Unconventional hydrocarbons in abiogenic Archean crystalline rocks: insight into ancient fluid chemistry in the Lupin Gold Deposit, Nunavut, Canada

By

Daniel Meagher

A thesis presented to the Department of Geology of

Saint Mary's University

in partial fulfillments of the requirements for the degree of

BACHELOR OF SCIENCE

IN GEOLOGY (HONOURS)

Examining committee:

Dr. Jacob Hanley, Department of Geology, Saint Mary's University

Department of Geology

Saint Mary's University

Halifax, Nova Scotia

April 13, 2016

Abstract: Unconventional hydrocarbons in abiogenic Archean crystalline rocks: insight into ancient fluid chemistry in the Lupin Gold Deposit, Nunavut, Canada

Daniel Meagher

Archean gold-bearing quartz veins at the Lupin mine occur in amphibolitic iron-formation in a deformed metaturbidite sequence. Stable isotope, fluid inclusion microthermometry, gas chromatography, laser ablation IC-PMS, and laser Raman microscopy techniques were used to study quartz-hosted fluid inclusions, the associated altered host rocks, and the relative timing and role fluids played in late stage gold precipitation.

Bulk GC crush analysis of vein quartz showed that fluid inclusion volatiles are dominated by CH_4, but also contain aliphatic species up to at least C6, and aromatic species that are suspected to be of a biogenic origin but could have been re-speciated by abiogenic processes (e.g., reductive coupling oligomerization). The vein quartz, at 20˚C, contains two petrographically distinct single-phase non-aqueous fluid inclusion types, classified as type-I and type-II. Type-II fluid inclusions ($T_{hCarbonic(avg)}$ = -22.4˚C) contain primarily CO_2-(CH_4-N_2-H_2S), and are early secondary in origin, forming as grain boundaries sealed up after most of the quartz had already grown. Type-I fluid inclusions ($T_{hCarbonic(ave)}$ = -89.9˚C) contain primarily CH_4-(N_2-H_2S), and are late secondary, crosscutting the healed grain boundaries that host type-II fluids. The type-I fluids were trapped heterogeneously with two-phase aqueous fluids between 320 - 490˚C and 1.2 – 2.2 kbar, as deduced by the method of intersecting isochores.

Sulfur found in vein and host sulfides has $\delta^{34}S_{VCDT}$ values of +1.8 to +3.4‰, which is in the endogenic (processes that originate within the earth) or magmatic source range. Nitrogen isotope analysis of fluid inclusions in vein quartz found a $\delta^{15}N_{AIR}$ value of +7.4‰, which indicates that organics and micas from the BIF and associated metasedimentary rocks are source possibilities. Carbon isotope analysis of fluid inclusions in vein quartz found $\delta^{13}C_{VPDB}$ values of -29.9 to -22‰, in accordance with a thermogenic origin of hydrocarbons, or originating from Fischer-Tropsch-type reactions.

Three possibilities for secondary gold precipitation are suggested based on ore assemblages and petrographic/compositional characteristics of fluid inclusion assemblages: (i) an increase in pH, which is suggested by the occurrence of magnetite with gold, decreasing the Au-complexing sulfur and Au concentrations in solution; (ii) minor changes in fO_2 in a highly oxidized system causing Au to drop out; or (iii) the partitioning of H_2S (and Au-complexing HS^-) from aqueous fluid to carbonic fluid as they mingled immiscibly, derived from different sources initially.

Date of submission: April 13, 2016

Acknowledgements

I would like to acknowledge the Society of Economic Geologists for research funding. I thank April Vuletich, Christabel Jean, and Dr. Kurt Kyser at Queen's Facility for Isotope Research for assistance in processing and presenting isotope data. A thank you goes out to Dr. Joe Petrus (Laurentian University) for analyzing, processing, and presenting laser ablation data that enhanced the manuscript. I would also like to extend my gratitude to my friends and colleagues, Kevin Neyedley and Mitch Kerr (Saint Mary's University), with whom I have had lengthy and comprehensive conversations regarding the scope and management of an Honours Thesis. Importantly, Kevin and Mitch collected and helped analyze data which was essential to the completion of this thesis. Thank you to Steve Crowell (Saint Mary's University) for providing supplemental data that strengthened this manuscript. I would also like to acknowledge Dr. Dan Kontak (Laurentian University) for constructive external reviews that improved the manuscript. My family (Pat, Doug, Chris and Stephanie) are thanked for their endless support that they have shown in every aspect of my life. Finally, I would like to thank my friend and supervisor, Dr. Jacob Hanley (Saint Mary's University), for his tireless support and mentorship that made this endeavour possible.

Table of contents

Acknowledgements iii

List of figures and appendices vi

List of tables vii

Chapter 1 - Introduction 1

1.1 - Introduction 1

1.2 – Banded Iron Formation (BIF) 2

1.3 – Orogenic gold deposits: their setting and fluid chemistry 4

1.4 – Fluids in metamorphic environments 6

Chapter 2 – Geological setting 9

2.1 – Lupin mining and exploration history 9

2.2 – Regional geology of the Contwoyto Lake area 9

2.3 – Gold mineralization in the Slave Province 15

2.4 – Local geology of the Lupin deposit 16

2.5 – Gold mineralization of the Lupin deposit 21

Chapter 3 - Methods 23

3.1 – C-N-S isotope systematics of vein-hosted fluid inclusions and associated sulfides in host rocks 23

3.2 – Laser Raman microscopy 24

3.3 – Fluid inclusion microthermometry 26

3.4 – In-line rock-crushing gas chromatography 27
3.5 – Trace and major element mapping of arsenopyrite by LA-ICP-MS 30
3.6 – SEM analysis 31
Chapter 4 – Results 31
4.1 – C-N-S isotope systematics of vein inclusion fluids and associated sulfides in host rocks 31
4.2 – Ore petrography and mineral compositions 44
4.3 – Fluid inclusion petrography and microthermometry 49
4.4 – Laser Raman microscopy 55
4.5 – In-line rock-crushing gas chromatography 63
4.6 – Arsenopyrite thermometry and trace element chemistry 66
Chapter 5 – Discussion and conclusion 73
5.1 – Discussion 73
5.1.1 – Evaluation of fluid sources 73
5.1.2 – Fluid compositions and associated P-T conditions 77
5.1.3 – Arsenopyrite – complexity in composition 83
5.1.4 – Implications for gold deposition and exploration 85
5.2 – Conclusion 88
References 91

List of figures and appendices

Figure 1.1: P-T diagram showing boundaries of immiscibility for various volatile mixtures in an aqueous fluid of mixed salinity. 8

Figure 2.1: Location map of Lupin 14

Figure 2.2: Graphic of idealized cross-section of gold orebody at Lupin. 19

Figure 3.1: Flame ionization detector schematic. 29

Figure 4.1 Nitrogen, sulfur, and carbon isotope compositions of various terrestrial reservoirs relevant for comparison to Lupin samples..... 36

Figure 4.2: Isotopic distribution fields related to CH_4 source 37

Figure 4.3: Polished slab of ore showing a cross-cutting quartz vein in sulfidic BIF 45

Figure 4.4: Sketch of an ore slab vein selvage showing seven typical gold textural occurrences 46

Figure 4.5: SEM-BSE images of gold texture associations surrounding quartz veins. 47

Figure 4.6: Mosaic of X-ray elemental intensity maps depicting a late pyrrhotite-electrum vein 48

Figure 4.7: Transmitted light photomicrographs of non-aqueous and aqueous fluid inclusions in auriferous quartz veins 51

Figure 4.8: Homogenization temperatures of a carbonic phase in quartz fluid inclusions. 54

Figure 4.9: Laser Raman microscopy spectra of type-I and type-II fluid inclusions on an intensity (counts) vs. Raman shift (cm-1) plot 57

Figure 4.10: Laser Raman microscopy spectra of type-III and type-III-I fluid inclusions on an intensity (counts) vs. Raman shift (cm-1) plot 58

Figure 4.11: Molar concentrations of volatile species in type-I and type-II fluid inclusions as determined by laser Raman microscopy 61
Figure 4.12: Two-dimensional composition maps, as determined with laser Raman microscopy, of a single type-I fluid inclusion showing the distribution of volatile species..... 62
Figure 4.13: Gas chromatogram of a vein quartz sample using a FID 64
Figure 4.14: Gas chromatogram of a vein quartz sample using a FID and a TCD in series 65
Figure 4.15: SEM-EDS analysis of arsenic in arsenopyrite shown on a T-X diagram with arsenopyrite-buffered curves. 68
Figure 4.16: Graphical correlation of Ag-Au vs. Te with LA-ICP-MS maps 69
Figure 4.17: Graphical correlation of Ag-Au vs. As with LA-ICP-MS maps 71
Figure 4.18: Graphical correlation of Sb-Au vs. Mo with LA-ICP-MS maps 72
Figure 5.1: The inferred P-T window for quartz-vein hosted type-I and type-III fluid inclusion in samples from the Lupin gold deposit using the method of intersecting isochores and the constraints determined from this study. 82
Appendix A: LA-ICP-MS Operating Conditions. 102
Appendix B: Quantified LA-ICP-MS maps. 103

List of tables

Table 1: Characteristics of banded iron formation-hosted gold deposits 20
Table 2: C isotope data for bulk fluids contained in Lupin quartz veins 38
Table 3: C isotope data for fluids contained in Lupin quartz veins compared to isotope data of various metamorphic and igneous settings 39

Table 4: N isotope data for fluids contained in Lupin quartz veins 40

Table 5: N isotope data for fluids contained in Lupin quartz veins compared to isotope data of various metamorphic, igneous, and sedimentary settings 41

Table 6: S isotope data for sulfides in quartz veins and wall-rocks at Lupin 42

Table 7: S isotope data for sulfides in Lupin quartz vein selvages and wall rocks compared to isotope data of various Archean sediment-hosted or associated deposits 43

Table 8: Microthermometric data for type-I and –II fluid inclusions 52

Table 9: Laser Raman microscopy data for non-aqueous quartz-hosted fluid inclusions 59

Chapter 1 - Introduction

1.1 - Introduction

There are many uncertainties concerning the hydrothermal evolution of Archean gold deposits due to the wide range of pressure-temperature (P-T) conditions of mineralization that are associated with these deposits, in addition to their occurrence in many rock types in, and adjacent to, Archean greenstone belts but can be genetically related through common hydrothermal processes. For example, the Archean Yilgarn Block in Western Australia has individual deposits with P-T conditions of formation ranging from 200 to 700˚C and 1 to 5 kbar, corresponding to formation depths of 3 to 18 km (Ridley et al., 1995). Yet, these deposits share hydrothermal fluids of similar compositions (i.e., major cation components, major salts, and isotope ratios). Characterization of the chemistry of hydrothermal fluids of Archean gold systems is a subject of ongoing interest and an essential focus to discern a deposit's relation to other nearby deposits showing variable metamorphic grade and whether they share the same hydrothermal fluid origin for the mineralization.

Geusebroek and Duke (2005) postulated an endogenic (processes that originate within the earth) metamorphic metallogenic model for the Lupin BIF-hosted lode gold deposit in Nunavut. Furthermore, these authors preferred an epigenetic, or endogenic, model over both the syngenetic gold-enriched BIF and the exogenetic granite-sourced gold models. However, little is known about the fluid chemistry and the associated hydrothermal-metamorphic processes that locally reconcentrated gold in and adjacent to the quartz veining at Lupin. The goals of this thesis project are to: (i) characterize the volatile chemistry and P-T conditions of entrapment of nitrogen- and hydrocarbon-rich

fluid inclusions occurring in mineralized quartz veins, and the relationship of these fluid types to gold mineralization, and (ii) compare the fluid chemistry and hydrothermal processes related to the mineralization to those of modern petroleum/natural gas systems as well as other Archean gold deposits. In doing so, this study will discern whether specific trace gas hydrocarbon signatures are diagnostic of abiogenic versus biogenic origin. In addition, these hydrocarbon signatures may prove to be useful as exploration criteria to locate Archean gold systems under buried cover.

In this study, samples of quartz veins and vein selvage material from the Lupin deposit were used to fully evaluate the volatile stable isotope and mineralogy/mineral chemistry of gold-bearing quartz veins.

1.2 – Banded Iron Formation (BIF)

The time span of deposition of BIF on Earth ranges from ~3.8 Ga (Early Eoarchean Era) to ~1.8 Ga (Late Paleoproterozoic Era) with most forming at ~2.4 Ga (Beukes, 1973; Klein and Beukes, 1993; Huston and Logan, 2004). The increase in oxygen abundance in the atmosphere between ~2.5 and ~1.9 Ga can be correlated with the deposition of most Superior-type BIF (Goldfarb et al., 2001). However, this major change in oxidation state had no direct influence on the genesis of gold ore because substantial gold deposits formed prior to 2.5 Ga and subsequent to 2.1 Ga. The Superior-type BIF formed in stable platform environments and show no association with gold ores. Conversely, Late Archean and Paleoproterozoic Algoma-type BIF deposits show a distinct spatial association with orogenic gold ores and are closely associated with oceanic volcanic activity.

Hydrothermal activity where such fluids transected BIF created alteration zones that record extreme sulfidation, as evidenced from abundant pyrite, pyrrhotite, and arsenopyrite (Groves et al., 1998). These deposits also show a clear lateral zonation of alteration phases with assemblages that are several meters thick.

BIF can provide favorable chemical traps for gold mineralization because during the regional deformation of continental margins these iron-rich rocks provide welcoming reaction zones for replacement style mineralization formed during ingress of metamorphic fluids (Goldfarb et al., 2001). These hydrothermal fluids, which are inferred to have contained gold and sulfur, entered and reacted with specific chemical/sedimentary horizons containing iron oxides (magnetite and/or hematite) causing the precipitation of gold and sulfides (Wilton, 1996). Major gold deposits can be hosted within these BIF horizons, such as the Lupin mine in the center of the Slave province, Nunavut, Canada. Other examples of major BIF-hosted gold deposits include: the Cuiabá gold deposit, the Meadowbank gold deposit, and the Musselwhite gold deposit. The Cuiabá gold deposit in Brazil contains fine-grained gold (<60 μm) associated with the sulfide-rich portions of BIF host; gold grades decrease in sulfide-poor segments (Ribeiro-Rodrigues et al., 2007). The Meadowbank gold deposit in Nunavut is also associated within sulfide-rich portions of BIF, with the bulk of gold being texturally associated with pyrrhotite (Janvier et al., 2014). Finally, the Musselwhite gold deposit in Ontario, in which gold was extensively remobilized, is hosted in highly reactive silicate BIF facies (Dubé et al, 2015).

1.3 – Orogenic gold deposits: their setting and fluid chemistry

Within the Archean Eon, orogenic gold ores are largely confined to host rock packages in the Neoarchean Era (Goldfarb et al., 2001). The only significant gold deposits in rocks from the Paleo- and Meso-Archean are in the Barberton greenstone belt, South Africa (3.57 – 3.08 Ga), which has a resource estimate of 10 million ounces (Goldfarb et al., 2001). Much of the older Archean crust may have been recycled into the mantle during increased convection rates on early Earth with much higher temperatures (Condie, 1997). It follows, therefore, that the nearly exclusive nature of greenstone-hosted gold ore in Late Archean rocks, and, to a lesser extent, in Paleoproterozoic rocks is partly due to a decrease in mantle convection rates and the resulting preservation of this mineralized crust in continental platforms. Gold mineralization associated with late stage veins can be as young as 0.5 Ga, like the Crixas greenstone belt-hosted veins which formed during the final stages of Brasiliano deformation (Goldfarb et al., 2001). Slate belts can also host Au, with some forming very late; for example, deposits in the late Devonian to Early Carboniferous Carolina slate belt of the southeastern United States, and Meguma terrane of Nova Scotia (Bierlein & Crowe, 2000).

Examination of the world's preserved greenstone belts show a dominant association of gold ore and greenschist facies rocks (Groves et al., 1998). This association is linked to metamorphic fluid production at depth and its focusing into structurally ideal ground at shallower depths. These fluids, which have been generated at the amphibolite-greenschist transition, unmix during their ascent and subsequent cooling. This unmixing can lead to a decrease in Au solubility (see below; Goldfarb et al., 2005). Higher and lower metamorphic grade terranes in the Archean also host some of the world's

significant orogenic gold deposits. For example, the Archean terrane of the Slave Province of northern Canada contains ore hosted by clastic marine sedimentary rock with greywacke metamorphosed to psammite, quartzite, and mica-rich schist, and argillite metamorphosed to slate, phyllite, and pelitic schist, all within the range of greenschist to amphibolite grade.

There are specific styles of structure, alteration, and metal budget associated with Archean lode gold deposits (Smith, 1996). These deposits are comprised of shear zones hosting veins or breccias abutted by wall-rock alteration with elemental enrichments in K, S, CO_2, H_2O, SiO_2 ± Na and large ion lithophile elements (LILE) (Smith, 1996; Groves et al., 1998). There is normally more Au relative to Ag and base metals in these deposits, with highly variable Ag, As, S, W, Sb, Bi, Te, B, and base metal enrichment.

Trace and major elements associated with quartz veining in Archean orogenic gold deposits are carried into the system and deposited by neutral to moderately acidic, low salinity (≤ 5 wt. % NaCl equiv.) H_2O-CO_2±CH_4 fluids (Smith, 1996; Groves et al., 2003). Kerrich and Wyman (1990) postulated that these ore-forming fluids were generated from deep crustal, convergent plate margin tectonics taking place after magmatism and metamorphism in ore-hosting supracrustal rocks. Fluid transport of gold occurs via reduced bi-hydrosulfide complexes (i.e., $Au(HS)^{\circ}$, $HAu(HS)^{\circ}_2$, and $Au(HS)^{-}_2$: Seward, 1973; Shenberger and Barnes, 1989; Hayashi and Ohmoto, 1991). The transported gold may be dropped out of solution by fluid mixing, which leads to neutralization and dilution of the gold-bearing fluid leading to the destabilization of gold-bearing complexes, or the interaction of fluid and wall-rock which leads to neutralization and desulfurization, similarly destabilizing the gold bi-hydrosulfide complexes. The gold-

bearing fluids may also undergo immiscibility, which is another major mechanism for gold deposition. Immiscibility involves the effervescence (phase separation) of carbonic (either CO_2-rich or CH_4-rich) fluid from an initial aqueous-carbonic fluid of low salinity. The preferential partitioning of hydrogen sulfide (H_2S), a volatile species, into the carbonic phase lowers the amount of H_2S (and HS^-) in the aqueous fluid and causes gold bi-hydrosulfide complexes to destabilize (Naden and Shepherd, 1989). See Section 1.4 for more discussion on immiscibility in metamorphic fluid systems.

1.4 – Fluids in metamorphic environments

Archean orogenic gold deposits hosted in rocks of various metamorphic grades – from sub-greenschist to lower granulite facies – commonly formed from and contain preserved (in inclusions) low-salinity, mixed aqueous-carbonic fluids (Mikucki and Ridley, 1993). The deposits that are sub-amphibolite facies, like the Lupin deposit, are associated with ore fluids with relatively high concentrations of CO_2. Thermodynamic and fluid inclusion measurements demonstrate that sub-amphibolite facies generally have fluids with X_{CO2} ranging from 0.05 to 0.25 (Mikucki and Ridley, 1993).

Determining the P-T range of immiscibility of metamorphic fluids is important in gold exploration because immiscibility induces vapor-aqueous liquid partitioning of H_2S, as noted already (Seward, 1973; Heinrich et al., 2004; Pokrovski et al., 2008; Mernagh and Bastrakov, 2013). Partitioning of important volatile species (i.e., H_2S) controls the concentration of dissolved gold complexes in solution [i.e., bisulfide (HS^-), sulfite (O_3S), thiosulfate ($S_2O_3^{2-}$) and polysulfide (S_n^{2-})] under hydrothermal conditions relevant in orogenic gold systems. In addition, the P-T range of immiscibility can expand or shrink depending on the volatile chemistry and salinity of metamorphic fluids (Fig. 1.1).

In addition to CO_2 and CH_4, it has been well documented through microthermometry and laser Raman analysis that N_2 is also an important non-aqueous volatile component in fluid inclusions in metamorphic terranes (Bottrell et al., 1988). Fluid inclusions containing N_2 can be found in barren and auriferous quartz veins in orogenic gold deposits and associated metamorphic rock assemblages in a diversity of settings of different ages (Table 5).

Nitrogen found in quartz veins of orogenic gold deposits has three possible origins. First, N_2 can originate from sedimentary protoliths rich in decomposed/devolatilized organic matter (Bottrell et al., 1988). Second, N_2 can originate from decomposed NH_4^+-bearing silicate minerals (amphiboles, micas, clays) in sedimentary or magmatic crustal- or mantle-derived protoliths, or from pre-existing metamorphic micas that decompose in later prograde paths (Dee & Roberts, 1993). Third, N_2 can originate from the mantle as a primary volatile phase (Elvevold & Andersen, 1993).

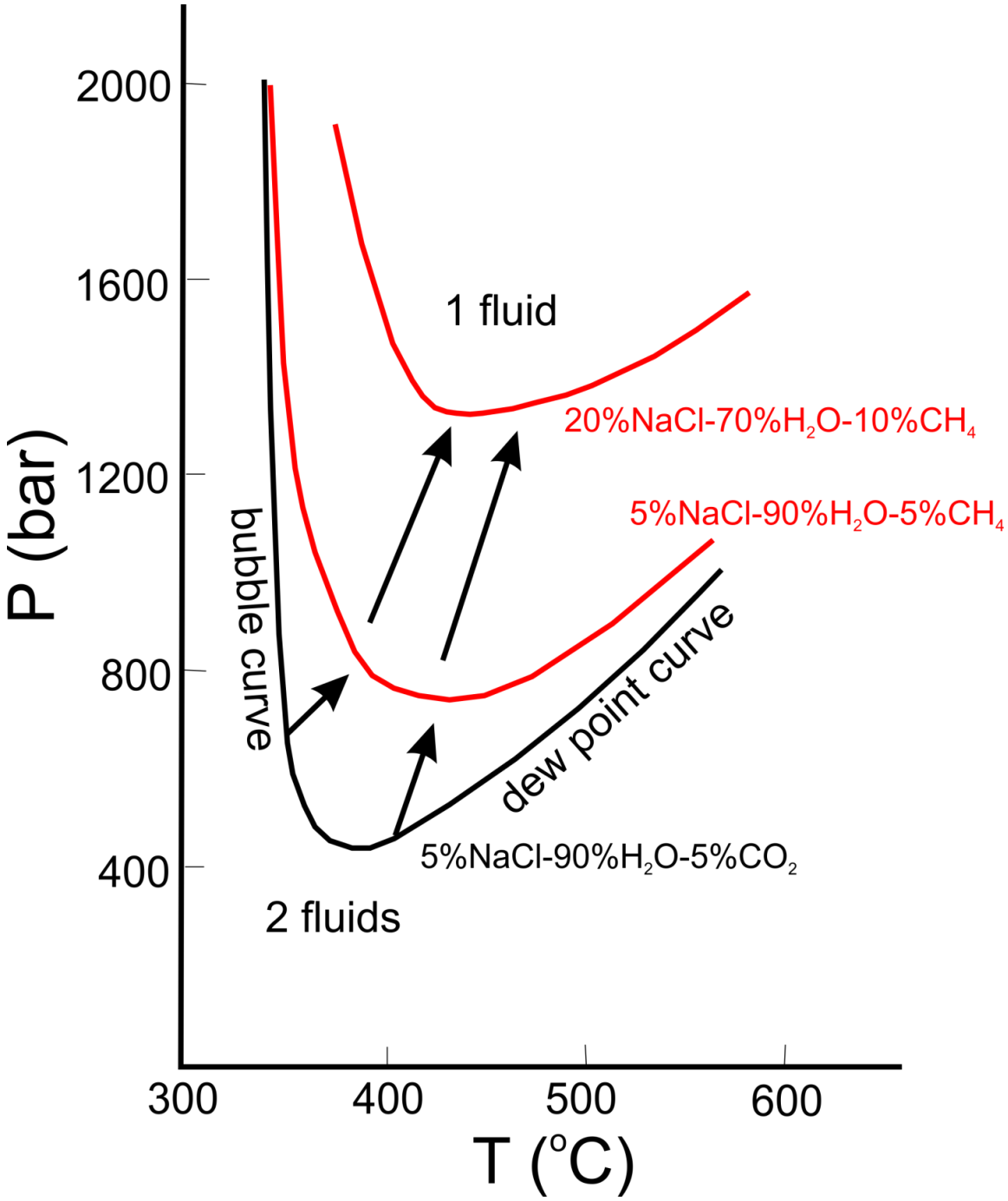

Figure 1.1: P-T diagram showing boundaries of immiscibility for various volatile mixtures in an aqueous fluid of mixed salinity. The boundaries (i.e., solvi) separate 2-fluid from 1-fluid fields in the systems NaCl-H_2O-CO_2 and NaCl-H_2O-CH_4 (Schmidt and Bodnar, 2000; Duan et al. 2003). The P-T range of immiscibility is much greater for systems containing CH_4 (or N_2) and with higher salinity.

Chapter 2 – Geological setting

2.1 – Lupin mining and exploration history

The Lupin mine has produced over 3.4 million ounces of gold, with an average ore grade of 8.9 grams per tonne (Gwinnett, 2015). Mining of the late Archean gold-bearing BIF began in 1982 and ended in December, 2004. The gold is extracted by both open-pit mining and underground operations from four zones – West, Central, East and McPherson – with the center and west zones of the deposit open at depth (Bullis et al, 1994; Tarikh, 2015). The mine was placed on care and maintenance in February, 2005 (Gwinnett, 2015).

Elgin Mining Inc., a Canadian based company, acquired the Lupin mine on July 8, 2011 and planned to commence production in 2015 (Engineering & Mining Journal, 2012). However, they were taken over in September, 2014, by Mandalay Resources as finalized by a court-approved plan of arrangement (CNW Group Ltd., 2014). Mandalay subsequently sold the Lupin mine to WPC Resources for $3-million (CAD), 18 million shares, and a $1.6-million convertible note for the environmental bond (Gwinnett, 2015).

2.2 – Regional geology of the Contwoyto Lake area

The Lupin gold deposit is hosted in the Archean Yellowknife Supergroup, which is comprised of supracrustal metasedimentary and metavolcanic rocks. The gold deposit is found in the Contwoyto Lake area in the western Kitikmeot District of Nunavut, about 400 km north-northwest of Yellowknife and 80 km south of the Arctic Circle (Fig. 2.1) (Kerswill, 1986, 1992, 1993, 1996; Bullis et al., 1994; Geusebroek & Duke, 2005;).

The Yellowknife Supergroup is part of the Slave Province and is comprised of four formations in the Contwoyto Lake area: the Contwoyto, the Point Lake, the

Keskarrah, and the Itchen (Bullis et al., 1994). There are no significant internal unconformities within the Yellowknife Supergroup which indicates that these formations were deposited in the same period of time (Henderson & Easton, 1997). The Neoarchean Contwoyto Formation contains the Lupin deposit and consists of interbedded graywacke and mudstone that represent turbiditic sediments forming a submarine fan, with lenses and horizons of BIF, and minor volcanic components.

Regional structural studies of the Contwoyto Lake and Nose Lake area indicate that there have been four major events of deformation, denoted as D1, D2, D_{NE} and D_{NW} (Relf, 1990). D1 occurred before peak metamorphism and formed structures distinguished by tight to isoclinal folds of bedding (F1). Cleavage (S1) of biotite and muscovite is sometimes observed in the hinge of F1 folds and is axial planar, which means the S1 fabric may be related to F1 folding. D2 is dated at about 2608 Ma and is represented by syn-thermal peak tight to isoclinal folding, faulting and cleavage development. Based on garnet-biotite geothermobarometric studies, peak metamorphic conditions are thought to have been approximately 570˚C and 4 kbar, which places these rocks in the upper greenschist to amphibolite facies (Ford & Duke, 1993; McCuaig et al., 1993). The folding of bedding (F2) during D2 serves as the most dominant mesoscopic folding event in the Contwoyto Lake and Nose Lake area (Fig. 2.1). The main planar fabric of the metasediments in the area mapped by Relf (1990) is biotite and muscovite cleavage (S2) which is associated with D2 because of its distinct axial planar orientation on the hinges of F2 folds. The interaction of the D1 and D2 deformational events formed a modified domal structure which encompasses the gold deposit (Bullis et al., 1994). The

gold deposit occupies the limbs of the domical structure and is hosted within a sulfidic BIF with areas of variable sulfide enrichment.

The deformational events D_{NE} and D_{NW} (formerly referred to as D3 and D4, respectively, in the literature) occurred contemporaneously around 2593 Ma after peak metamorphism and are characterized by two sets of open, upright NE- and NW-striking cross folds (King et al., 1988, 1989; Relf, 1989, 1990). Above, the NE- and NW- subscripts represent the direction of strike for the cleavage and axial planes to folds of the two structure sets; the NE and NW orientations of these structures are very persistent which makes them easy to identify. Northeast- and NW-structures are interpreted to be of the same generation (i.e., post-thermal peak) due to similar relationships to thermal peak minerals. Both NE- and NW-folds (F_{NE} and F_{NW}, respectively) have generated superimposed foliations in the form of an S2 crenulation cleavage and associated porphyroblasts in response to two different stress directions. Locally, F_{NE} folds have a well-developed crenulation cleavage represented in biotite, whereas, F_{NW} folds have a local cleavage defined by biotite. Regionally, these cross folds have played an important part in defining the kilometer-scale domical structure (Fig. 2.1). Gold is hosted in the limbs of the dome; therefore, detailed structural mapping of these cross folds is important when determining the plunges of the folds, their subsurface geometries, and related gold occurrences. As well, late gold redistribution in quartz veins may be a result of the D_{NE} and D_{NW} events related to unroofing post-peak metamorphism.

During latest D2 and earliest $D_{NW/NE}$, pyrrhotite replaced grunerite-hornblende-biotite, rocks were silicified with associated calc-silicate replacement (skarnification), and shear-related hydrothermal biotitization/chloritization occurred (Geusebroek and

Duke, 2004). In addition, there was post-kinematic growth of andalusite, almandine, and arsenopyrite-loellingite around late quartz veins. Finally, hydrothermal activity produced a spatially restricted alteration of andalusite to paragonite, and altered almandine garnet to chlorite.

The Yellowknife Supergroup of supracrustal rocks have been intruded by Neoarchean granitoid complexes, as represented by six plutonic units of variable age in the Contwoyto Lake area, identified as C1-C6 (King et al., 1990). The oldest units, C1 to C3, are comprised of gabbroic to granodioritic rocks and are contemporaneous with volcanic activity roughly 2650 Ma (Bullis et al., 1994; King et al., 1990). Emplacement of these units was before D2 (i.e., 2608 Ma), thus predating the metamorphic thermal peak. Subsequently, C4 and C5 were emplaced during peak metamorphism and these suites have a wide range of composition from gabbroic to granitic. Finally, the C6 plutonic unit was emplaced post-peak metamorphism at around 2593 Ma and contains granitic to syenogranitic and locally pegmatitic rocks. All Archean rocks have been cut by Proterozoic diabase dyke swarms (Bullis et al., 1994).

The rocks of the Contwoyto Formation have undergone regional and contact metamorphism (Bullis et al., 1994). Cordierite and sillimanite isograds mapped by Relf (1989) divide the Contwoyto Formation into three metamorphic zones: the biotite zone, the cordierite zone, and the sillimanite zone (Fig. 2.1). The gold deposit lies within the biotite zone of upper greenschist facies which extends from the surface to roughly 550 meters depth where it intersects with the cordierite isograd (Bullis et al., 1994). There is alteration of biotite and hornblende to chlorite which indicates that an early prograde metamorphism is followed by retrograde metamorphism. The cordierite zone represents

peak metamorphism and its isograd cross-cuts major folds indicating that this event postdates the main folding (Relf, 1989). The appearance of mineral assemblages in the cordierite zone that contain andalusite and/or staurolite is indicative of a low pressure-high temperature regime (Bullis et al., 1994). Although metamorphic assemblages change in the pelitic rocks when transitioning from the biotite to cordierite zones, they appear unchanged in the ore-bearing BIF.

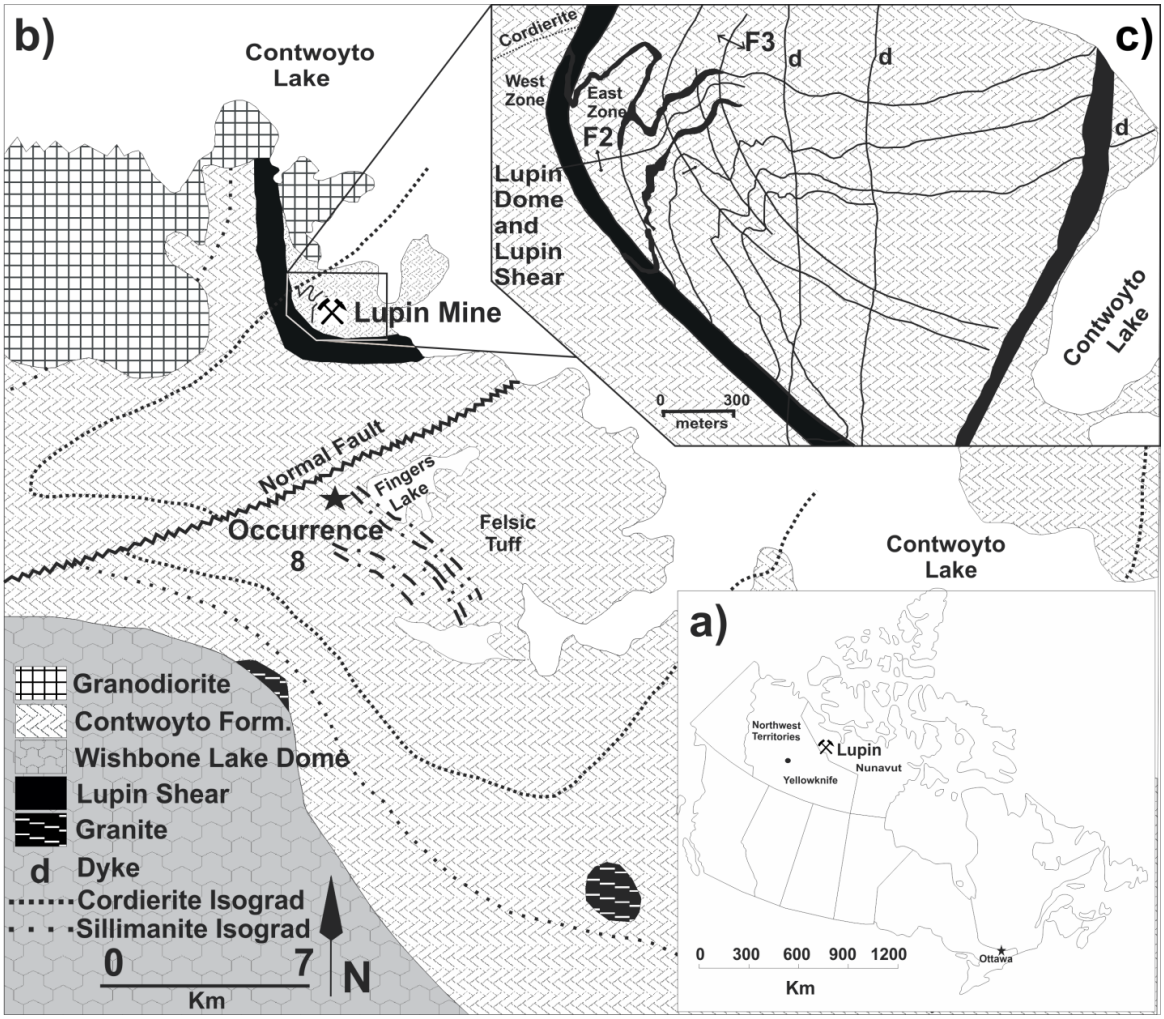

Figure 2.1: Location map of Lupin. (a) Location map of the Lupin deposit (lat 65˚ 48´N, long 111˚ 15´W) in the western Kitikmeot District of Nunavut, near the border with NWT (Bullis et al., 1994). (b) Regional geological map of the deposit showing major structural elements and isograds, lithologies, and water bodies. (c) Local geological map of the BIF and dome, showing the F2 and F3 fold structures (West-East zones projected to surface from the ~890 m level). (Image modified by Steve Crowell after Geusebroek and Duke, 2005).

2.3 – Gold mineralization in the Slave Province

The Slave craton is a world class gold province that formed between 2.8 and 2.55 Ga and is historically a large part of the global gold resource (Goldfarb et al., 2001). The spatially extensive metasedimentary and metavolcanic terranes of the Late Archean Slave Province contain broadly distributed gold-bearing BIF (Ford, & Duke, 1993). A prolonged history of deformation, metamorphism, and plutonism has impacted the structure and mineralogy of the thick turbidite sequences that encompass the gold-bearing BIF. The economically viable gold mineralization is found at structurally complex sites within the BIF characterized by polyphase folding. At Lupin, BIF units are enclosed by metapelites with stable prograde metamorphic assemblages.

Ford and Duke (1993) investigated five different gold occurrences in the Archean Slave Province, including the Lupin gold deposit, and found two distinct prograde mineral assemblages representing two facies of protolith silicate BIF spatially hosting or associated with the deposits. The two facies are amphibolitic iron formation (AIF) and pelitic iron formation (PIF). The AIF mineral assemblage is the one that hosts the Lupin gold deposit and consists of quartz + grunerite + hornblende + pyrrhotite + garnet + graphite + ilmenite. Textural analysis shows that grunerite crystallized prior to hornblende. In addition, garnet and other prograde metamorphic minerals in AIF are in textural equilibrium with banded pyrrhotite, meaning sulfidation of AIF happened during the approach to peak metamorphism. The prograde mineral assemblages in AIF were replaced on the margins of quartz veins by retrograde hornblende, grunerite, arsenopyrite-loellingite, chlorite, garnet, zoisite, apatite, carbonate, ferroactinolite, and gold-bearing sulfide minerals. Metamorphism in the Slave Province started around 2690

Ma (Groves et al., 1998). The tectonic event associated with the metamorphic rocks of the Slave Province is the 100-m.y.-long subduction regime initiated by 2712 Ma.

2.4 – Local geology of the Lupin deposit

The Lupin deposit is in the Contwoyto Formation, north-central Slave Province and is part of an Archean metaturbidite sequence (Bullis et al., 1994). The age of the Lupin deposit is constrained by uranium-lead dating in detrital zircon grains of the north-central Slave Province, which showed concordant to slightly discordant ages ranging from 3006 to 2661 Ma (Mortensen et al., 1992). The ore bearing sections of the deposit are restricted to an uninterrupted greenschist-amphibolitic transition grade BIF. The main ore bearing section is a sulfide-rich amphibolitic BIF with small-scale interbeds of remnant phyllite and quartzitic metagraywacke (Fig. 2.2). The footwall of the primary orebody is mainly in contact with massive quartzitic metagraywacke that contain pelitic beds and lenses. Phyllites that grade into metagraywacke are commonly found in the hanging wall of the orebody. Garnet-amphibole-chlorite-biotite schists that can be up to a few meters wide are found at the zone of contact between the orebody and the phyllites. The amount of garnet decreases with increased distance from the orebody. Discontinuous sulfide-rich and sulfide-poor amphibolite horizons can be found in the pelitic zones that lie above and below the amphibolitic BIF. These amphibolite horizons can be up to 2 meters wide and stretch laterally for tens of meters. Generalized characteristic features of Lupin-like deposits are listed in Table 1.

The mineralized quartz vein selvages in the orebody postdate S3 cleavage which is associated with the contemporaneous D_{NE} and D_{NW} events (Geusebroek & Duke, 2004). These two deformation events account for the Lupin shear strands. The inner shear

strands and the outer Sand Bay make up the perimeter of the Lupin deformation zone (LDZ). The S3 shear strands in the LDZ contain the most intense chloritization within vein selvages. The mineralized BIF is bound by the chlorite shears that contain variable amounts of porphyroblastic almandine. In addition, euhedral arsenopyrite grains which distinctly postdate S3 shear fabric are within the chlorite selvages that developed around late quartz veins. The chlorite-arsenopyrite selvages in the shallow parts of the deposit are gold poor (10 g/t) but deeper in the deposit there is a gold enrichment (20 g/t) hosted in the same selvages. Shallower ore has gold reporting mostly to ubiquitous pyrrhotite, whereas in deeper ore there is a much more restricted association with pyrrhotite. Importantly, free gold in the vein selvages resides mostly along the contacts of remnant loellingite cores in late arsenopyrite grains. This association of gold with loellingite cores indicates that gold was initially dissolved in loellingite at temperatures above the stability limit of arsenopyrite and unmixed during the reaction of loellingite to arsenopyrite. The remnant loellingite has an average gold content of ~40 ppm, whereas arsenopyrite and pyrrhotite together have less than ~1 ppm (Chryssoulis & Agha, 1996). So, the refractory ore constituent is accounted for by mainly remnant loellingite.

The mineralized BIF hosts cross-cutting ("ladder", crack-seal type and tension gash infillings) and foliation-parallel (often boudinaged) quartz veins. The BIF adjacent to quartz veins contains a zoned sequence of alteration minerals and secondary sulfides (Lhotka, & Nesbitt, 1989). Closest to the veins there is a calc-silicate composition with a mineral assemblage of hedenbergite, quartz, epidote, scheelite, and grossular garnet. This mineralogy is followed by an arsenic-rich zone that contains hornblende, quartz, hedenbergite, epidote, and actinolite. Even farther away from the veins are gold-rich

zones (~530 ppm Au) with iron sulfides like pyrite and pyrrhotite, and minerals similar to the arsenic-rich zone (i.e., hornblende, quartz, hedenbergite, epidote, and actinolite). The quartz veins show locally high gold grades and are characterized by alteration assemblages containing electrum-pyrite-arsenopyrite-loellingite-pyrrhotite-grunerite-chlorite (Fig. 4.3).

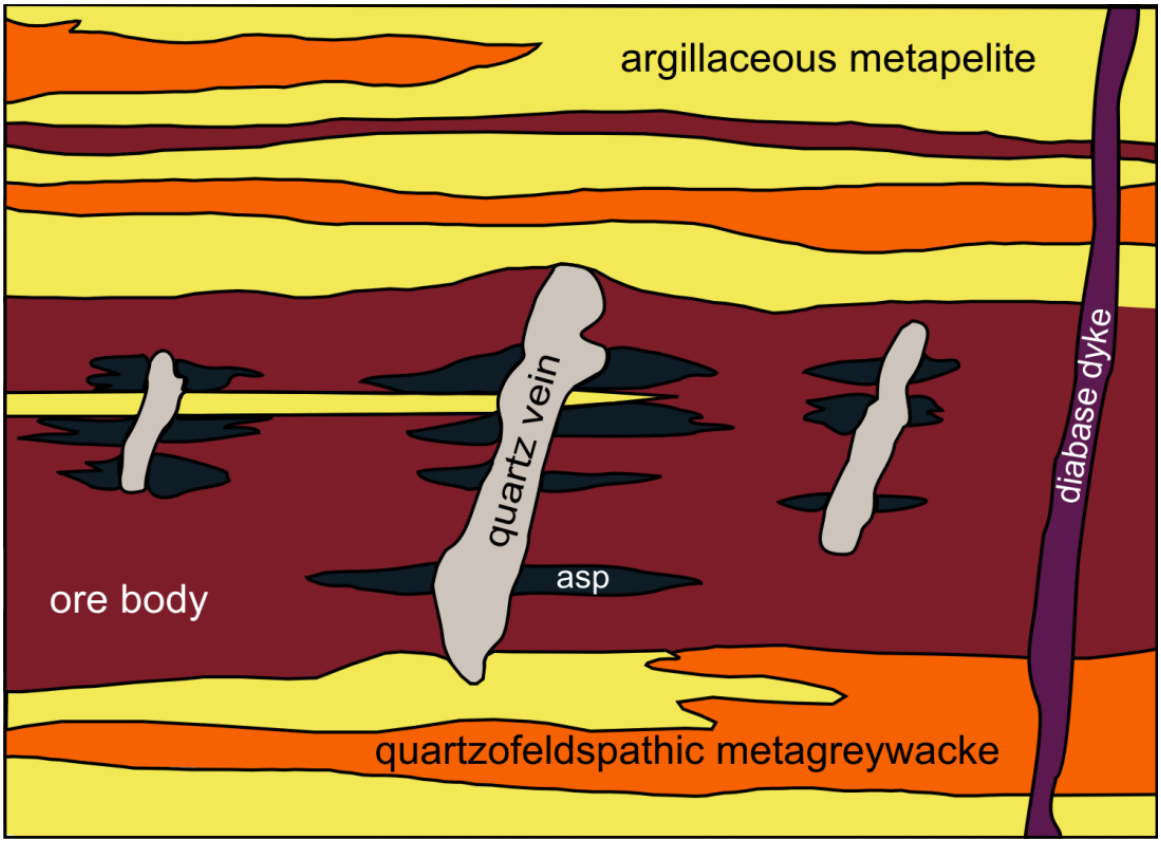

Figure 2.2: Graphic of idealized cross-section of gold orebody at Lupin. Arsenopyrite halos represent sulfide zoning around quartz veins and are more common than pyrrhotite halos. The orebody is bound by dominantly quartzofeldspathic metagraywacke in its footwall and dominantly argillaceous metapelite in its hanging wall. Near mineralization, the BIF has been modified from quartz-grunerite-magnetite to hornblende-quartz-pyrrhotite-pyrite (to ~30 vol%) with chlorite and arsenopyrite locally. The ore is not stratigraphically distinct but represents the most sulfidic domains of the main BIF. Discontinuous BIF units occur above/below the main ore BIF. Image modified from Bullis et al. (1994).

Table 1: Characteristics of banded iron formation-hosted gold deposits

1. Deposits are stratiform
2. Gold mostly restricted to iron-formation or to veins that crosscut sulfide-iron-formation
3. Sulfide-iron-formation occurs in several thin, but laterally continuous units that are conformably interlayered with barren silicate-iron-formation and/or carbonate-iron-formation and clastic sedimentary rocks
4. Sulfide-iron-formation is well laminated and chert-rich; iron sulfide minerals are typically finely layered
5. Distribution of iron sulfide minerals and gold are not clearly controlled by veins and/or late structures
6. Orebodies are as deformed or more deformed than associated rocks
7. Iron sulfide minerals show effects of deformation and metamorphism
8. Deposits occur in both greenschist and amphibolite facies terranes
9. Sulfidation textures are absent
10. Lack of orebody-scale alteration; localized vein-related alteration does occur
11. Vein-related alteration is commonly atypical of "mesothermal vein" gold deposits
12. Oxide-iron-formation is lacking in the deposits, irrespective of metamorphic grade
13. Pyrrhotite is typically the dominant iron sulfide mineral; in some cases early pyrrhotite has been replaced by pyrite
14. Arsenic is generally abundant adjacent to late quartz veins, but is not well correlated with gold
15. Silver contents of gold grains are moderately high (Au-to-Ag ratios - 3.0-7.0)
16. Deposits are rare, can be very large, and are less difficult to evaluate and mine than are the non-stratiform deposits

Table modified from Kerswill, 1996.

2.5 – Gold mineralization of the Lupin deposit

The BIF-hosted orogenic gold deposit at Lupin demonstrates multiple stages of gold enrichment. The first stage of gold enrichment is associated with the development of auriferous sulfidic BIF. This stage of gold enrichment is more pronounced in shallower parts of the orebody where grades are higher in sulfides than in deeper parts of the orebody. The second stage of gold enrichment is potentially associated with quartz veining that cross cuts primary BIF layering. Mineralization is characterized by fine grains of gold which have precipitated in association with pyrrhotite and arsenopyrite in amphibolitic BIF (Bullis et al., 1994). Gold associated with quartz veins is locally of higher grade deeper in the orebody and very poor gold grades in shallower parts of the orebody.

Quartz veining and the replacement of grunerite by hornblende are conclusive characteristics of the gold-bearing portions of the BIF (Bullis et al., 1994). The portions of the host BIF that have low concentrations of gold commonly show sulfide zoning around quartz veins, with arsenopyrite halos being more limited to the quartz veins than pyrrhotite halos. The sections of the host BIF that have high concentrations of gold have a density of one quartz vein per meter along strike. The distribution and increased abundance of pyrrhotite in portions with higher concentrations of gold creates a texture of sulfide banding. However, Kerswill et al. (1996) show that these quartz veins are a minor part of the gold ore and that field data is more consistent with a genetic model that applies to synsedimentary concentration of considerable quantities of the gold and sulfur in the stratiform portion of the deposit. The authors argue that only a small portion of the

gold and sulfur were brought in during quartz vein formation, and that epigenetic processes contributed very little to gold mineralization in the deposit.

The deposit origin is controversial with both epigenetic or syngenetic models suggested (Goldfarb et al., 2001). Kerswill (1996), arguing for a syngenetic model, stated that hydrothermal fluids deposited all the constituents (Fe, Si, Ca, S, As, Au, Ag, Cu, C, CO_2, W, etc.) during chemical sedimentation or early diagenesis. The idea that hydrothermal fluids deposited all the constituents during chemical sedimentation or early diagenesis is based on a submarine hydrothermal vent model (Haynes, 1987). The typically vein-controlled distribution of certain constituents (Si, Ca, As, W, etc.) is accounted for by the localized remobilization of these constituents during metamorphism and/or deformation in an essentially closed system. Kerswill (1996) argued that the observed low gold grades near quartz veins (and proportion of gold associated with veins) are evidence that the remobilization of gold by epigenetic processes was very minor. In contrast, Nesbitt and Lhotka (1989) deduced that the deposit is of epigenetic origin in which all the Au, S, and As were introduced by late quartz veins. Essentially, an epigenetic model states that certain constituents of the iron-formation were deposited during chemical sedimentation (Fe, Ca, some Si and CO_2, etc.) whereas others are associated with ore formation (S, Au, Ag, Cu, As, W, some Si and CO_2, etc.) and were introduced during vein-related hydrothermal activity that occurred due to much later deformation, metamorphism, and/or magmatism.

Goldfarb et al. (2001) acknowledged that many researchers have attempted to relate Algoma-type BIF-hosted gold ores to syngenetic processes associated with BIF deposition; however, Goldfarb et al. (2001) have advocated for an epigenetic origin.

These authors explained that significant volumes of BIF were located along deforming cratonic margins during the Late Archean and Early Paleoproterozoic global episodes of orogenesis, which formed suitable chemical traps for orogenic gold mineralization within complex volcano-sedimentary terranes. Replacement style mineralization was supported by the presence of iron-rich rocks in the deforming continental margins.

Chapter 3 - Methods

3.1 – C-N-S isotope systematics of vein-hosted fluid inclusions and associated sulfides in host rocks

Isotope analysis of N_2 ($\delta^{15}N_{AIR}$) and carbon ($\delta^{13}C_{VPDB}$) released from fluid inclusions in vein quartz samples was carried out at the Queens Facility for Isotope Research (QFIR) at Queens University, Kingston, Ontario. Two samples of quartz measuring 3.5 and 4.5 g, respectively, were analyzed using a Costech ECS 4010 (for thermal decrepitation of inclusions) coupled to a Thermo-Finnigan Delta^{Plus} XP Continuous-Flow Isotope Ratio Mass Spectrometer (CF-IRMS).

Values of bulk $\delta^{13}C$ and $\delta^{15}N$ are reported using the delta (δ) notation in units of per mil (‰) relative to Vienna Pee Dee Belemnite (VPDB) and AIR ($\delta^{15}N$=0‰), respectively, with a precision of ± 0.2‰ for both isotope measurements. The $\delta^{13}C_{VPDB}$ values are bulk analyses of a mixture of C-bearing volatiles (CH_4, CO_2, etc.). Gas chromatography bulk analysis was performed (see Section 3.4) in order to discern the relative proportions of each volatile species, allowing simplification of the interpretation of $\delta^{13}C_{VPDB}$ values. Contributions of N from impurities in the quartz (e.g., mica grains) were minimized through the selection of clean quartz samples via careful hand-picking

from crushed samples with the aid of a binocular microscope. Analytical protocols at the QFIR lab ensured that 10% of sample analyses represented certified reference materials and secondary standards, random duplication of unknown samples, and blanks.

Large arsenopyrite crystals in vein alteration halos and matrix/vein sulfides (pyrrhotite and pyrite) were sampled with a ~2 mm diamond drill bit to produce sulfide powders that were analyzed for bulk $\delta^{34}S_{VCDT}$ at the QFIR. Three arsenopyrite powder samples were collected from a slab of ore containing a prominent quartz vein, and two were collected from a slab of ore containing only mineralized host rock. Three vein sulfide and two host matrix sulfide powder samples were also collected. Sulfur isotope compositions were measured using a Thermo Fisher Scientific MAT252 Isotope Ratio Mass Spectrometer (IR-MS) coupled to a Carlo Erba NCS 2500 Elemental Analyzer. Values of $\delta^{34}S$ were calculated by standardizing the measured $^{34}S/^{32}S$ ratios in the samples to Vienna Canyon Diablo Troilite (VCDT) and are reported using the delta (δ) notation in units of per mil (‰) and are reproducible to ± 0.2‰.

3.2 – Laser Raman microscopy

Quantitative laser Raman microscopy was performed on polished chips containing single-phase non-aqueous inclusions and two-phase aqueous inclusions at Saint Mary's University, Halifax, Nova Scotia. The instrumentation used was a Jobin-Yvon Horiba LabRam HR confocal Raman microscope with an 800 mm spectrograph and Synapse 1024 x 256 pixel CCD detector. A 600 groves/mm grating and 25 μm confocal hole size were used for spectrum collection. A 532.21 nm (green) Nd-YAG laser (105 mW laser power at objective) was used to apply energy to the fluid species which was directed through a 100x objective. The frequency calibration standard was

pure silicon. Spectrum collection (single window) over the range 1000-4200 cm^{-1} was done using an acquisition time of 20 seconds per accumulation and 3 accumulations obtained per inclusion analysis. Semi-quantitative determination of relative gas species abundances (in mol%) was done using the empirical quantification parameters and methodologies of Wopenka and Pasteris (1986, 1987), Dubessy et al., (1989), Burke (2001), and Beeskow et al. (2005). The determination of the wavelength-dependent relative Raman scattering cross-sections ($\sigma_{532\ nm}$) for each gas species was obtained by interpolating Table 2 in Burke (2001).

Microthermometrically-determined CO_2 and CH_4 contents were compared to Raman-determined quartz-hosted CO_2-CH_4 standard inclusions from the South Wales Coal Field (Beeskow et al., 2005) in order to calculate instrument efficiencies (ζ) for CO_2 and CH_4. The instrument efficiencies for other gas species were assumed to be 1, in the absence of standards, which lead to slight overestimations of the mole fractions of H_2S, N_2, and H_2. The uncertainties in calculated mole fractions of species present in the carbonic phase of the inclusions are within 20% (relative).

Mole fractions of CH_4, CO_2, N_2, and H_2S from individual fluid inclusions and homogenization temperatures obtained by microthermometry were used to determine bulk densities, modelled using the BULK software routine (Bakker, 2003) using equations applicable to any gas mixture from Bowers & Helgeson (1983), and Bakker (1999). Both an upper quartile (Q3) and a lower quartile (Q1) homogenization temperature associated with the inclusion type (i.e., type-I or type-II) were applied for density determination, yielding a Q1 – Q3 range. The densities of bulk fluid inclusions obtained from BULK were used to calculate isochores using the ISOC software routine

(Bakker, 2003), using equations of state developed by Bakker (1999) and Bowers & Helgeson (1983), with quartz as the host mineral. This calculation yielded isochoric data associated with the entrapment conditions of the fluid inclusions.

Finally, a two-dimensional composition map of CO_2, CH_4, H_2S + N_2 distribution in a single type-I inclusion was obtained using the following operating parameters: an acquisition time of 30 seconds per accumulation, five accumulations per analysis, a 600 grooves/mm grating, a 532.21 nm laser, and a confocal hole size of 25 μm. The laser power out of the aperture was 109 mW, but with a 100X objective that has a very low working distance of 0.21 mm, the laser power is 2.2 mW through the objective.

3.3 – Fluid inclusion microthermometry

A Linkam FTIR 600 temperature-programmable heating-freezing stage mounted on an Olympus BX51 microscope was used at Saint Mary's University to perform microthermometric measurements on fluid inclusions contained in doubly polished quartz chips. Quartz veins with abundant fluid inclusions were selected in three thin sections (Fig. 4.7). Six, 1cm x 1cm chips were cut from the thin sections and were labelled LUP6A, LUP6B, LUP4C, LUP4D, LUP3E, and LUP3F. Calibration of the stage was done using synthetic fluid inclusion standards (Fluid Inc.) containing pure CO_2 (melting at -56.6˚C) and pure, critical density H_2O (melting at 0˚C and homogenizing by supercritical behavior at 374.1˚C). Repeat analyses of these standards indicated total uncertainties on measured temperatures of ± 0.2˚C for phase changes observed at a heating rate of 1˚C/min. The programs BULK and ISOC (Bakker, 2003; equations of state from Duan et al., 1992a, 1992b) were used to calculate densities (g/cc) and corresponding isochores for carbonic (non-aqueous) inclusions based on the temperature

of homogenization of the carbonic phase (T_h) and mode of homogenization for the carbonic phase (to liquid, vapor, or by supercritical behavior). For aqueous inclusions, salinities were calculated using the equation of Bodnar and Vityk (1994) from final ice melting temperatures (T_m^{ICE}) and isochores were determined using the model and program SOWAT (Driesner, 2007; Driesner and Heinrich, 2007).

3.4 – In-line rock-crushing gas chromatography

In-line, rock-crushing gas chromatography analysis of volatiles liberated from vein quartz was performed at the Saint Mary's University Mineral Exploration and Ore Fluids Laboratory, Halifax, Nova Scotia. Analysis was completed using a method modified after Andrawes and Gibson (1979) and Andrawes et al., (1984). Samples were crushed in stainless-steel, hydraulically-driven, air-tight crushers with adjustable helium gas flow that carries liberated volatiles to an analytical column to be separated and analyzed (Kerr et al., 2015). Technicians at the University of Toronto Machine Shop customized the stainless steel, hydraulically-driven rock crushers based on the designs of Bray and Spooner (1992) and Bray et al., (1990), which are revised designs of Andrawes and Gibson (1979) and Andrawes et al., (1984). The newly designed in-line technique improves detection levels for trace volatiles in fluid inclusions and is done under lower operating temperatures than traditional off-line techniques, such as *in* vacuo thermal decrepitation, to avoid thermal degradation and helps to minimize issues such as adsorption, unwanted chemical reactions and gas loss upon crushing.

Samples were studied using an Agilent 7890 series gas chromatograph fitted with applicable valve and injection systems from Wasson-ECE Instrumentation (Kerr et al., 2015). A flame ionization detector (FID) capable of performing analyses of combustible

compounds, such as alkanes, was set up in sequence with an Alumina-PLOT capillary analytical column (50 mm x 0.53 mm x 10 μm). Immediate volatilization of all captured fluids was achieved by crushing samples at temperatures ranging from ~105-110˚C. Ensuing helium gas carried the volatiles to the analytical column at a flow rate of 8.5 ± 0.5 ml/min.

The FID chosen for this experiment is the most commonly used detector for gas chromatography (Fig. 3.1). Effluent from the column was directed into a modest air-hydrogen flame. The temperature of this flame caused the organic compounds to be pyrolyzed which produced ions and electrons. These charged particles were collected which produced an electric current. A high-impedance picoammeter measured this current which was roughly 10^{-12} amperes. These measurements of electrical current were manually converted to compound concentrations (in moles, or ppm).

For hydrocarbon analysis, the FID has a high sensitivity (~10^{-13} g/s), several orders of magnitude in linear response range (~10^{7}), and low noise. The FID has a few disadvantages; namely, it destroys the sample upon combustion and requires additional operational gases and controllers. For this reason, a thermal conductivity detector (TCD) was used for the non-destructive detection of non-hydrocarbon species, such as CO_2. One quartz sample of 0.6 grams was used for light hydrocarbon analysis using only the FID, whereas two other quartz samples from the same vein selvage were analyzed using the TCD and FID in series.

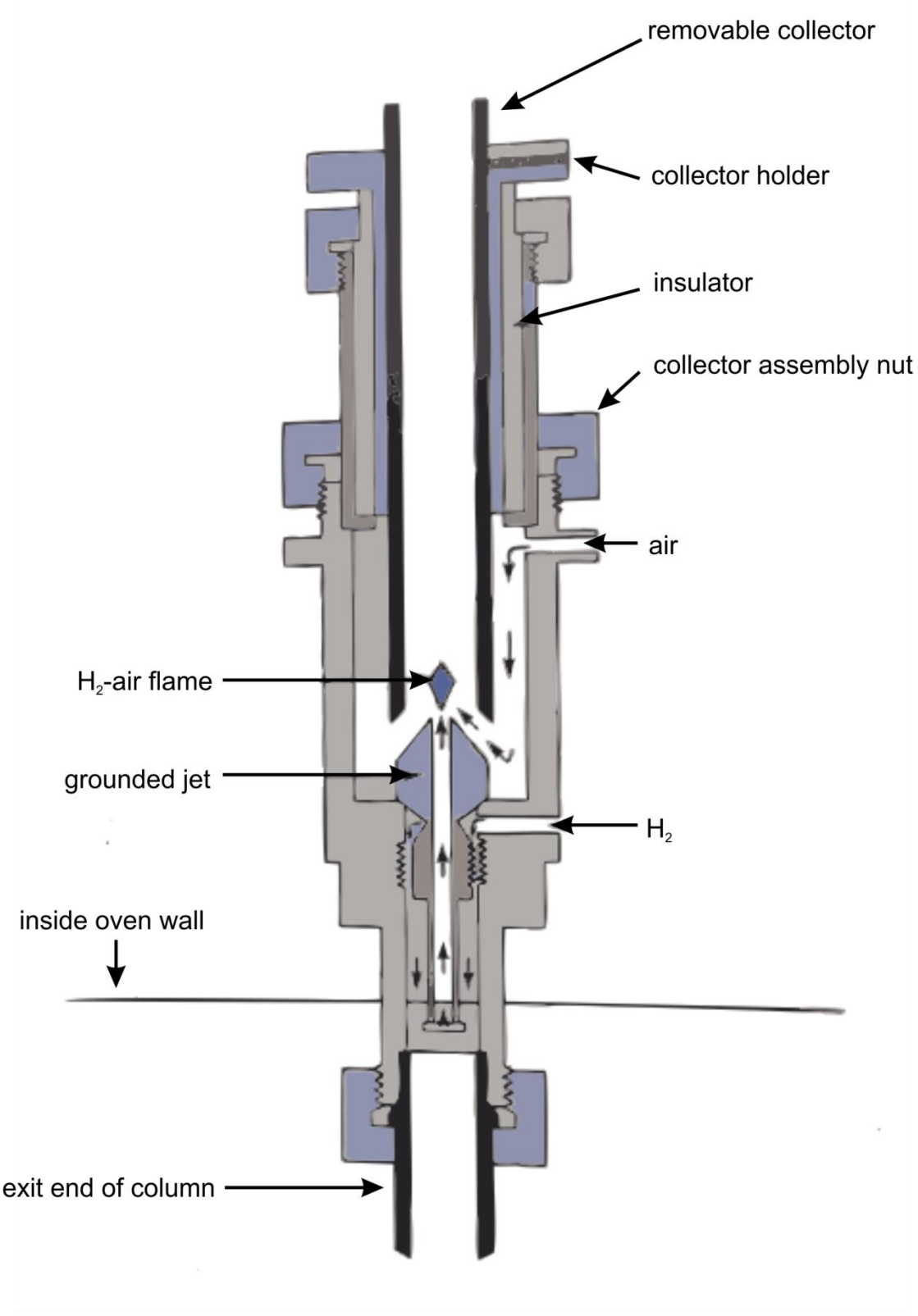

Figure 3.1: Flame ionization detector schematic. A typical flame ionization detector with components labelled. Image modified from Skoog, Holler, and Crouch (2007).

3.5 – Trace and major element mapping of arsenopyrite by LA-ICP-MS

Laser ablation inductively-coupled plasma mass spectrometry (LA-ICP-MS) was performed at Laurentian University, Sudbury, Ontario, on individual arsenopyrite grains to obtain spatially resolved major and trace element concentrations across entire grain cross sectional areas. The instrumentation used to produce the analyte concentration maps was a Thermo Scientific X Series II Ar plasma quadrupole ICP-MS coupled to a Resonetics RESOlution M-50 laser ablation system comprised of a 193 nm, 20 ns pulsed ArF excimer laser ablation microprobe. For fast washout characteristics, a two-volume Laurin Technic sample cell was utilized. Each isotope mass was measured on a 10 ms dwell time, carrier gas flow rates of 0.65 l/min, 0.85 l/min, and 6 ml/min for He, Ar, and N_2, respectively, and laser energy density of 7 J/cm^2. The maps were produced by linearly rastering the laser over the region of interest with 30 seconds of washout between individual spots. The parameters applied for trace element mapping of arsenopyrite were optimized for each of the grain areas mapped. Repetition rates ranged from 6 to 7 Hz, beam diameters from 48 μm to 90 μm, and scan speed from 24 μm/s to 45 μm/s).

The raw data were quantified and compiled into maps using the Iolite software package (Paton et al. 2011), with synthetic NIST SRM 610 glass as an external reference material, and scaling concentrations using an average (grain-wide) Fe content in arsenopyrite of 34.4 wt% as an internal reference, and BHVO-2G glass and Po725 PGE+Au doped Po (Sylvester et al. 2005) as quality control monitors. For complete operating conditions of the LA-ICP-MS system, see Appendix A.

3.6 – SEM analysis

SEM and BSE images and quantitative analyses of electrum and arsenopyrite were obtained using a LEO 1450VP SEM at Saint Mary's University, operated with a beam current of 3.2 nA, an accelerating voltage of 25 kV, and a working distance range of 17–21 mm. The SEM imaging system was equipped with an Oxford Instrument INCA X-max 80 mm^2 silicon drift detector (SDD) energy dispersive spectrometer (EDS) detector linked to a desktop computer (INCA software). Quantification was performed using in house mineral standards of known composition (pyrite, millerite, nickeline, and pentlandite).

Chapter 4 – Results

4.1 – C-N-S isotope systematics of vein inclusion fluids and associated sulfides in host rocks

The $\delta^{13}C_{VPDB}$ values are bulk analyses of a mixture of hydrocarbon and carbonic fluids from vein quartz. Five measurements of these fluids released from two quartz samples showed a $\delta^{13}C_{VPDB}$ distribution of -29.9 to -22‰, which falls within the thermogenic range (Fig. 4.1). However, this isotopic distribution also overlaps with the $\delta^{13}C_{CH4}$ range of hydrocarbons contained in quartz of peralkaline granitic rocks and generated by Fischer-Tropsch-type (F-T-t) reactions, with CO_2 as the initial magmatic gas phase (Fig. 4.1). This relationship is also demonstrated by an overlap with a well-established F-T-t-CH_4 isotopic distribution field on a $\delta^{13}C$-δD diagram (Fig. 4.2). The $\delta^{13}C$ distribution also overlays three major compositional fields: Canadian Shield groundwaters, fumaroles and hotsprings, and Scandinavian shield rocks. The carbon

isotopic composition of the vein fluids is compared to other deposits of various rock types and localities in Table 3. The most similar $\delta^{13}C$ range in Table 3 comes from fluids contained in quartz from Strange Lake pegmatites hosted in a subsolvus granite (-32.0 to -19.7‰). Furthermore, the quartz vein-hosted CH_4 in alkali granite and augite syenite found on the northern and southern edges of the Ilímaussaq complex in Greenland has a broad $\delta^{13}C_{CH4}$ range (-43.4 to -22.6‰) that overlaps the range in this study.

Similar to carbon, the N_2 isotope data is representative of a bulk analysis of fluids trapped in vein quartz. There could also be contributions of N_2 from impurities in the vein quartz (e.g., mica grains); however, these contributions were minimalized by selecting clean quartz samples with the aid of a stereoscopic microscope. Only one quartz sample yielded a signal for N_2 that was above the detection capabilities. The $\delta^{15}N_{AIR}$ value reported is +7.4‰ and falls within ranges of several other sample types that are equivalent in terms of metamorphic rock type, with similar protolith sources and metamorphic mineral sinks for N. For example, the upper Kalevian amphibolite grade mica-schists of the Talvivaara area in Kainuu, Finland have an isotopic range of +4.9 to +7.8‰ and represent turbiditic deep-water graywackes with intercalated black shales (Fig. 4.1; Table 5). In addition, the amphibolite-grade banded, garnet-bearing quartz + plagioclase + biotite + muscovite schists of the Glenfinnian Division, Moine succession in the northern Highlands of Scotland have an isotopic range of +7.2 to +8.2‰(Fig. 4.1; Table 5). Phanerozoic marine sedimentary organic matter has a range of 0 to +10‰ (Fig. 4.1; Table 5). Finally, kerogens in Proterozoic cherts from marine, lacustrine and alluvial settings have a range of +0.3 to +10.1‰ (Fig. 4.1; Table 5). The $\delta^{15}N_{AIR}$ value from this

study is included in a table with other rock types of varying localities with their associated isotopic distributions (Table 5).

Sulfides (n = 10) have a $\delta^{34}S_{VCDT}$ range of +1.8 to +3.4‰ (Table 6), which falls within the magmatic range (Fig. 4.1). The magmatic range is based on the sulfur isotopic composition that is traditionally thought to represent the mantle (Thode et al., 1961). However, there can be a wider range of $\delta^{34}S$ values for material derived from the mantle. For example, peridotitic diamonds are considered to have a strictly mantle source and typically have sulfide inclusions with $\delta^{34}S$ values ranging from -5 to +5‰ (Eldridge et al., 1995). Sulfur of magmatic values can be mobilized during metamorphic processes. Figure 4.1 shows that the $\delta^{34}S$ values in this study overlap with those of pyritic shale from both the Barberton Greenstone Belt, South Africa (-0.8 to +4.4‰) and the Bubi Greenstone Belt, Zimbabwe (-0.5 to +8.2‰). In addition, the $\delta^{34}S$ values are similar to those of pyrite found in microbial mats of the Dresser Formation, Pilbara Craton, Western Australia (+1.6 to +6.7‰) and pyrite hosted in stromatolites, cherts, and sandstones of the Jeerinah Formation, Western Australia (-2.5 to +5.6‰). There is also $\delta^{34}S$ overlap with volcano-sedimentary-hosted pyrite and chalcopyrite of the Tumbiana Formation, Pilbara Craton, Western Australia (-5.73 to +2.75‰). Finally, Fig. 4.1 demonstrates that the $\delta^{34}S$ values of this study are similar to those of the BIF-hosted pyrite and chalcopyrite of the Quadrilátero Ferrifero, Minas Gerais state, Brazil (+1.5 to +5.1‰) and the Temagami iron formation, Ontario, Canada (sediment-hosted suite = -0.2 to +3.0‰; volcanic-hosted suite = -6.3 to +2.9‰). All $\delta^{34}S$ values of various Archean sediment-hosted or associated deposits used for comparison in this study are presented in Table 7. The two $\delta^{34}S$ ranges that most closely resemble the measured sample range are

from the volcano-sedimentary-hosted massive chalcopyrite of the Salobo deposit in Carajás, Brazil (+1.6 to +2.9‰) and the oxide facies BIF-hosted pyrite of the Amalia Greenstone Belt in South Africa (+1.8 to +2.5‰) (Table 7).

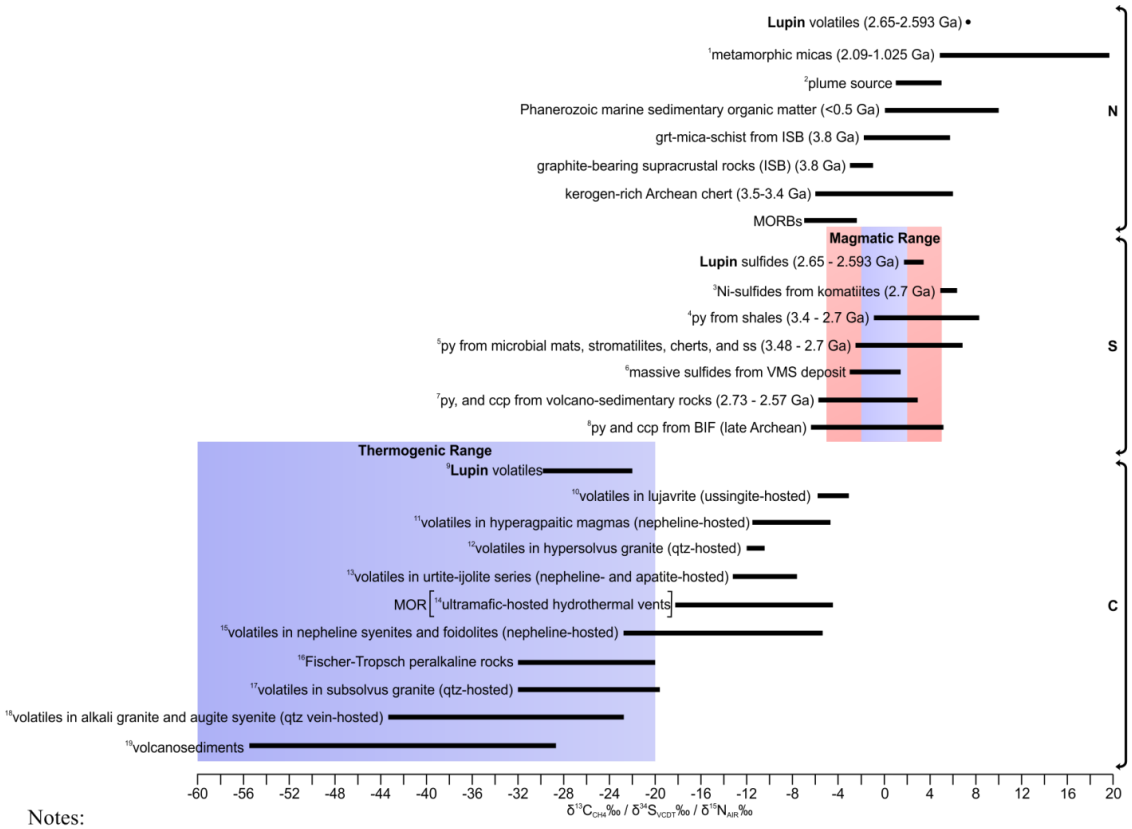

Notes:

[1]Metamorphic micas from amphibolite grade mica- and biotite-schists from Talvivaara, Finland and the Moine succession in Scotland, respectively (Papineau et al., 2005)

[2]Plume sourced rocks from the Kola Peninsula, Russia (Marty & Dauphas, 2002)

[3]Komatiites of the Alexo Mine, Abitibi Greenstone Belt, Ontario, Canada (Bekker et al., 2009)

[4]Shales from both the Barbeton Greenstone Belt, South Africa (3.4 – 3.1 Ga) and the Bubi Greenstone Belt, Zimbabwe (2.7 Ga) (Kakegawa & Ohmoto, 1999; Marin-Carbonne et al., 2014)

[5]Microbial mats of the Pilbara Craton (Dresser Formation, Western Australia – 3.48 Ga) and stromatolites, cherts, and sandstones of the Jeerinah Formation, Western Australia (2.7 Ga) (Wacey et al., 2015; Kakegawa & Nanri, 2006)

[6]VMS deposit of the Kidd Creek Mine, Abitibi Greenstone Belt, Ontario, Canada (Jamieson et al., 2006)

[7]Volcano-sedimentary rocks of various localities: Tumbiana Formation, Pilbara Craton, Western Australia (2.73 Ga); and Salobo sulfide deposit, Carajás, Brazil (2.57 Ga) (Thomazo et al., 2009; Bühn et al., 2012)

[8]BIF of various localities: Quadrilátero Ferrífero, Minas Gerais state, Brazil (2.72 – 2.7 Ga); Amalia Greenstone Belt, South Africa; and Temagami iron formation, Ontario, Canada (Bühn et al., 2012; Adomako-Ansah et al., 2012; Bowins, & Crocket, 1994)

[9]Carbon isotope distribution is based on bulk analyses of a mixture of hydrocarbon species, and CO2; however, gaschromatography shows that CH4 is by far the most abundant species

[10]North coast of the Tunulliarfik fjord, Illímaussaq complex, Greenland (Graser et al., 2008)

[11]Lovozero complex samples from a range of rock types, including: urtite, foyaite, lujavrite, eudialyte lujavrite and loparite juvite (Potter et al., 2013)

[12]Strange Lake agpaitic pegmatite hosted in hypersolvus granite (Potter et al., 2013)

[13]Silica-undersaturated peralkaline complex, Yuksporr mine, Khibina complex, Kola Peninsula (Voytov, 1992)

[14]Water samples from hydrothermal vents from the Rainbow, and Lost City complexes of the Mid Atlantic Ridge and from the 21° EPR complex of the East Pacific Rise (Charlou et al., 2002; Proskurowski et al., 2008; Whelan & Craig, 1983)

[15]Khibina complex, Kola Peninsula (Beeskow et al., 2006)

[16]Fischer-Tropsch-type hydrocarbon generation in quartz-bearing peralkaline granitic rocks with CO2 as the initial magmatic gas phase (Potter et al., 2013)

[17]Strange Lake pegmatite hosted in subsolvus granite and subsolvus peralkaline granite (Potter et al., 2013)

[18]Northern and southern edge of Ilímaussaq complex, Greenland (Graser et al., 2008)

[19]Volcanosediments from the Witswatersrand complex, South Africa (Sherwood-Lollar et al., 2006)

Figure 4.1 (see previous page): Nitrogen, sulfur, and carbon isotope compositions of various terrestrial reservoirs relevant for comparison to Lupin samples. . The nitrogen isotopic distribution of quartz fluid inclusions (n=1) is compared to stable N_2 isotope signatures of various sources, such as: metamorphic micas, continental crust, plume, organic matter in oceanic sediments, garnet-mica schists, graphite-bearing supracrustal rocks, Archean chert, and mid-ocean ridge basalts. The sulfur distribution of sulfides (n=10) is compared to the stable sulfur isotope signatures of other rock types, such as: komatiites, shales, microbial mats, stromatolites, cherts, sandstones, VMS deposits, BIF, and volcano-sedimentary rocks. The traditional magmatic range for sulfur is represented by the blue polygon, whereas the red polygon covers a wider range of magmatic material (e.g., peridotitic diamonds). The carbon isotopic distribution of quartz fluid inclusions (n=5) is compared to CH_4 stable carbon isotope signatures of other types of rocks, such as: hydrothermal rocks, peralkaline rocks, volcanosediments, and rocks of the Canadian Shield. The thermogenic range for carbon is denoted by the blue polygon.

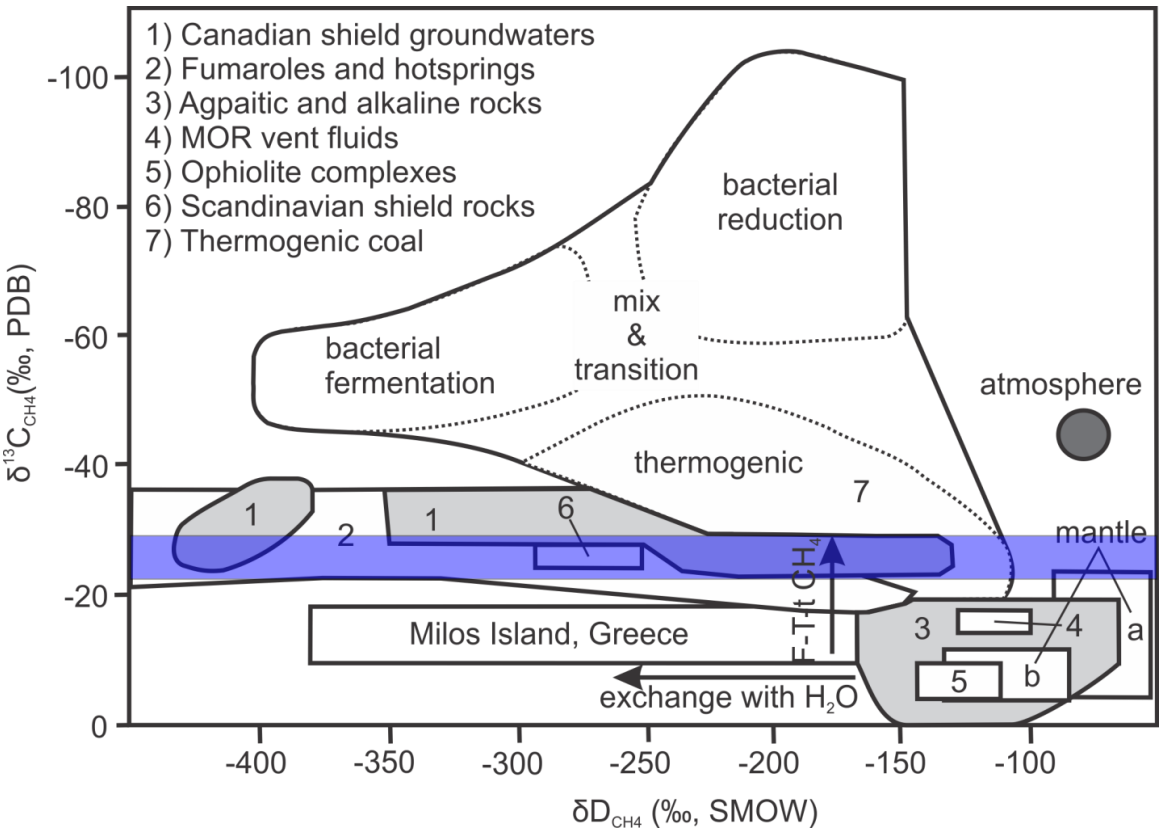

Figure 4.2: Isotopic distribution fields related to CH_4 source. Well-established CH_4 fields on a $\delta^{13}C$ versus δD diagram. The arrows represent CH_4 isotopic composition shifts with response to exchange with H_2O or because of Fischer-Tropsch-type reactions (F-T-t CH_4). The transparent blue polygon represents the range of $\delta^{13}C$ of the current study. Diagram modified from Potter et al. (2013).

Table 2: C isotope data for bulk fluids contained in Lupin quartz veins

Sample	Mineral type	$\delta^{13}C_{VPDB}$(‰)
Lupin_1	quartz	-26.7
Lupin_1	quartz	-25.8
Lupin_2	quartz	-29.9
Lupin_2	quartz	-22.0
Lupin_2	quartz	-23.8

Notes: Samples Lupin_1 and Lupin_2 weighed 3.5 and 4.5 g, respectively. The $\delta^{13}C$ values are bulk analyses of a mixture of hydrocarbons and carbonic fluids

Table 3: C isotope data for fluids contained in Lupin quartz veins compared to isotope data of various metamorphic and igneous settings

Locality	Complex	Rock Type	[1]$\delta^{13}C$	$\delta^{13}C_{CO2}$	$\delta^{13}C_{CH4}$	Reference
Russia	Lovozero	[2]hyperagpaitic magmas	-	-	−11.6 to −4.7	Potter et al. (2013)
Canada	Strange Lake	[3]agpaitic pegmatite	-	−21.5 to −16.0	−12.0 to −10.3	Potter et al. (2013)
Canada	Strange Lake	[4]pegmatite	-	−2.0 to −1.8	−32.0 to −19.7	Potter et al. (2013)
[5]various vent fields, EPR	21° EPR	hydrothermal fluids	-	-	−17.6 to −15.0	Whelan and Craig (1983)
Amar segment, MAR	Rainbow	ultramafic-hosted hydrothermal	-	−4.0 to −3.0	−18.2 to −13.0	Charlou et al. (2002)
Lost City, MAR	Lost City	ultramafic-hosted hydrothermal	-	-	−13.6 to −9.4	Proskurowski et al. (2008)
Canadian shield	Kidd Creek Mine	crystalline basement	-	-	−40.7 to −32.7	Sherwood-Lollar et al. (2002)
South Africa	Witswatersrand	volcanosediments	-	-	−55.5 to −28.7	Sherwood-Lollar et al. (2006)
Yuksporr mine	Khibina	[6]silica-undersaturated peralkaline	-	−18.6 to −14.6	−13.3 to −7.6	Potter and Longstaffe (2007)
Kola peninsula	Khibina	[7]nephaline syenites and foidolites	-	-	−22.4 to −5.4	Beeskow et al. (2006)
Greenland	Ilímaussaq	alkali granite and augite syenite	-	−21.0 to −4.6	−43.4 to −22.6	Graser et al. (2008)
Tunulliarfik fjord	Ilímaussaq	lujavrite (ussingite-hosted)	-	−17.3 to −4.6	−5.9 to −3.1	Graser et al. (2008)
various MORBs	-	MORB	-5.9 to -4.5	-	-	Marty and Zimmermann (1999)
Nunavut, Canada	Yellowknife group	BIF	-29.9 to -22	-	-	this study

Notes and abbreviations: Minimum and maximum $\delta^{13}C$ values are shown in per mil (‰).
[1]The carbon isotope distribution of $\delta^{13}C$ represents a bulk analysis of a mixture of hydrocarbon and carbonic species
[2]Lovozero samples are from a range of rock types (urtite, foyalite, lujavrite, eudialyte lujavrite, and loparite juvite) present in the complex. Fluids are mainly hosted in nepheline
[3]Strange Lake pegmatite hosted in a hypersolvus granite. Fluids are hosted in quartz
[4]Strange Lake pegmatite hosted in a subsolvus granite and a subsolvus peralkaline granite. Fluids are hosted in quartz
[5]Vent fields include: the National Geographic Society site, the Ocean Bottom Seismometer site, and the Southwest Vents
[6]Hydrocarbon gas inclusions in nepheline and apatite from the urtite-ijolite series at the Yuksporr mine
[7]Hydrocarbon gas inclusions in nepheline found in a variety of nepheline syenites and foidolites
BIF = Banded Iron Formation; EPR = East Pacific Rise; MAR = Mid Atlantic Ridge; MORB = Mid-Ocean Ridge Basalt

Table 4: N isotope data for fluids contained in Lupin quartz veins

Sample	Mineral type	$\delta^{15}N_{AIR}$(‰)	Notes
Lupin_1	vein quartz	-3.3	no N_2 peak
Lupin_1	vein quartz	-2.3	no N_2 peak
Lupin_2	vein quartz	-4.9	no N_2 peak
Lupin_2	vein quartz	-4.8	no N_2 peak
Lupin_2	vein quartz	+7.4	N_2 peak

Notes: Samples Lupin_1 and Lupin_2 weighed 3.5 and 4.5 g, respectively. Contributions of N from impurities in the quartz (e.g., mica grains) were minimized through the selection of clean quartz samples via careful hand-picking from crushed samples with the aid of a binocular microscope

Table 5: N isotope data for fluids contained in Lupin quartz veins compared to isotope data of various metamorphic, igneous, and sedimentary settings

Locality/Source	Rock Type	$\delta^{15}N_{AIR}$(‰)	Reference
[1]Talvivaara, Kainuu, Finland	amphibolite grade mica-schists	+4.9 to +7.8	Papineau et al. (2005)
[2]Moine succession, Scotland	amphibolite grade biotite-schists	+7.2 to +8.2	Boyd and Philippot (1998)
Southern West Greenland (ISB)	garnet-mica-schists	-1.9 to +5.9	Papineau et al. (2005)
Southern West Greenland (ISB)	graphite-bearing supracrustal	-3 to -1	van Zuilen et al. (2005)
Kola peninsula, Russia	carbonatites (plume source)	+1 to +5	Marty and Dauphas (2002)
continental crust sources	continental crust	+2 to +6	Marty and Dauphas (2002)
mantle sources	MORBs	-7 to -3	Marty and Dauphas (2002)
asthenospheric mantle source	MORBs	-4.3 to -2.3	Marty and Zimmermann (1999)
oceanic sediment source	modern sedimentary organic matter	0 to +10	Beaumont and Robert (1999)
marine, lacustrine, alluvial	kerogen-rich cherts	+0.3 to +10.1	Beaumont and Robert (1999)
Archean cherts	kerogen-rich cherts	-6 to +6	Beaumont and Robert (1999)
Nunavut, Canada	BIF	7.4	this study

Notes and abbreviations: Settings are a variety of both magmatic and metamorphic. The metamorphic settings include Archean greenstone belts and other orogenic settings. Minimum and maximum $\delta^{15}N$ values are shown

[1]Upper Kalevian amphibolite grade mica-schists of the Talvivaara area in Kainuu, Finland. The mica-schists represent turbiditic deep-water graywackes with intercalated black shales

[2]Amphibolite grade banded, garnet-bearing quartz+plagioclase+biotite+muscovite schists of the Glenfinnian Division, Moine succession, northern Highlands, Scotland

ISB = Isua Greenstone Belt; BIF = Banded Iron Formation; MORB = Mid-Ocean Ridge Basalt

Table 6: S isotope data for sulfides in quartz veins and wall-rocks at Lupin

Sample	Mineral type	Mass (mg)	$\delta^{34}S_{VCDT}$(‰)
1	host arsenopyrite	16.9	+3.1
2	host arsenopyrite	38.5	+3.4
3	vein arsenopyrite	18.8	+3.4
4	vein arsenopyrite	32.1	+3.3
5	vein arsenopyrite	27.2	+3.0
6	host matrix sulfides	19.9	+2.5
7	host matrix sulfides	32.5	+2.7
8	vein matrix sulfides	15.1	+2.5
9	vein matrix sulfides	15.3	+2.9
10	vein matrix sulfides	18.1	+1.8

Notes: Host arsenopyrite and host matrix sulfides were sampled from mineralized host rock with no proximal quartz vein. Vein arsenopyrite and vein matrix sulfides were sampled from a slab of ore containing a prominent quartz vein. Mineral types labeled as “sulfides” are dominantly pyrrhotite with very minor pyrite

Table 7: S isotope data for sulfides in Lupin quartz vein selvages and wall rocks compared to isotope data of various Archean sediment-hosted or associated deposits

Locality	Formation/Complex/Deposit	Mineral/Rock Type	$\delta^{34}S_{VCDT}$(‰)	Reference
Carajás, Brazil	Salobo sulfide deposit	massive chalcopyrite from volcano-sedimentary rocks	+1.6 to +2.9	Bühn et al. (2012)
Carajás, Brazil	Serquerinha sulfide deposit	chalcopyrite	+0.2 to +0.9	Bühn et al. (2012)
Minas Gerais	Quadrilátero Ferrífero	massive pyrite and chalcopyrite from BIF	+1.6 to +5.1	Bühn et al. (2012)
Zimbabwe	Bubi Greenstone Belt	pyrite from shale	-0.5 to +8.2	Marin-Carbonne et al. (2014)
South Africa	Amalia Greenstone Belt	pyrite from oxide facies BIF	+1.8 to +2.5	Adomako-Ansah et al. (2012)
South Africa	Barbeton Greenstone Belt	pyrite from shale	-0.8 to +4.4	Kakegawa and Ohmoto (1999)
Ontario, Canada	Temagami iron formation	pyrite from BIF (sediment-hosted suite)	-0.2 to +3	Bowins and Crocket (1994)
Ontario, Canada	Temagami iron formation	pyrite from BIF (volcanic-hosted suite)	-6.3 to +2.9	Bowins and Crocket (1994)
Ontario, Canada	Boston iron formation	pyrite from BIF	-4.7 to +1.1	Bowins and Crocket (1994)
Kidd Creek Mine	Abitibi Greenstone Belt	massive sulfides from VMS deposit	-3 to +1.4	Jamieson et al. (2006)
Alexo mine	Abitibi Greenstone Belt	nickle sulfide minerals from komatiites	+4.8 to +6.2	Bekker et al. (2009)
Western Australia	Dresser Formation	pyrite from microbial mat	+1.6 to +6.7	Wacey et al. (2015)
Western Australia	Tumbiana Formation	pyrite from sediments	-5.73 to +2.75	Thomazo et al. (2009)
Western Australia	Jeerinah Formation	pyrite from stromatolites, cherts, and sandstones	-2.5 to +5.6	Kagegawa and Nanri (2006)
Lupin, Nunavut	Contwoyto Formation	pyrite, arsenopyrite, and matrix sulfides from BIF	+1.8 to +3.4	this study

Notes: A variety of magmatic, sedimentary, and metamorphic settings are represented. Minimum and maximum $\delta^{34}S$ values are shown

4.2 – Ore petrography and mineral compositions

The petrography of a vein and vein selvage is depicted in Fig. 4.3. Polished slabs of mineralized veins exhibit quartz veins that cross-cut sulfidic BIF containing pyrite, pyrrhotite, chlorite, grunerite, loellingite, and arsenopyrite. There are layers of coarse- and fine-grained sulfidic BIF which represent metamorphosed graywacke and pelitic beds, respectively. The same vein selvages show seven distinct gold textural styles (Fig. 4.4). The seven textural occurrences or styles are: (1) fracture fill or inclusion in massive sulfide, (2) fracture fill in arsenopyrite-loellingite, (3) inclusion in arsenopyrite-loellingite, (4) fracture fill or inclusion in qtz, (5) interlamination inclusion, (6) inclusion along amphibole-sulfide boundary, and (7) inclusion along chlorite-sulfide boundary. Occurrence types 1, 6, and 7 are shown in SEM-BSE images (Fig. 4.5). In the majority of cases, gold grains are intimately associated with mineral phases that grew as a result of vein overprinting (e.g., chlorite in frame (a) of Fig. 4.5). Grains can also be secondary with respect to host phases, occurring interstitial to or as fracture infillings in silicates and sulfides (e.g., hornblende and pyrrhotite-pyrite in frames (b) and (c) of Fig. 4.5). Essentially, Fig. 4.5 illustrates the late nature of the gold, hosted in chlorite, crosscutting hornblende and hosted in quartz filled fractures in matrix sulfides. Fracture fill in arsenopyrite-loellingite (occurrence type 2) is a good example of a late Au depositional texture and, when investigated using X-ray EDS mapping, shows that Au in this infilling co-precipitated with Cu (as chalcopyrite), magnetite, and pyrrhotite, an assemblage that constrains the conditions of Au precipitation (see Section 4.6; Fig. 4.6).

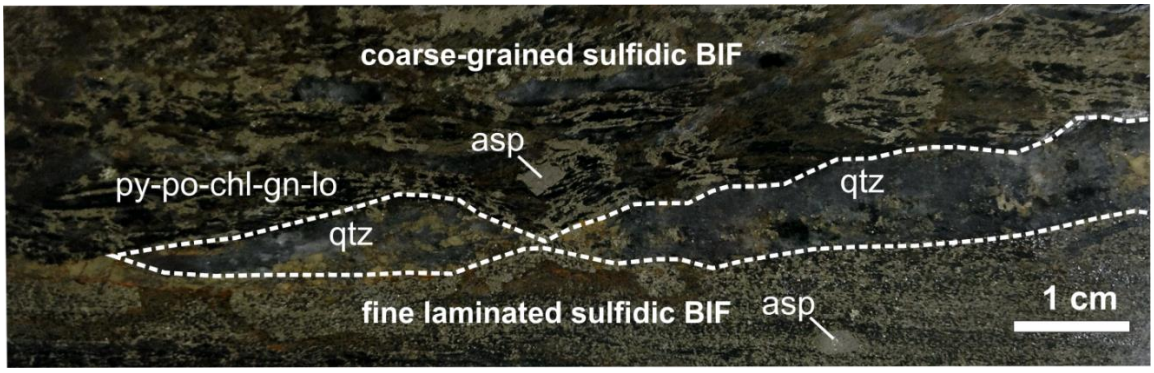

Figure 4.3: Polished slab of ore showing a cross-cutting quartz vein in sulfidic BIF. Polished slab showing a late stage boudinaged ribbon-textured quartz (qtz) vein. Host rock is sulfidic BIF containing pyrite (py), pyrrhotite (po), chlorite (chl), grunerite (gn), loellingite (lo), and arsenopyrite (asp) grains. This mineral assemblage is characteristic of vein selvages.

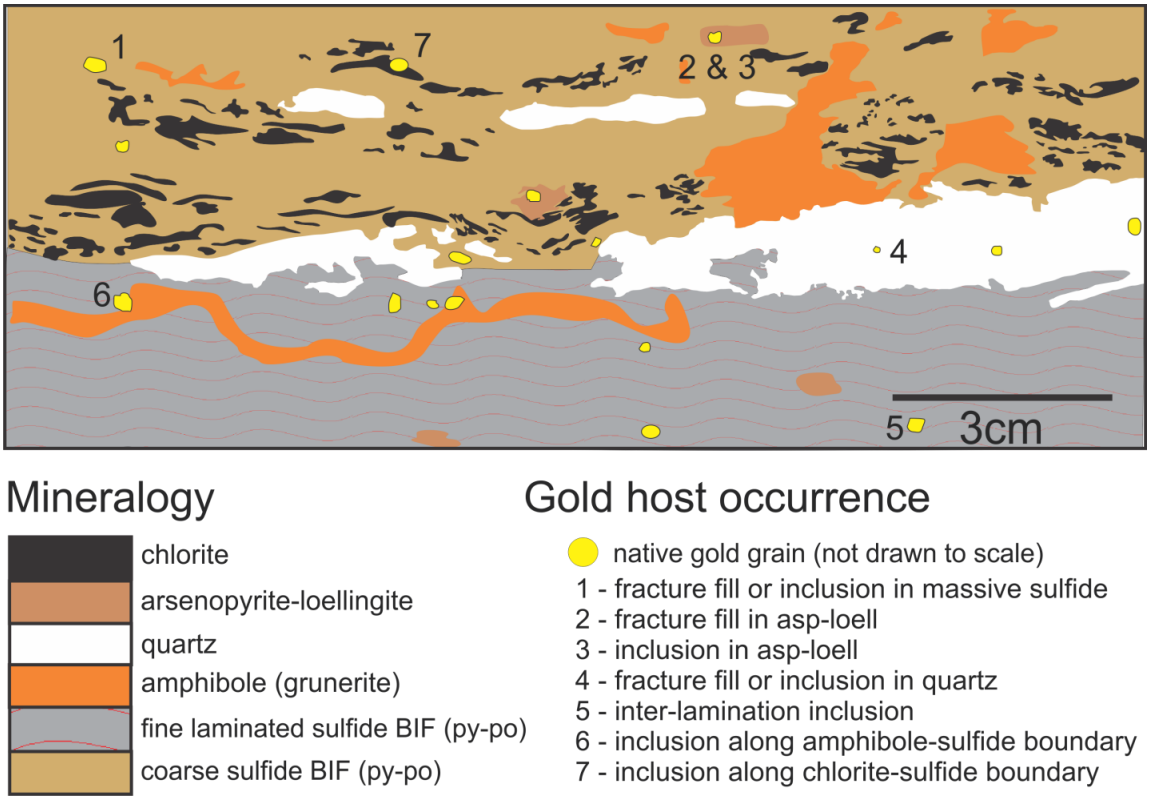

Figure 4.4: Sketch of an ore slab vein selvage showing seven typical gold textural occurrences or styles drawn from the image in Fig. 4.3. Occurrences 1 (fracture fill), 2, 3, and 7 are most common. The fracture fill textural occurrences speak to the secondary nature of gold mineralization in proximity to the quartz veins.

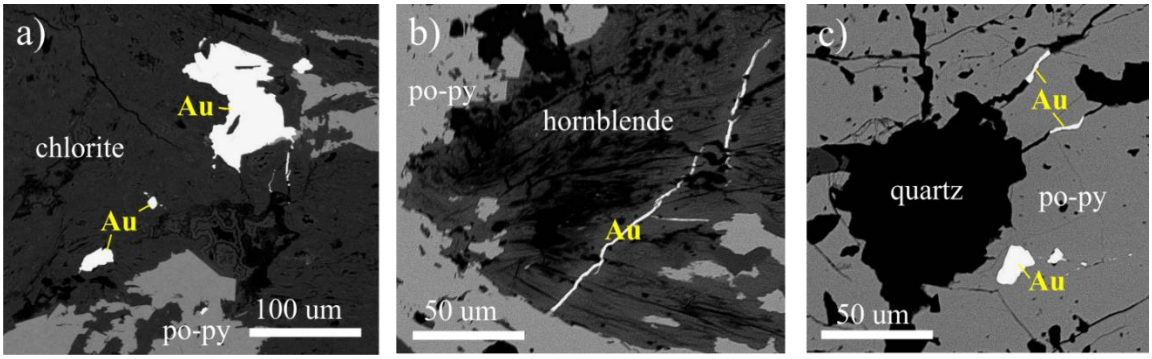

Figure 4.5: SEM-BSE images of gold textures. SEM-BSE images showing common gold textural associations surrounding quartz veins. (a) Gold inclusions in chlorite grain within a pyrrhotite-dominant matrix (occurrence type 7). (b) Gold fracture infill in chloritized hornblende grain within a pyrrhotite-dominant matrix (occurrence type 6). (c) Interstitial gold infill and inclusions in pyrrhotite-dominant matrix (occurrence type 1).

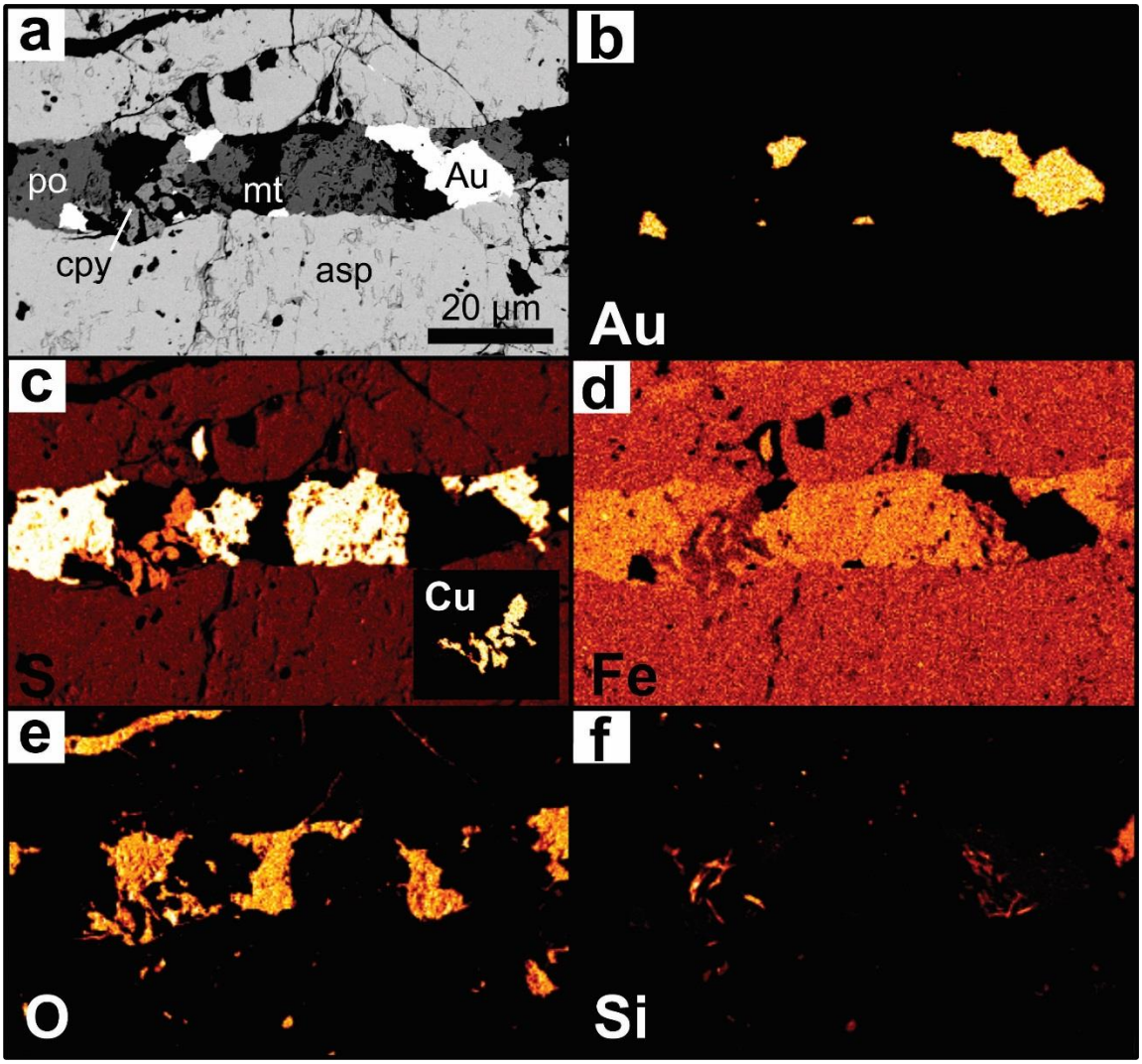

Figure 4.6: Mosaic of X-ray elemental intensity maps depicting a late pyrrhotite-electrum vein (i.e., inclusion fracture fill) crosscutting an arsenopyrite (asp) grain. a) Late pyrrhotite-electrum vein containing electrum (Au), magnetite (mt), chalcopyrite (cpy), and pyrrhotite (po) which is hosted in an arsenopyrite-loellingite grain. b) Distribution of elemental Au (in electrum). c) Distribution of S (in chalcopyrite, pyrrhotite, and arsenopyrite) with inset of Cu (in chalcopyrite). d) Distribution of Fe (in magnetite, arsenopyrite, pyrrhotite, chalcopyrite). e) Distribution of O (in magnetite, and quartz). f) Distribution of Si (in quartz). Gold remobilization is late with respect to arsenopyrite formation, as shown by Au-bearing inclusion fracture fills in arsenopyrite (frame (a)). Gold deposition came after the formation of arsenopyrite alteration haloes associated with quartz vein emplacement and therefore likely postdates quartz vein formation.

4.3 – Fluid inclusion petrography and microthermometry

Three types of petrographically distinct fluid inclusion assemblages (FIAs) were observed in late-stage (cross-cutting auriferous sulfidic BIF) crack-seal and ribbon-textured quartz veins (Fig. 4.3; and Fig. 4.7). Inclusions were considered to be of the same FIA if they were in the same trail or cluster, while similar homogenization temperatures were used as supportive criteria for FIA identification. Non-aqueous type-I fluid inclusions occur in planar arrays that crosscut healed grain boundaries (Fig. 4.7). Non-aqueous type-II fluid inclusions follow healed grain boundaries (Fig. 4.7). Aqueous type-III inclusions contain a vapor bubble and can occur in groups with the non-aqueous inclusions, or as isolated clusters (Fig. 4.7). Petrographic observations show that type-I inclusions are late secondary (LS) in origin because they crosscut healed grain boundaries that host type-II inclusions which are early secondary (ES) in origin (Table 8). All fluid inclusions ranged in diameter from 4.5μm (lower quartile, Q1) to 7.5μm (upper quartile, Q3), with an average diameter of 6.4 μm (Table 8).

Chips LUP6B and LUP3F did not provide reliable thermometric results due to inclusions being too small to measure at the optical resolution of the microscope set-up, or due to suspected post-entrapment leakage. Measurements in this study were acquired from Chips LUP6A, LUP4C, LUP4D, and LUP3E (Table 8). Fourteen type-I FIAs were studied and could not be frozen using liquid N_2 (-196ºC), but homogenized (T_h) to a liquid phase between -89.5°C (lower quartile, Q1) and -88.8°C (upper quartile, Q3), with an average T_h of -89.9°C (Table 8; Fig. 4.8). Type-I inclusions found in the same FIA exhibited similar $T_{h,}$ with an average range of 0.6°C between the lowest and highest homogenization temperatures (note: this calculation does not include FIAs 1 and 2 which

have anomalous ranges in T_h). Upon homogenization, the two-phase (liquid and vapor) carbonic fluid transitioned into a single-phase liquid carbonic fluid. Three type-II FIAs were studied and had an average freezing temperature of -102.4°C, and homogenized mainly to liquid between -25.6°C (lower quartile, Q1) and -19.1°C (upper quartile, Q3), with an average T_h of -22.4°C (Fig. 4.8). Two of 7 type-II inclusions exhibited supercritical behavior upon homogenization, while only one homogenized to vapor. Type-II inclusions that belonged to the same FIA exhibited an average T_h variance of 0.8 ˚C (note: this calculation does not include FIA 11 which had an anomalous range in T_h, or FIA 12 which only had 1 inclusion measurement). Homogenization temperatures of type-I inclusions are organized in FIAs 1-10 and I-IV, and T_h measurements for type-II inclusions are labelled as FIAs 11-13. Notably, FIA IV had anomalously low T_h values (i.e., -112.0 to -111.0°C). In addition, there were 3 FIAs (1, 2, and 11) that showed large variations in T_h which could suggest that these have suffered post-entrapment changes. There could have been post-entrapment leakage or stretching, which would have changed the density of the inclusions and influenced the T_h. Type-III inclusions exhibited clathrate melting (Tm_{clath}) between -4.8ºC and 8ºC and homogenized ($Th_{L\text{-}V>L}$) between 254ºC and 308ºC (Crowell, unpublished).

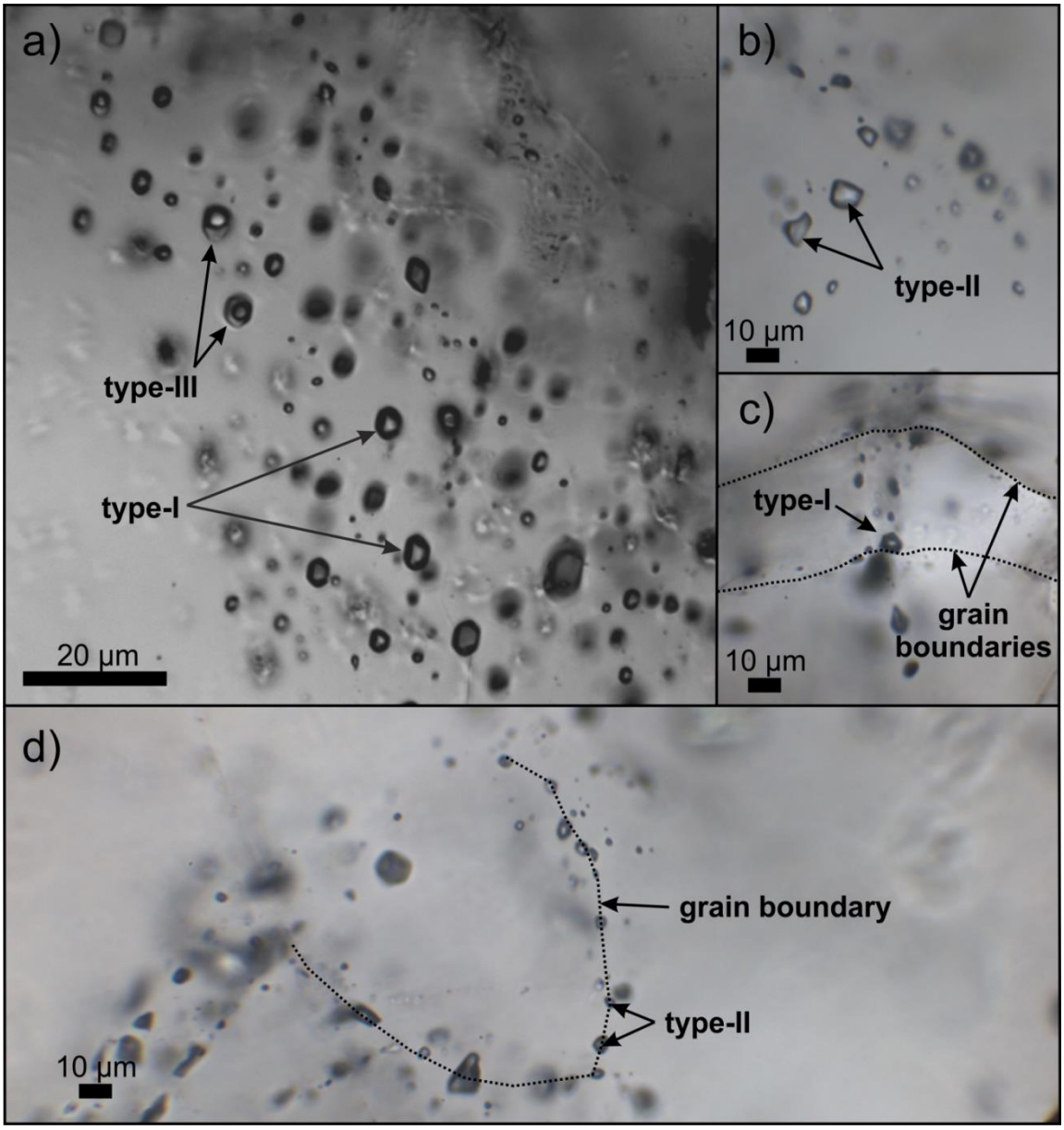

Figure 4.7: Transmitted light photomicrographs of non-aqueous and aqueous fluid inclusions in auriferous quartz veins. (a) Planar array of mixed (heterogeneously trapped) aqueous, type-III inclusions and non-aqueous, type-I fluid inclusions at 100x magnification. (b) Single phase non-aqueous, type-II fluid inclusions at 50x magnification. (c) Linear trail of non-aqueous, type-I fluid inclusions cross cutting healed grain boundaries at 50x magnification. (d) Non-aqueous, type-II inclusions along a healed grain boundary at 50x magnification.

Table 8: Microthemometric data for type-I and –II fluid inclusions

[1]Inclusion	[2]T_m (°C)	T_h (°C)	[3]Origin	[4]Size (μm)	[5]Mode	[6]FIA
type-I						
FIS_LUP6A_1-1	-	-84.3	LS	-	SCB	1
FIS_LUP6A_1-2	-	-89.1	LS	-	SCB	1
FIS_LUP6A_1-3	-	-88.4	LS	-	L	1
FIS_LUP6A_1-4	-	-86.7	LS	-	L	1
FIS_LUP6A_2-1	-	-89.6	LS	-	L	2
FIS_LUP6A_2-2	-	-102	LS	-	L	2
FIS_LUP6A_2-3	-	-89.2	LS	-	L	2
FIS_LUP6A_3-1	-	-89.8	LS	4.5	V	3
FIS_LUP6A_3-2	-	-90	LS	6	V	3
FIS_LUP4C_4-1	-	-82.9	LS	6	SCB	4
FIS_LUP4C_4-2	-	-85.1	LS	4.5	SCB	4
FIS_LUP4D_5-1	-	-89.5	LS	7.5	L	5
FIS_LUP4D_5-2	-	-89.2	LS	7.5	L	5
FIS_LUP4D_5-3	-	-89.1	LS	6	L	5
FIS_LUP4D_5-4	-	-89.1	LS	3	L	5
FIS_LUP4D_6-1	-	-87.7	LS	7	V	6
FIS_LUP4D_6-2	-	-88.4	LS	8	L	6
FIS_LUP4D_6-3	-	-88.3	LS	10	L	6
FIS_LUP4D_6-4	-	-88.4	LS	6	L	6
FIS_LUP4D_6-5	-	-88.5	LS	6	L	6
FIS_LUP4D_7-1	-	-88.9	LS	7.5	L	7
FIS_LUP4D_7-2	-	-89	LS	9	L	7
FIS_LUP4D_7-3	-	-89	LS	6	L	7
FIS_LUP4D_8-1	-	-90.4	LS	7.5	L	8
FIS_LUP4D_8-2	-	-90.3	LS	7.5	L	8
FIS_LUP4D_8-3	-	-90.3	LS	10.5	L	8
FIS_LUP4D_8-4	-	-90.3	LS	7.5	L	8
FIS_LUP4D_8-5	-	-90.4	LS	7.5	L	8
FIS_LUP3E_9-1	-	-88.8	LS	4.5	V	9
FIS_LUP3E_9-2	-	-88.7	LS	4	V	9
FIS_LUP3E_10-1	-	-90.9	LS	3.5	L	10
FIS_LUP3E_10-2	-	-90.9	LS	3	L	10
Crowell_IV-1	-	-112	LS	-	L	IV
Crowell_IV-2	-	-111	LS	-	L	IV
Crowell_I-3	-	-88.8	LS	-	L	I
Crowell_I-4	-	-88.8	LS	-	L	I
Crowell_I-5	-	-89	LS	-	L	I
Crowell_I-6	-	-89.5	LS	-	L	I
Crowell_I-8	-	-89.1	LS	-	L	I
Crowell_I-9	-	-88.8	LS	-	L	I
Crowell_II-14	-	-88.8	LS	-	L	II
Crowell_II-15	-	-88.8	LS	-	L	II
Crowell_II-16	-	-88.8	LS	-	L	II
Crowell_II-17	-	-88.8	LS	-	L	II
Crowell_II-18	-	-88.8	LS	-	L	II
Crowell_II-19	-	-88.9	LS	-	L	II
Crowell_III-20	-	-88.9	LS	-	L	III
Crowell_III-21	-	-88.9	LS	-	L	III
Crowell_III-22	-	-88.9	LS	-	L	III
Crowell_III-23	-	-88.9	LS	-	L	III
Crowell_III-24	-	-88.9	LS	-	L	III
Crowell_III-25	-	-88.9	LS	-	L	III
Crowell_III-26	-	-87.8	LS	-	L	III
Crowell_III-27	-	-88.4	LS	-	L	III
type-II						
FIS_LUP6A_11-1	-63.2541	-19	ES	-	L	11
FIS_LUP6A_11-2	-63.2541	-19.1	ES	-	L	11
FIS_LUP6A_11-3	-63.2541	-21.4	ES	-	SCB	11
FIS_LUP6A_11-4	-64.8429	-36	ES	-	V	11
FIS_LUP6A_12-1	-62.9562	-10.2	ES	5	SCB	12
FIS_LUP6A_13-1	-62.0625	-25.2	ES	-	L	13
FIS_LUP6A_13-2	-	-26	ES	-	L	13

Notes and abbreviations (see previous page): Tm = final melting temperature of the carbonic phase; Th = homogenization temperature of the carbonic phase

[1]Inclusions labeled by thin section (FIS_LUP3, FIS_LUP4, and FIS_LUP6), sample chip (A, C, D, and E), assemblage (1 to 13), and inclusion in respective assemblage. The inclusions by Crowell (unpublished) are labeled by author's name, assemblage, and inclusion number

[2]Only type-II inclusion carbonic phase melting temperatures could be measured. Type-I inclusion carbonic phase melting temperatures could not be observed because freezing of the carbonic phase could not be achieved with the degree of undercooling possible with the available instrumentation and liquid nitrogen as a coolant

[3]Fluid inclusion origin is based on petrographic observations

[4]Size indicates the diameter of a discrete inclusion; assemblages 1, 2, 11, 13, and Crowell (unpublished) were not measured

[5]Mode of homogenization: L (homogenize to liquid = vapor bubble collapsed); V (homogenize to vapor = vapor bubble expanded); SCB (by supercritical behavior = vapor bubble gradually disappeared)

[6]For all samples, groups of inclusions were designated as assemblages if they were in the same trail or cluster LS = late secondary and ES = early secondary

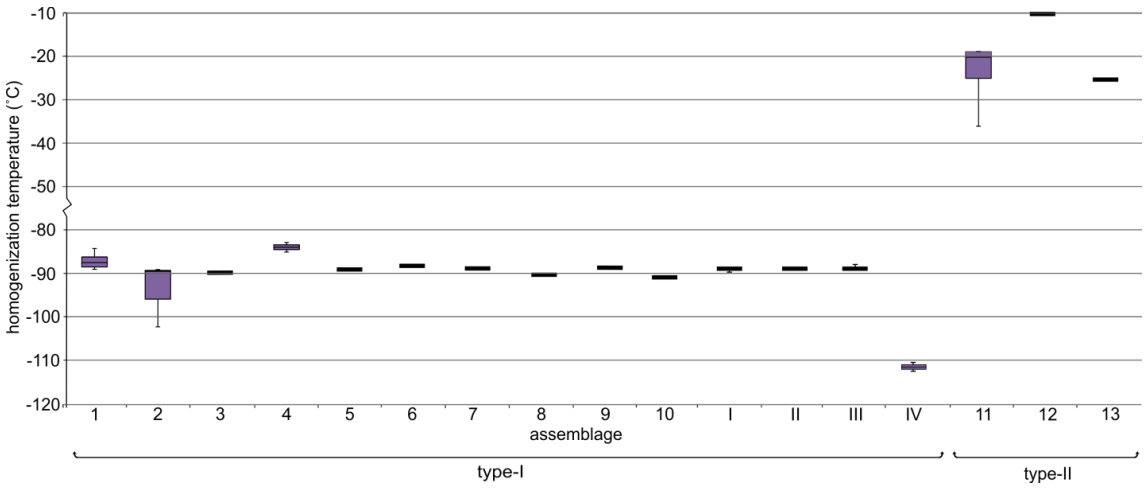

Figure 4.8: Homogenization temperatures of a carbonic phase in quartz fluid inclusions. Upon homogenization, the two-phase (liquid and vapor) carbonic fluid transitioned into a single-phase carbonic fluid. The upper limit of each box represents the upper quartile (Q3), or maximum, temperature of the FIA; whereas, the lower limit of each box represents the lower quartile (Q1), or minimum, temperature of the FIA. The whiskers represent outlier temperatures and were not factored into the lower and upper temperature limits for each FIA. Homogenization temperatures of type-I inclusions are organized in FIAs 1-10 and I-IV, while T_h measurements for type-II inclusions are labelled as FIAs 11-13.

4.4 – Laser Raman microscopy

Raman spectra were examined from 33 individual quartz fluid inclusions. On the basis of compounds present in the inclusions and their relative abundances, quantified by Raman analysis, 22 fluid inclusions were labelled as type-I, whereas the remaining 11 fluid inclusions were labelled as type-II (Table 9). Both types-I and -II correspond to the inclusions of the same label described in Section 4.3. Raman measurements from Crowell's unpublished directed study (n=14) were included in this study for comparison purposes and to strengthen the sample size (n_{total} = 47). Type-I fluid inclusions, which crosscut healed grain boundaries (Fig. 4.7), contain CH_4, N_2, and H_2S, with average mole percentages of 89%, 11%, and ~1%, respectively. The average CH_4:N_2 ratio of type-I inclusions was 8.8, with a range from 7.1 (Q1) to 10.6 (Q3). Methane concentrations ranged from 87.1 (Q1) to 90.7 (Q3) mol% and N_2 concentrations ranged from 8.6 (Q1) to 12.2 (Q3) mol% (Table 9); their averages were 88.6 and 10.8 mol%, respectively. Type-II fluid inclusions, which follow healed grain boundaries (Fig. 4.7), contain CO_2, CH_4, N_2, and H_2S, with average mole percentages of 50.4, 22.7, 26.7, and 0.2, respectively. The average CO_2:CH_4 ratio of type-II inclusions is 2.41. Type-III fluid inclusions have a saline aqueous fluid with a vapor bubble containing CH_4 but not CO_2, H_2S, or N_2 like the non-aqueous inclusions (Crowell, unpublished). These vapor bubbles represent immiscibly entrapped CH_4. Raman peak areas and quantified mol % determined using semi-quantitative methods for various contained volatile species (CO_2, CH_4, N_2, and H_2S) are listed in Table 9.

Examples of typical spectra, with characteristic Raman peaks labelled, are shown in Figs. 4.9 and 4.10. The Raman shifts for N_2 peaks depicted in Figs.4.9 and 4.10 have a

range of ~2326 to ~2327cm^{-1}, while those for H_2S are both roughly 2578cm^{-1}. The Raman shift for CH_4 varies between the non-aqueous and vapor bubbles of type-III inclusions, with the non-aqueous having a shift of ~2912cm^{-1} and type-III having a shift of ~2917cm^{-1}. Type-II inclusions have two Raman shift peaks for CO_2 (i.e., fermi diad) at ~1282cm^{-1} and ~1385cm^{-1}. Type-III inclusions have broad H_2O peaks that range from ~3439 to ~3442cm^{-1} and some analyzed vapor bubbles contained an H2 peak at ~4155cm^{-1} (Crowell, unpublished). The relative abundances of the volatiles of all type-I and type-II inclusions are depicted in two tri-plots [i.e., CH_4-N_2-CO_2, and (CO_2+CH_4)-N_2-(H_2Sx100)] (Fig. 4.11). Concentrations are compared to other volatiles contained in quartz of gold-bearing deposits with varying metamorphic grade, including those of eclogite-, granulite-, and greenschist-amphibolite-facies. Volatiles contained in auriferous slates are included as well. The volatile species distribution and overall miscibility of all volatile species in type-I inclusions at room T is demonstrated in two-dimensional Raman compositional maps of a single inclusion (Fig. 4.12). The relative peak intensities of three fluid species (i.e., CH_4, N_2, and H_2S) and a ratio map of CH_4:N_2 are shown in individual maps, but their intensities have been modified in order to improve the presentation of their spatial distribution. The modification involved artificially increasing the intensities in order to best display the compounds distribution in the inclusion (i.e. all intensities are not normalized). Therefore, these images should be used to display the homogeneity of these species only, not to infer relative abundances. The maps show that the volatile species share the same space within the inclusion, and are therefore non-aqueous miscible or homogeneous single-phase inclusions.

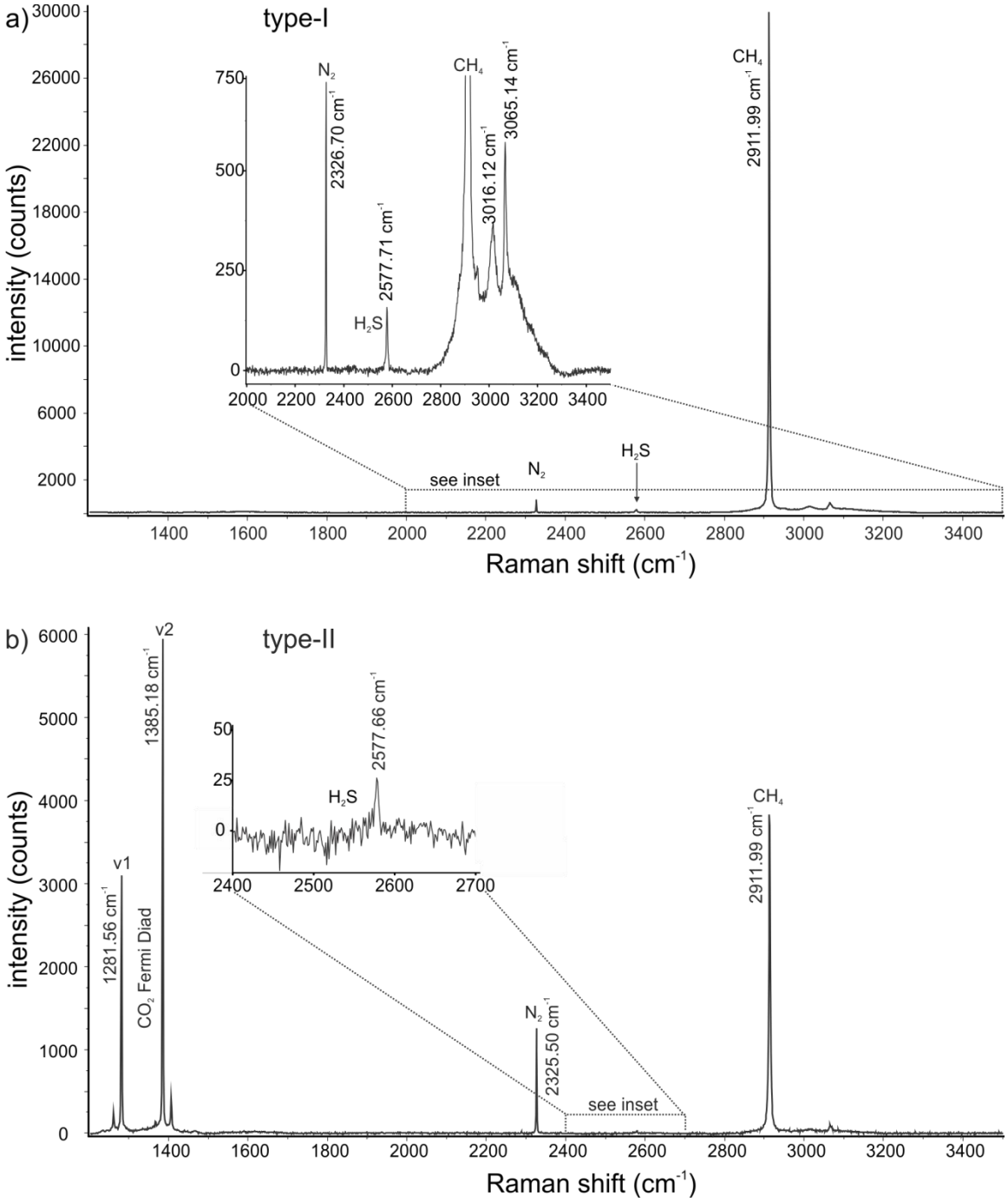

Figure 4.9: Laser Raman microscopy spectra of type-I and type-II fluid inclusions on an intensity (counts) vs. Raman shift (cm^{-1}) plot. Insets show lower intensity volatile species. (a) Spectrum of a type-I inclusion with N_2 at 2326.70 cm^{-1}, H_2S at 2577.71 cm^{-1}, and CH_4 at 2911.99 cm^{-1}. (b) Spectrum of a type-II inclusion with CO_2 at 1281.56 cm^{-1} and 1385.18 cm^{-1}, N_2 at 2325.50 cm^{-1}, H_2S at 2577.66 cm^{-1}, and CH_4 at 2911.99 cm^{-1}.

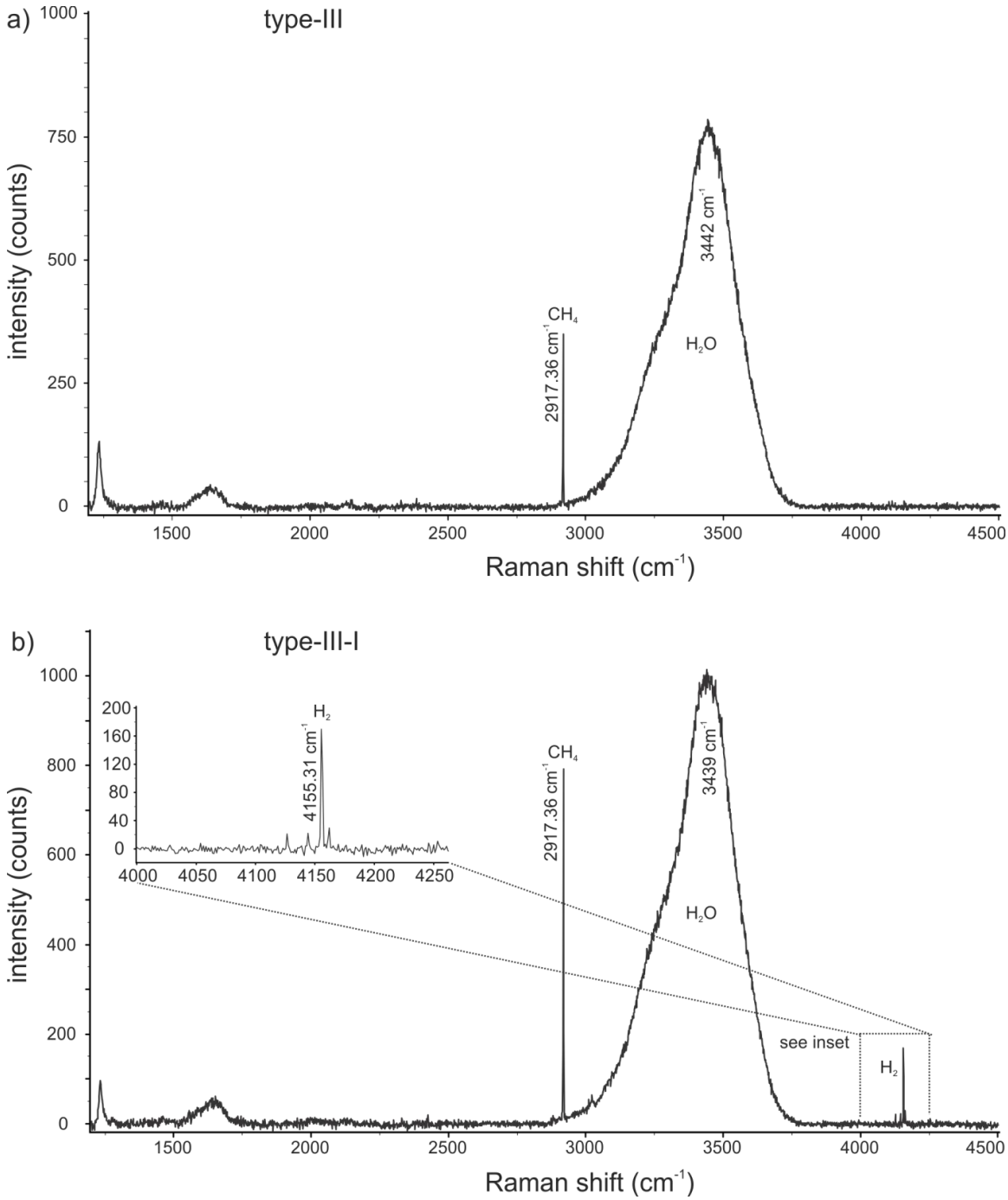

Figure 4.10: Laser Raman microscopy spectra of type-III and type-III-I fluid inclusions on an intensity (counts) vs. Raman shift (cm^{-1}) plot. (a) Spectrum of a type-III inclusion with CH_4 at 2917.36 cm^{-1} and H_2O at 3442 cm^{-1}. (b) Spectrum of a mixed type-III-I inclusion with CH_4 at 2917.36 cm^{-1}, H_2O at 3439 cm^{-1}, and H_2 at 4155.31 cm^{-1}. These inclusions are rare and they contain mixed proportions of type-I and type-III fluids and are therefore evidence of immiscibility. Inset highlights the presence of hydrogen gas.

Table 9: Laser Raman microscopy data for non-aqueous quartz-hosted fluid inclusions

			peak areas							mole fractions			
inclusion	**mineral host**	**f.d. spacing (cm)**	**CO2 v1**	**CO2 v2**	**CO2 total**	**CH4**	**N2**	**H2S**	**CO2:CH4**	**XCO2**	**XCH4**	**XN2**	**XH2S**
type-I (CH4-N2-H2S)													
Lupin_fi1	quartz	n/a	-	-	-	84800	1050	-	-	-	0.907	0.093	-
Lupin_fi2	quartz	n/a	-	-	-	79400	971	734	-	-	0.898	0.091	0.011
Lupin_fi3	quartz	n/a	-	-	-	152000	2520	1200	-	-	0.871	0.120	0.009
Lupin_fi4	quartz	n/a	-	-	-	69200	826	616	-	-	0.900	0.089	0.011
Lupin_fi5	quartz	n/a	-	-	-	53700	781	467	-	-	0.883	0.107	0.010
Lupin_fi6	quartz	n/a	-	-	-	42600	622	373	-	-	0.883	0.107	0.010
chipA_area2_inc5-2	quartz	n/a	-	-	-	13300	270	85	-	-	0.849	0.144	0.007
chipA_area2_inc5-3	quartz	n/a	-	-	-	137000	2250	1150	-	-	0.872	0.119	0.010
chipA_area6_inc12	quartz	n/a	-	-	-	13100	142	76	-	-	0.911	0.082	0.007
chipA_area6_inc13	quartz	n/a	-	-	-	22400	249	163	-	-	0.907	0.084	0.009
chipA_area6_inc14-1	quartz	n/a	-	-	-	12800	157	95	-	-	0.899	0.092	0.009
chipA_area6_inc14-2	quartz	n/a	-	-	-	3770	123	-	-	-	0.787	0.213	-
chipA_area7_inc15	quartz	n/a	-	-	-	12800	131	91.1	-	-	0.914	0.078	0.009
chipA_area7_inc16-1	quartz	n/a	-	-	-	113000	1220	925	-	-	0.909	0.081	0.010
chipA_area7_inc16-2	quartz	n/a	-	-	-	34300	392	269	-	-	0.905	0.086	0.009
chipA_area9_inc1	quartz	n/a	-	-	-	10800	86	-	-	-	0.938	0.062	-
chipA_area9_inc2	quartz	n/a	-	-	-	5380	80	20	-	-	0.885	0.110	0.004
chipD_area1_inc1	quartz	n/a	-	-	-	7470	125	0	-	-	0.878	0.122	-
chipD_area1_inc2	quartz	n/a	-	-	-	20800	282	157	-	-	0.891	0.100	0.009
chipD_area1_inc3	quartz	n/a	-	-	-	26400	298	208	-	-	0.906	0.085	0.009
chipD_area1_inc4	quartz	n/a	-	-	-	54500	873	450	-	-	0.874	0.116	0.009
chipD_area1_inc6	quartz	n/a	-	-	-	30000	328	214	-	-	0.909	0.083	0.008
d	quartz	n/a	-	-	-	5940	104	-	-	-	0.873	0.127	-
d1	quartz	n/a	-	-	-	4810	89	-	-	-	0.866	0.134	-
d2	quartz	n/a	-	-	-	1490	27	-	-	-	0.867	0.133	-
d3	quartz	n/a	-	-	-	4440	50	-	-	-	0.914	0.086	-
d4	quartz	n/a	-	-	-	70900	1200	683	-	-	0.867	0.122	0.011
d5	quartz	n/a	-	-	-	22600	412	180	-	-	0.861	0.130	0.009
d13	quartz	n/a	-	-	-	132000	2250	1130	-	-	0.867	0.123	0.010
type-II (CO2-CH4-N2-H2S)													
chipA_area1_inc2-3	quartz	105	9020	16000	25000	23100	3640	217	2.700	0.538	0.199	0.261	0.002
chipA_area1_inc3-3	quartz	103	10700	18700	29400	24800	4010	195	2.960	0.557	0.188	0.253	0.002
chipA_area2_inc6	quartz	106	5180	8710	13900	19300	2410	220	1.800	0.467	0.260	0.270	0.004
chipA_area2_inc7	quartz	105	11900	20600	32500	43500	5740	245	1.870	0.470	0.252	0.276	0.002
chipA_area3_inc8	quartz	104	5080	9620	14700	10300	1640	-	3.580	0.605	0.169	0.225	-
chipA_area4_inc9	quartz	106	4450	9660	14100	13500	1600	-	2.610	0.568	0.218	0.214	-
chipA_area4_inc10	quartz	106	907	1580	2490	2210	314	-	2.800	0.563	0.201	0.237	-
chipA_area5_inc11	quartz	104	1640	2500	4140	2630	880	-	3.930	0.510	0.130	0.360	-
chipA_area10_inc1	quartz	106	945	1750	2690	5000	692	63.8	1.340	0.383	0.285	0.328	0.005
chipA_area10_inc2	quartz	106	1980	3820	5800	8890	851	79.1	1.630	0.474	0.291	0.232	0.003
chipA_area10_inc3	quartz	105	943	2360	3300	11000	1030	38.3	0.751	0.296	0.394	0.307	0.002
d8	quartz	104	8870	15100	24000	22200	3640	196	2.700	0.532	0.197	0.269	0.002
d9	quartz	104	10200	17500	27700	23400	4040	136	2.950	0.547	0.185	0.266	0.001
d10	quartz	104	18600	31100	49700	53500	7770	393	2.320	0.511	0.220	0.266	0.002
d14	quartz	104	4880	8120	13000	19200	2400	263	1.690	0.451	0.267	0.277	0.005
d15	quartz	104	11500	19300	30800	42300	5700	267	1.820	0.460	0.254	0.284	0.002
d16	quartz	104	5330	8120	13400	10200	1680	-	3.290	0.581	0.177	0.242	-
d18	quartz	104	946	1450	2390	2230	315	-	2.680	0.552	0.206	0.242	-

Notes:
[1]f.d. = fermi diad
[2]H_2S liquid (Raman shift = 2577.71 cm^{-1})
Inclusions labelled with "d" are from Crowell's 2014 directed study (unpublished).
Total number of inclusions analyzed was n = 47.

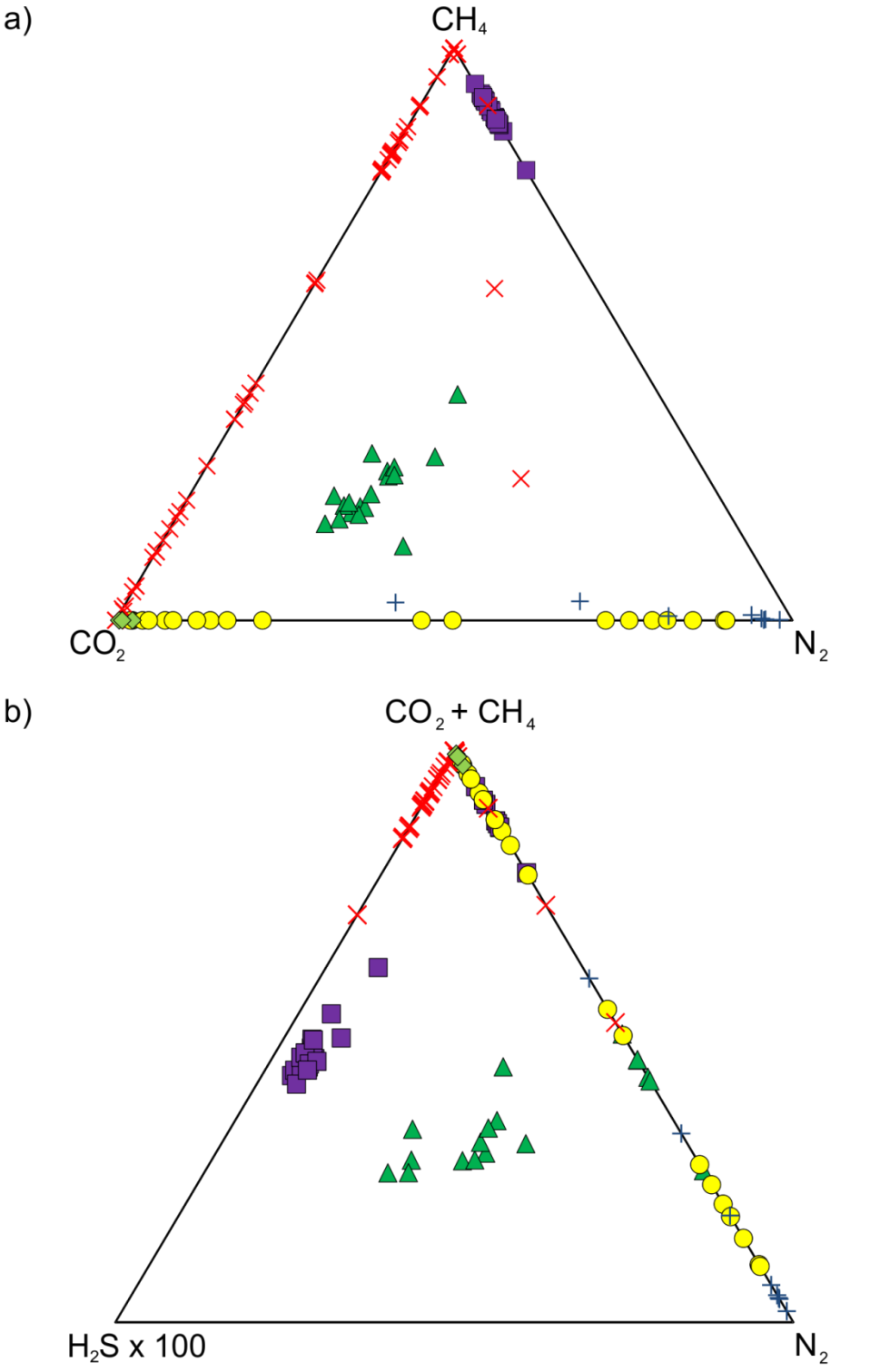
a)
CH4
CO2
N2
b)
CO2 + CH4
H2S x 100
N2
Legend
= type-I
= type-II
= 1eclogites
= 2granulites
= 3greenschist-amphibolite
= 4slates

Figure 4.11: (see previous page) Molar concentrations of volatile species in type-I and type-II fluid inclusions as determined by laser Raman microscopy. Concentrations are compared to other volatiles contained in quartz of gold-bearing deposits with varying metamorphic grade, including those of eclogite-, granulite-, and greenschist-amphibolite-facies. (a) Relative molar concentrations of CH_4, N_2, and CO_2 in type-I (purple squares) and type-II (green triangles) fluid inclusions, compared to fluids of other auriferous deposits. (b) Relative molar concentrations of CO_2+CH_4, N_2, and H_2Sx100 in type-I and type-II fluid inclusions, compared to fluids of other auriferous deposits.
[1]Fluid inclusions in eclogite-hosted quartz from difference localities in the Western Gneiss Region of the Norwegian Caledonides and pegmatitic quartz-omphacite and quartz+phengite/paragonite veins of the Grenvillian eclogite-facies complex on Holsnøy Island, Bergen Arcs, W. Norway (Andersen et al., 1989; Andersen et al., 1990)
[2]Fluid inclusions in banded-granulite-hosted quartz of the Grenvillian granulite-facies complex on Holsnøy Island, Bergen Arcs, W. Norway (Andersen et al., 1990)
[3]Volatiles from other orogenic gold samples, including: quartz from the McPhee's gold deposit in the granite-greenstone terrane of the Pilbara Craton (Baker & Seccombe, 2004); quartz from the amphibolite-facies metavolcanics of the Missouri and Sand King deposits in the Siberia district of the Eastern Goldfields province, Western Australia (Mernagh & Witt, 1994); saccharoidal quartz associated with an amphibolitic grade gold lode deposit in the Pontal mine, northeastern part of the Tocantins State, Brazil (Guilhaumou et al., 1990);
[4]Fluid inclusions in slate-hosted vein quartz of the Llanbedr Formation, North Wales (Bottrell et al., 1988)

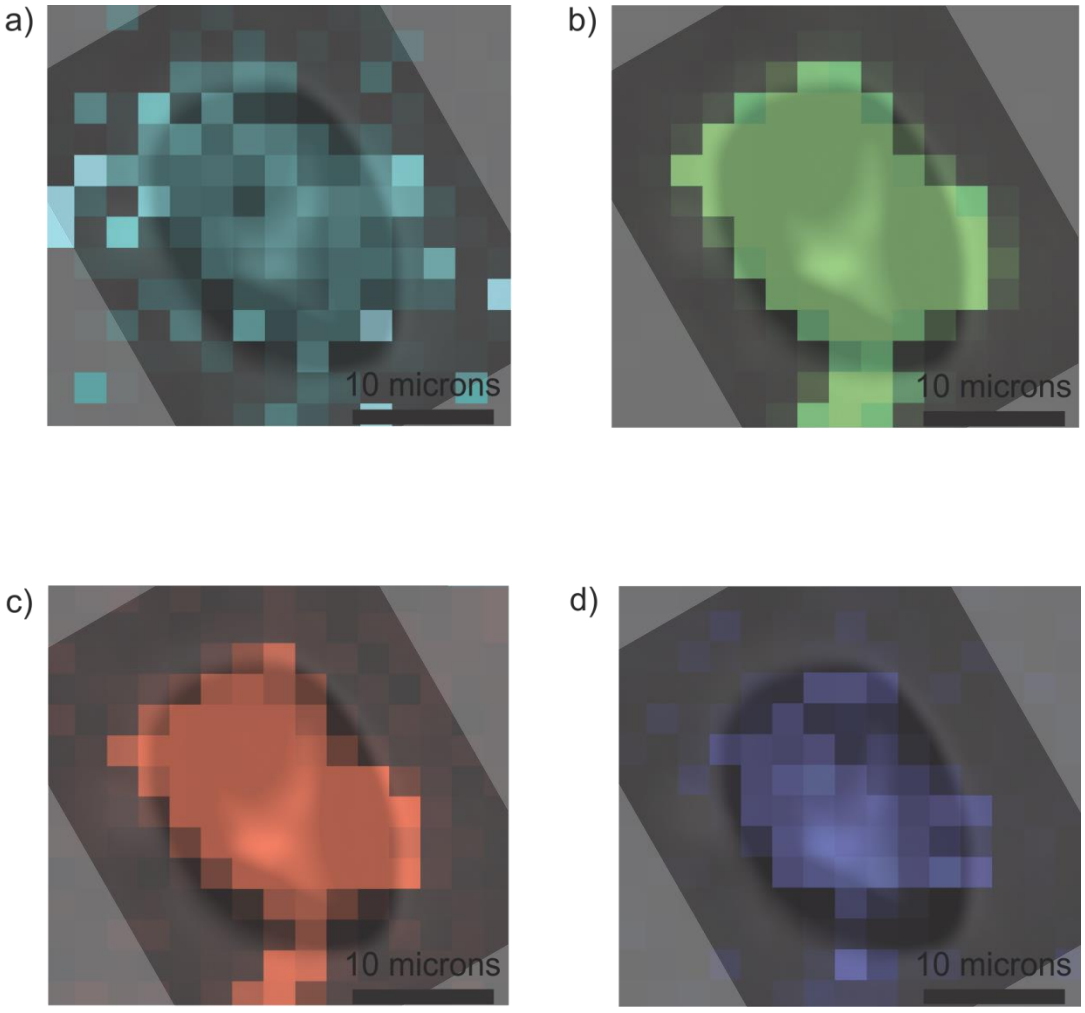

Figure 4.12: Two-dimensional composition maps, as determined with laser Raman microscopy, of a single type-I fluid inclusion showing the distribution of volatile species. Combined, the maps show the homogeneous nature of the non-aqueous type-I inclusions. (a) CH_4:H_2S ratio intensity map using peak areas; (b) CH_4 intensity map using peak area; (c) N_2 intensity map using peak area; (d) H_2S, or bi-sulfide, intensity map using peak area.

4.5 – In-line rock-crushing gas chromatography

A bulk crush of a 0.6g vein quartz sample from a mineralized selvage revealed that type-I, -II, and –III fluid inclusion volatiles are very rich in CH_4 and propane (C_3H_8) with a light enrichment in other higher order hydrocarbons (Fig. 4.13). There are single-chain alkanes [i.e., n-butane (C_4H_{10}), n-pentane (C_5H_{12}), and n-hexane (C_6H_{14})], and branched-chain alkanes [i.e., 2,2-dimethylpropane (C_5H_{12}), and 2-methylbutane (C_5H_{12})]. Also, there are single-chain alkenes [i.e., propene (C_3H_6), 1-butene (C_4H_{10}), 1-pentene (C_5H_{10}), c-2-pentene (C_5H_{10}), and 1-hexene (C_6H_{12})] and a branched-chain alkene [isobutene (C_4H_{10})]. Finally, there is toluene (C_7H_8), which is an aromatic hydrocarbon. A crush of a 0.5g sample of clean Brazilian quartz provided a comparative chromatogram that shows volatile species contained in a relatively pure silica sample with minimal fluid inclusions. The Brazilian quartz sample showed small peaks of methane, benzene, and an unknown species at 15.8 min.

Two additional aliquots of quartz from the same vein selvage were crushed using a separate GC method employing TCD and FID detectors in series to detect and quantify CO_2, H_2O and light hydrocarbons (Fig. 4.14). This was done to quantify proportions, in mol%, of H_2O, CO_2, CH_4 and C_{2+}. The first crush gave proportions of 45.9%, 24.6%, 29.2% and 0.3% for H_2O, CO_2, CH_4 and C_{2+}, respectively. The second crush gave proportions of 27.1%, 26.7%, 45.7% and 0.4% for H_2O, CO_2, CH_4 and C_{2+}, respectively.

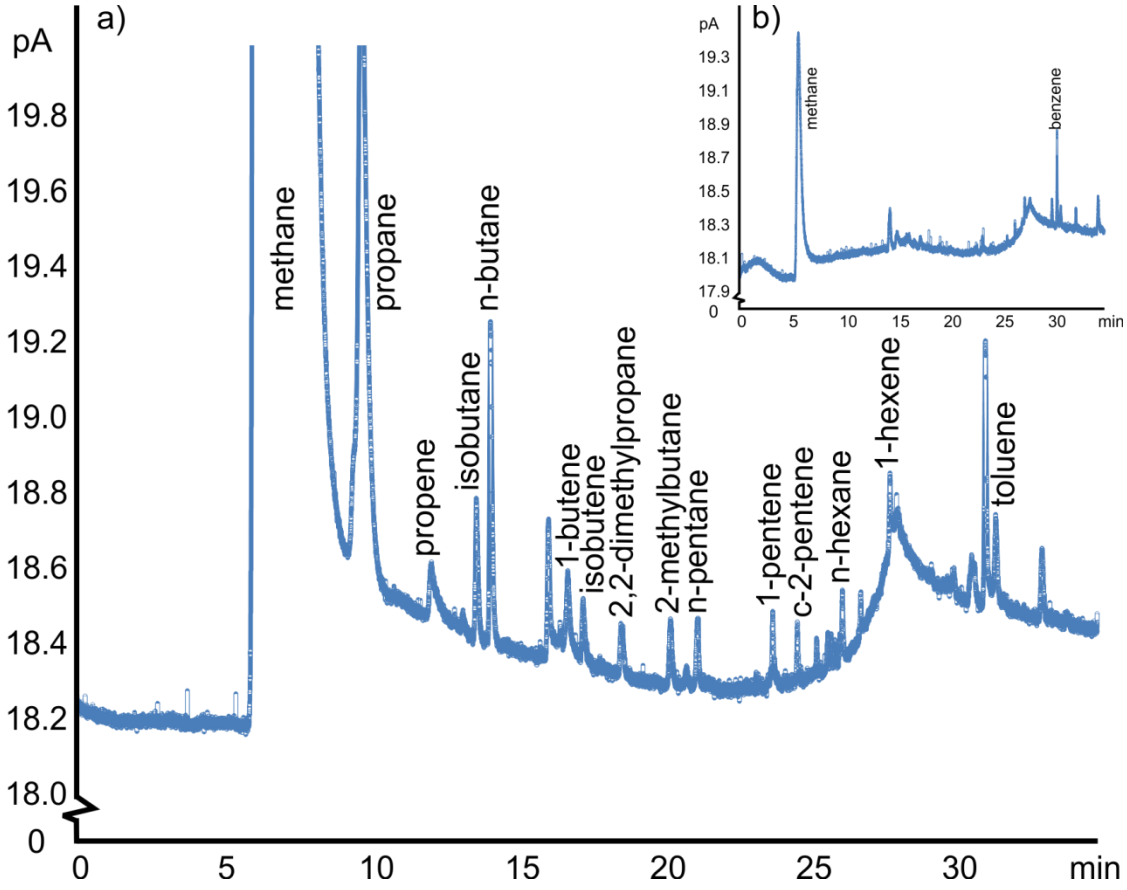

Figure 4.13: Gas chromatogram of a vein quartz sample using a FID. (a) Bulk analysis gas chromatogram of hydrocarbon concentrations released from a 0.6g quartz sample from a late quartz vein in a zone of mineralization. Relatively high concentrations of CH_4 and C_3H_8 are present as well as a variety of other higher order light hydrocarbons. However, the CH_4 peak is likely obscuring a CO_2 peak. (b) Chromatogram of the gas content in a crushed sample (0.5g) of Brazilian quartz blank.

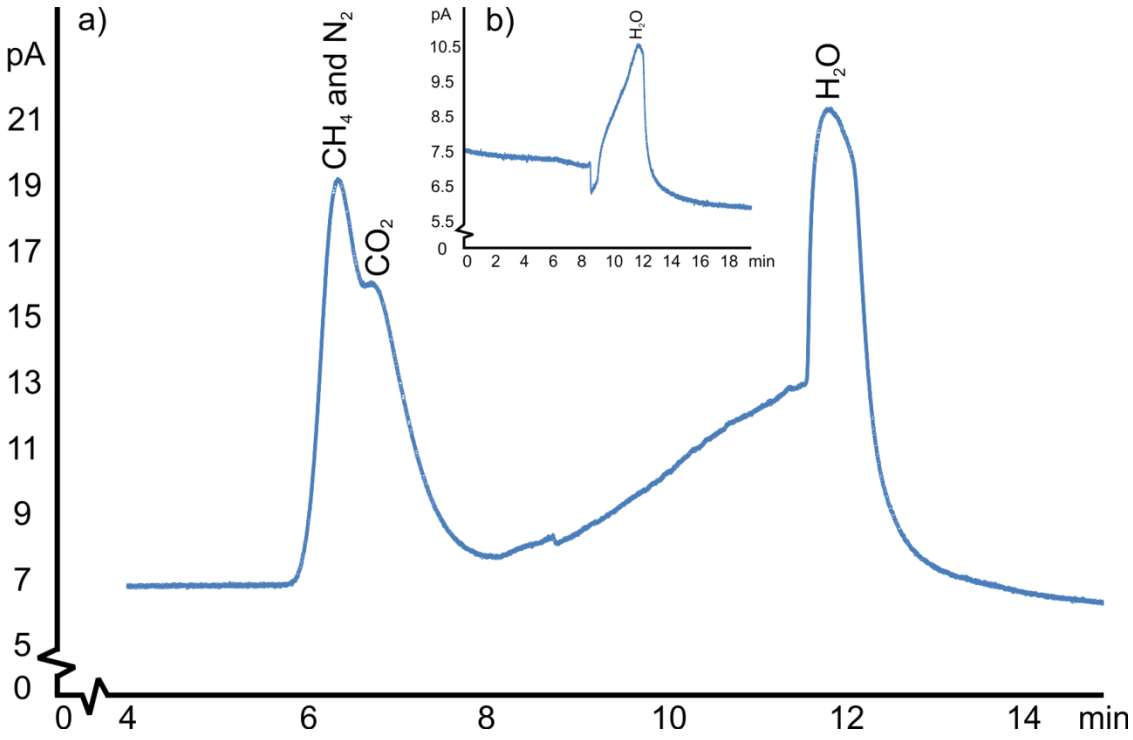

Figure 4.14: Gas chromatogram of a vein quartz sample using a FID and a TCD in series. (a) Bulk analysis gas chromatogram of a quartz sample from a late vein in a zone of mineralization. A shoulder peak of CO_2 is depicted, along with CH_4 + N_2, and H_2O peaks. (b) Blank crush of clean quartz with trace H_2O which may have adsorbed to the quartz.

4.6 – Arsenopyrite thermometry and trace element chemistry

To obtain an independent estimate of T, for application in the evaluation of the P-T characteristics of fluid inclusion entrapment, the atomic percent of As in an arsenopyrite grain of the assemblage asenopyrite-pyrrhotite-(pyrite) was calculated from SEM-EDS analysis and indicates that the final temperature of equilibration of arsenopyrite from loellingite was less than 300˚C (Fig. 4.15) (Kretschmar & Scott, 1976; Sharp et al., 1985). The T-X values of arsenopyrite equilibration were 300˚C and 28 – 30 %As, which are much lower than those of other arsenopyrite grains found in Contwoyto Lake (i.e., 550 - 600˚C, and 34.4-35.5 %As) (Kretschmar, 1973; and Bostock, 1968). However, arsenopyrite grains studied by Kretschmar (1973) and Bostock (1968) contained remnant loellingite, whereas the grains in this study did not, so higher temperatures and As concentrations associated with final equilibration would be expected. Comparison of these loellingite-bearing arsenopyrite grains to the arsenopyrite grains of this study showed that for an arsenopyrite grain to fully form from loellingite, T must drop drastically. Textural evidence shows that arsenopyrite is in equilibrium with pyrrhotite. Pyrite is present as well, but in far lesser abundance than pyrrhotite; therefore, the system is buffered with respect to S. Arsenopyrite would have formed from loellingite by a significant decrease in temperature and by the following reaction:

$$FeAs_2 + 4FeS + S_2 \rightarrow 2FeAsS + 2FeS + FeS_2 \quad (1)$$

Selected quantified maps of major and trace elements were generated from their appropriate time series data (Fig. 4.16, Fig. 4.17, and Fig. 4.18). For plotting of trace and major element variation diagrams, the time series data was filtered of any laser ablation spots that yielded As < 32%, representing ideal arsenopyrite. In some cases, concentrations higher than 32% (up to 75%) were reported, representing arsenopyrite spot analyses that are anomalously high due to the As "memory effect" persisting from one laser shot analysis to the next. Long wash out times did not reduce this but since As was not used as an internal standard, this had a negligible impact on the quantified trace element data. High As values did not represent shots in loellingite because the quantified S map of, for example, grain LUP7 (small) (Appendix B, Fig. III) did not show any S-free areas (i.e, no remnant loellingite). Laser spots yielding concentrations of As below 32% were deemed to represent mixed arsenopyrite-pyrrhotite-silicate signals and were excluded. The entire map suites for the SIBX, LUP7 (big), and LUP7 (small) arsenopyrite grains can be seen in Appendix B. These maps include both linear and logarithmic scales of element concentration.

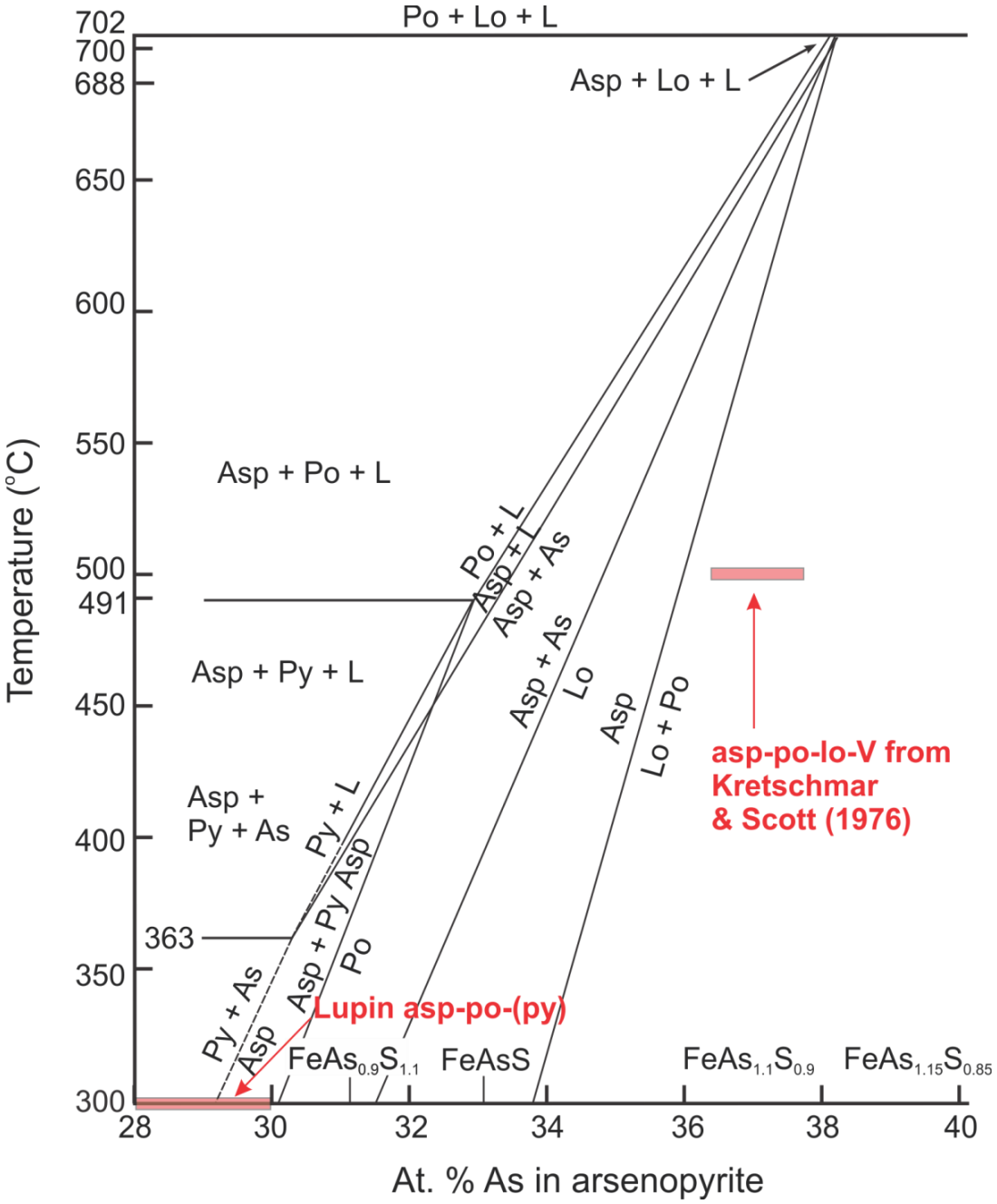

Figure 4.15: SEM-EDS analysis of arsenic in arsenopyrite shown on a T-X diagram with arsenopyrite-buffered curves. SEM-EDS analysis of atomic % As in arsenopyrite in the arsenopyrite-pyrrhotite-(pyrite) assemblage indicates a low temperature of final equilibration (<=300˚C) associated with the crystallization of arsenopyrite from loellingite. This reaction requires either a significant decrease in temperature or an increase in S_2 fugacity [see reaction (1)], or both. Kretschmar and Scott (1976) presented atomic % As ranges and associated temperatures for natural samples of arsenopyrite + loellingite + pyrrhotite + vapor from the Contwoyto Lake area, N.W.T. A red polygon represents the ranges of % As at 500 ˚C and is included for comparison purposes. Image modified from Kretschmar and Scott, 1976.

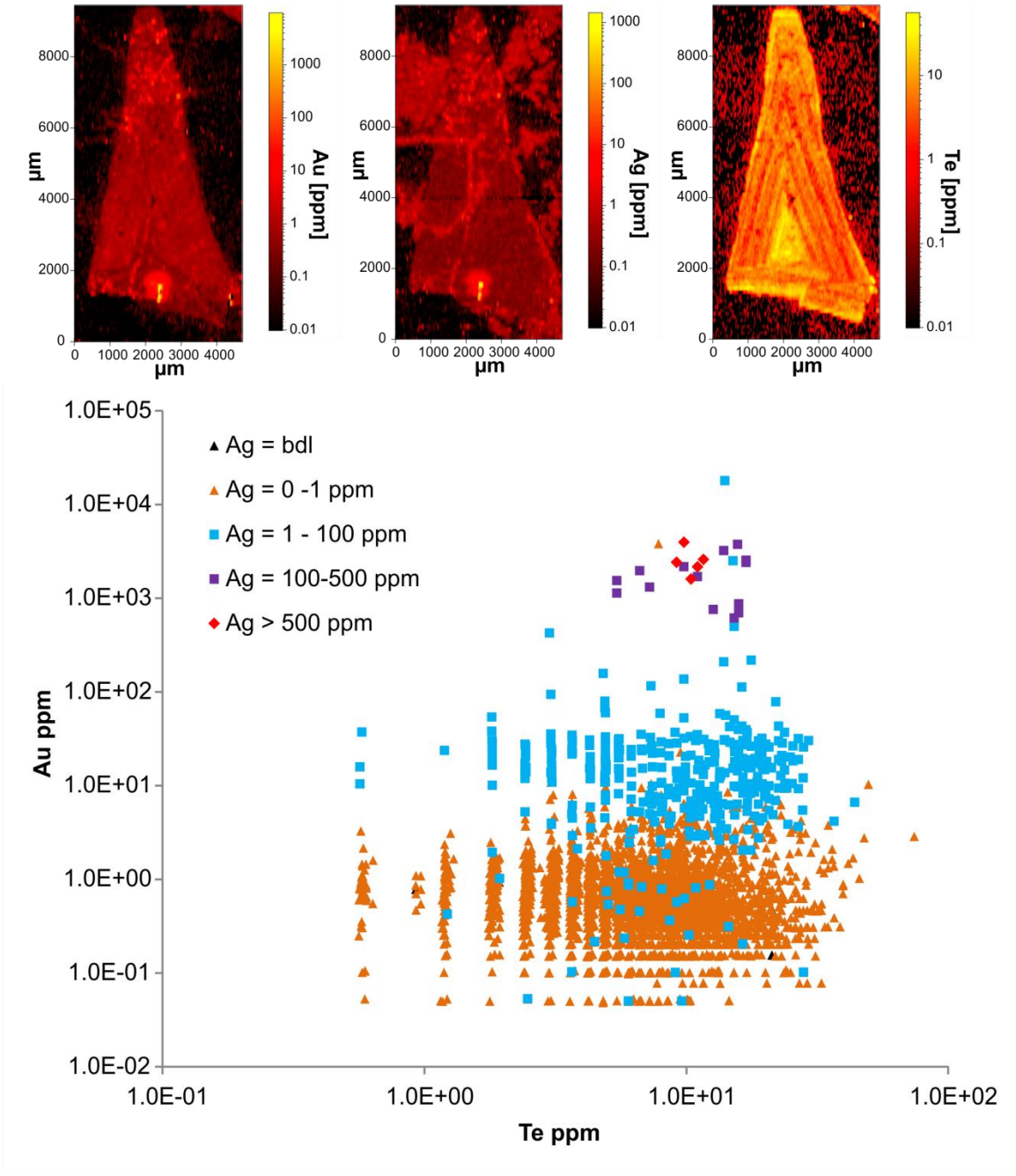

Figure 4.16: Graphical correlation of Ag-Au vs. Te with LA-ICP-MS maps. LA-ICP-MS maps of the LUP7 (big) arsenopyrite grain with logarithmic scales showing correlation of Au with Ag (i.e., electrum). The Te map shows growth rings which represent crystallization events with variable chemical input. The data set contains 3682 laser spots and is represented in a graphical correlation of Au vs. Te with Ag brackets.

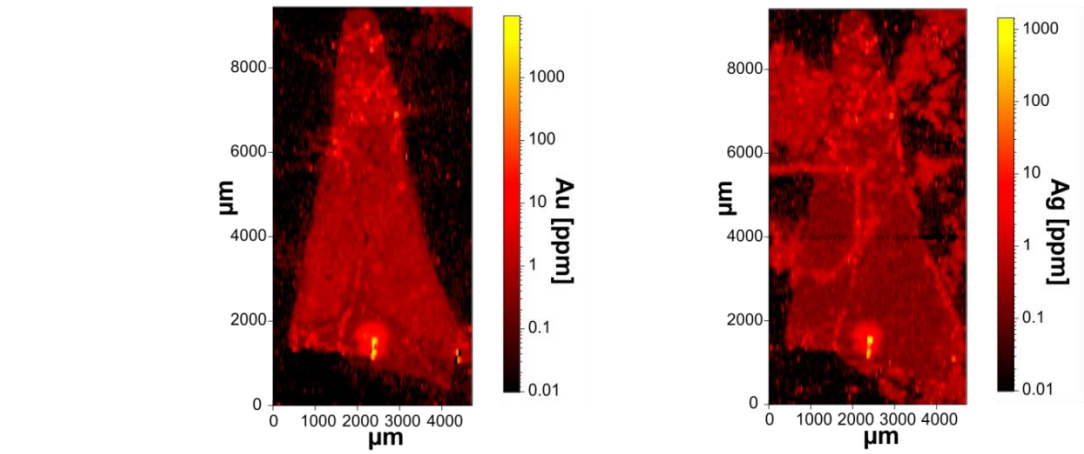
8000
6000
4000
2000
0
µm
0 1000 2000 3000 4000
µm
1000
100
10
1
0.1
0.01
Au [ppm]
Ag [ppm]

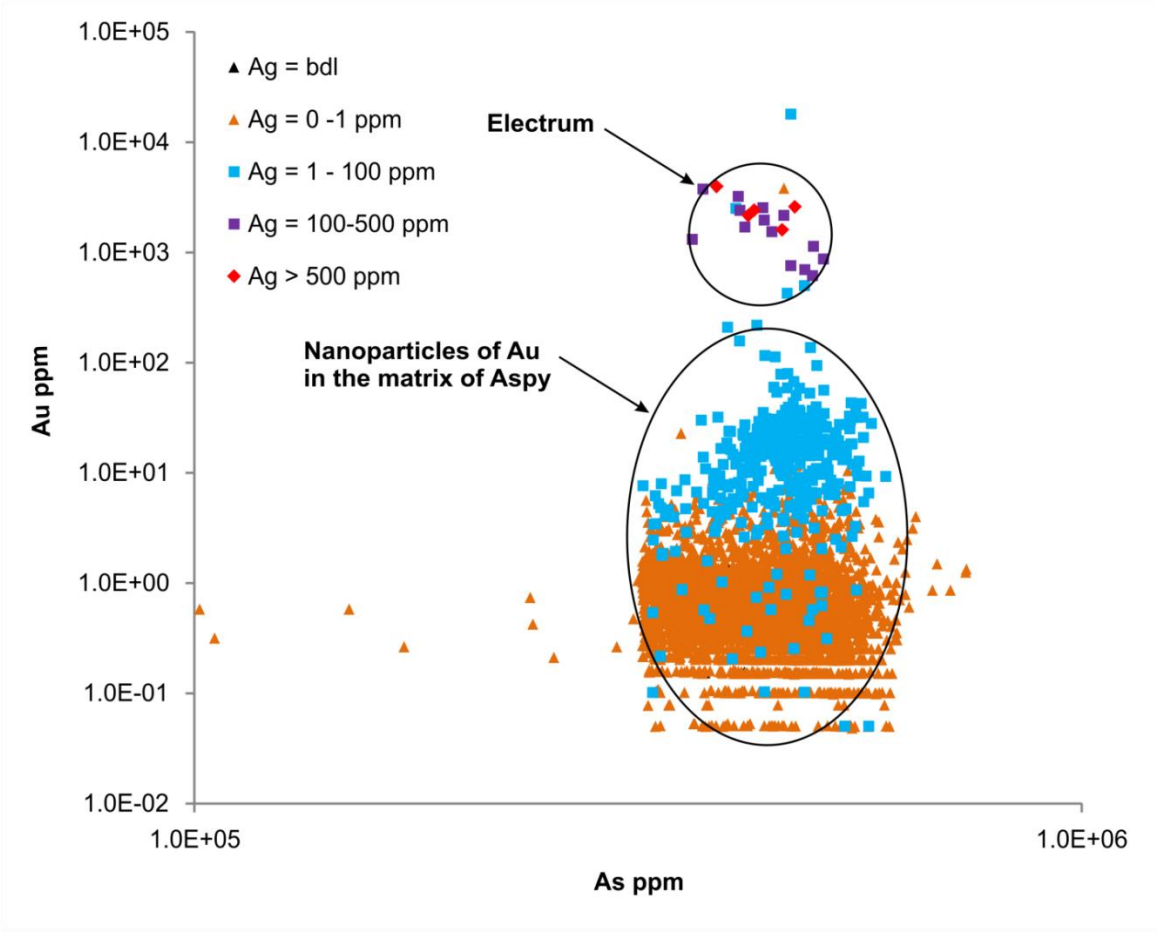
Ag = bdl
Ag = 0 -1 ppm
Ag = 1 - 100 ppm
Ag = 100-500 ppm
Ag > 500 ppm
Electrum
Nanoparticles of Au
in the matrix of Aspy
1.0E+05
1.0E+04
1.0E+03
1.0E+02
1.0E+01
1.0E+00
1.0E-01
1.0E-02
Au ppm
1.0E+05
1.0E+06
As ppm

Figure 4.17: (see previous page) Graphical correlation of Ag-Au vs. As with LA-ICP-MS maps. LA-ICP-MS maps of the LUP7 (big) arsenopyrite grain with logarithmic scales showing correlation of Au with Ag (i.e., electrum). Quantified As map is not included because it is not reliable due to the fact that As has a resident time in the system (i.e., memory) and thus affects any As coming from the NIST glass and the As background. The data set contains 3682 laser spots and is represented in a graphical correlation of Au vs. As with Ag brackets. The large cluster of light blue and orange data points depicts Au that has been incorporated into the matrix of the arsenopyrite grain as nanoparticles, which can be roughly a micron or less (Palenik et al., 2004).

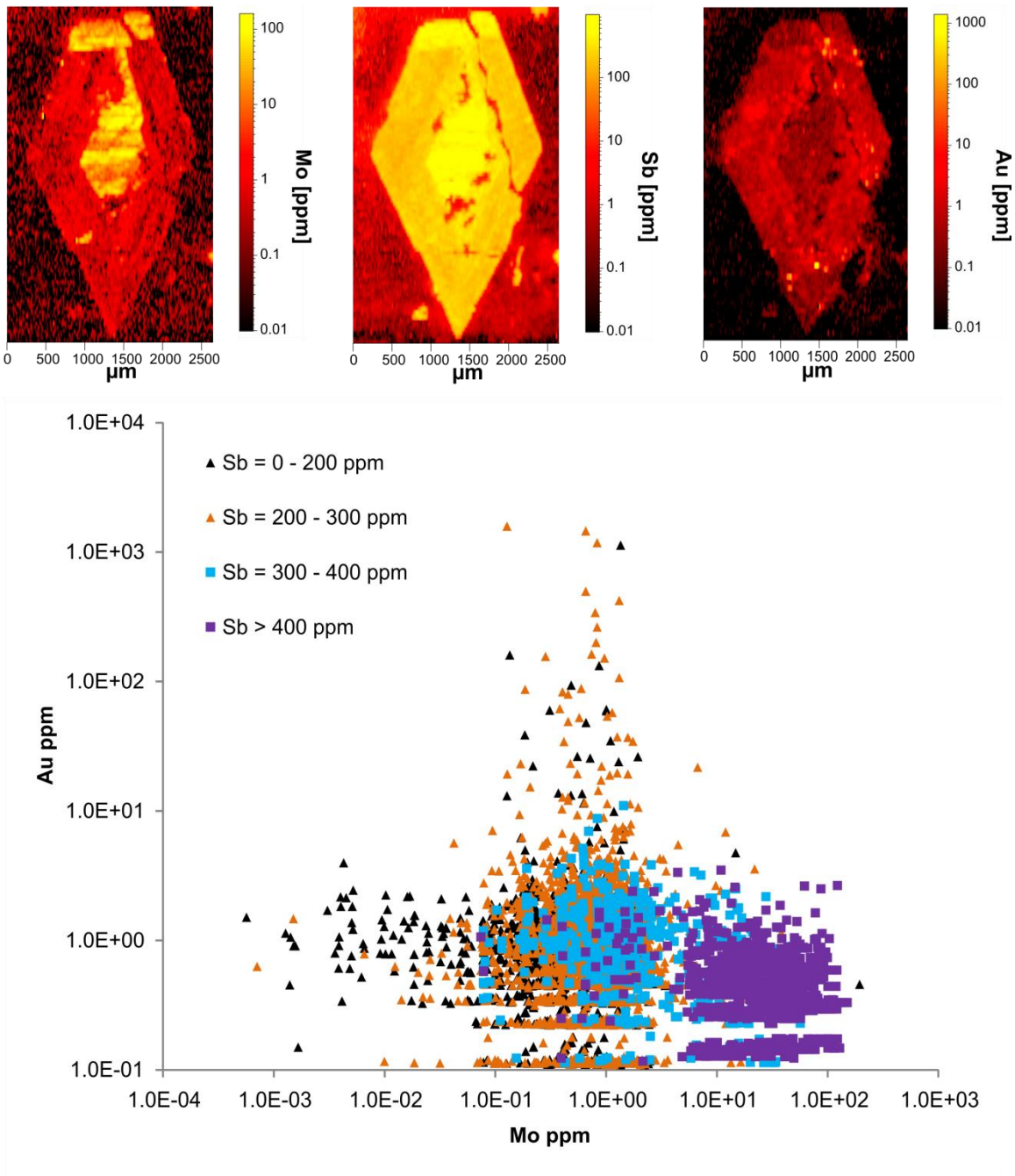

Figure 4.18: Graphical correlation of Sb-Au vs. Mo with LA-ICP-MS maps of the LUP7 (small) arsenopyrite grain with logarithmic scales for Mo, Sb, and Au. The core is Mo- and Sb-rich, but Au-poor. The data set contains 6727 laser spots and is represented in a graphical correlation of Au vs. Mo with Sb brackets.

Chapter 5 – Discussion and conclusion

5.1 – Discussion

5.1.1 – Evaluation of fluid sources

Sulfides, including vein and host sulfides (Table 6), have a $\delta^{34}S_{VCDT}$ distribution of +1.8 to +3.4‰, which is in the magmatic range (Fig. 4.1) and is typical for pyrite ± arsenopyrite ± pyrrhotite assemblages in upper-greenschist/lower-amphibolite gold settings (Mikucki and Ridley, 1993). This isotopic distribution falls within the range of all the other sulfides from gold deposits shown in Fig. 4.1; however, the most closely related isotopic ranges come from the Brazilian sulfides from the Quadrilátero Ferrífero BIF (+1.6 to +5.1‰) and the Salobo and Serquerinha sulfide deposits (+0.2 to +2.9‰). More specifically, the massive chalcopyrites from volcano-sedimentary rocks of the Salobo Au-Cu sulfide deposit (2.57 Ga) have the most similar sulfur isotopic distribution (i.e., +1.6 to +2.9‰) as Lupin (3006 to 2661 Ma) (Table 7). Bühn et al. (2012) postulated an endogenic source of this sulfur for the Salobo deposit, even with microbial sulfate reduction in seawaters starting as far back as 2.7 Ga (Shen et al., 2001). They argued that it cannot be sulfur from a shallow or exogenic source because shallow precipitated sulfides are produced mainly as a by-product of bacterial sulfate reduction and have negative fractionation values ranging from -4.5 to +0.5‰ (Kaplan, 1983). However, this does not imply that the sulfur was sourced directly from a magma; rather, it could have been sourced from metavolcanic rocks during metamorphic fluid production.

Quantification of laser Raman data (Table 9) indicates that type-II fluids have relatively high concentrations of N_2. Fluid inclusion petrography and microthermometry

indicate that the type-I fluid is volumetrically dominant (Table 8), but the N_2 content of type-I fluid is comparatively low. Thus, nitrogen isotope data for the fluid volume in the quartz is dominated by type-II fluid. The value of $\delta^{15}N$ is +7.4‰, which falls within the isotopic range of micas in metasediments and biotite schists (+4.9 to +19.7‰) (Fig. 4.1; Table 4). Micas containing NH_4^+ in the metasedimentary rocks of the Contwoyto Formation (mudstone and sandstone protoliths) could therefore have acted as the N_2 source. This process would have involved the thermal decomposition, volatilization and dehydration of the NH_4^+-rich micas and the subsequent oxidization of ammonium to N_2 (Papineau et al., 2005). The N_2 could have also been sourced from the metamorphic micas of the BIF during hydrothermal activity related to late gold redistribution. The N_2 isotopic data also falls within the ranges for organic matter in oceanic sediments (0 to +10‰) and kerogens in Early Archean and early Proterozoic cherts (+0.3 to +10.1‰) (Fig. 4.1; Table 5). Bottrell et al. (1988) demonstrated that N_2 derived from organic material in sediment can be released to a fluid phase during metamorphism. Nitrogen isotope analysis shows that both organics and/or micas from BIF and/or metasedimentary rocks are strong source possibilities (Fig. 4.1). Sediment is a likely source for N_2 but it is unclear for S because the Lupin iron-formation has an age range of 3006 to 2661 Ma and microbial sulfate reduction in Archean oceans did not start until 2700 Ma (Shen et al., 2001). So, it is hard to distinguish between S isotopes from sediments and those from magmas because most of the depositional history of the BIF and associated rocks happened prior to fractionation due to seawater sulfate reduction.

Fluid inclusion microthermometry and petrography indicate that the non-aqueous CH_4-rich type-I inclusions are volumetrically dominant (Table 8). In addition, gas

chromatography bulk analysis demonstrates that CH_4 is the dominant volatile species in vein quartz; however, there is substantial amounts of CO_2 present (Fig. 4.13, & Fig. 4.14). Calculations demonstrate that molar percentages of CH_4 range from 29.2% to 45.7%, while those of CO_2 range from 24.6% to 26.7%. Therefore, the C isotope signature is dominantly from CH_4 with some contributions from CO_2. The isotope composition of C in CH_4 in vein quartz-hosted fluid inclusions (i.e., -29.9 to -22‰) is in accordance with a thermogenic origin of hydrocarbons (Fig. 4.1). This is the most common carbon isotopic distribution in nature and is generated by the cracking of complex organic molecules in response to heating during diagenesis (Potter et al., 2013). This is a biotic generation of hydrocarbons and involves the preferential breaking of ^{12}C-^{1}H and ^{12}C-^{12}C bonds which forms simpler hydrocarbon species that are enriched in the lighter isotopes. This interpretation of C isotope origin has its limitations due to C contributions from both CH_4 and CO_2.

The limitations of the above interpretation are highlighted by the fact that the carbon isotopic distribution is also in accordance with an F-T-t origin of hydrocarbons (Fig. 4.2). An F-T-t reaction is the abiotic generation of hydrocarbons involving a reaction with CO_2 as the initial reactant, as summarized in the following equation from Potter et al. (2013):

$$nCO_2 + (3n + 1)H_2 \rightarrow C_nH_{2n+2} + 2_nH_2O \qquad (2)$$

The CO_2 in this case is inferred to be of magmatic origin, whereas the initial H_2 reactant is thought to be the product of hydrothermal redox reactions. During an F-T-t reaction, it

is thought that ^{12}C – ^{16}O bonds are broken and ^{12}C is incorporated into CH_4, thus depleting the ^{13}C component in CH_4 relative to the initial amount of ^{13}C in the CO_2 reactant. In addition, intermediate reactions produce lower $\delta^{13}C$ values in the higher hydrocarbons relative to CH_4 by breaking ^{12}C – ^{1}H bonds and forming ^{12}C – ^{12}C bonds.

Furthermore, a log linear Schultz-Flory distribution (plotting log scale concentration versus carbon number of saturated hydrocarbons) suggests that saturated hydrocarbons were generated by abiogenic processes (Fischer-Tropsch, reductive-coupling oligomerization), characterized by the production of a light hydrocarbon-dominated mixture. Although higher order hydrocarbons may be the result of abiogenic processes, the source of the carbon in the system is still unclear (i.e. decomposed organic material, re-speciated/reduced CO_2, re-speciation of graphite). Bulk volatile carbon isotope signatures suggest a thermogenic/biotic origin for the carbon, but without compound-specific carbon isotopic information constrained by compound-specific deuterium isotopic analysis, this conclusion is equivocal.

The authors recommend that further evaluation of the hydrogen isotopic distribution should be performed on fluid inclusion extracts from vein quartz in order to better constrain the origin of the hydrocarbon species. Hydrogen isotopic values below -140 ‰ would suggest an abiogenic source, whereas values above -140 ‰ would point to a biogenic source (Fig. 4.2). The current carbon isotopic signature demonstrates that there could be two sources of hydrocarbons: (i) a biogenic (i.e., thermogenic) source, and (ii) an abiogenic (i.e., F-T-t reaction) source.

Finally, Table 3 shows the following deposits with comparable $\delta^{13}C_{CH4}$ values: the silica-saturated peralkaline rocks of the Illímaussaq complex (-43.4 to -

22.6‰) and peralkaline granitic rocks of the Lovozero and Strange Lake (-32 to -20‰). In terms of the CH_4 source lithology, the presence of graphitic phyllites would have produced CH_4 and other hydrocarbons, and could serve as the source of gold. Other research has shown that graphite is an accessory mineral in the sulfide-rich iron-formation (Bullis et al., 1994).

5.1.2 – Fluid compositions and associated P-T conditions

Bulk compositional analysis of the entrapped fluids demonstrated the diversity of hydrocarbon species, with CH_4 being the primary constituent (Fig. 4.13). However, the area under the CH_4 peak is likely exaggerated because it is presumably superimposed on the CO_2 peak, which shows up immediately after the CH_4 peak on the x-axis (i.e., time), as demonstrated by Fig. 4.14. In addition, laser Raman and microthermometric data provide independent confirmation of the presence of CO_2. The higher order hydrocarbons are made up of single-chain alkanes [i.e., n-butane (C_4H_{10}), n-pentane (C_5H_{12}), and n-hexane (C_6H_{14})], and branched-chain alkanes [i.e., 2, 2-dimethylpropane (C_5H_{12}), and 2-methylbutane (C_5H_{12})]. Also, there are single-chain alkenes [i.e., propene (C_3H_6), 1-butene (C_4H_{10}), 1-pentene (C_5H_{10}), c-2-pentene (C_5H_{10}), and 1-hexene (C_6H_{12})] and a branched-chain alkene [isobutene (C_4H_{10})]. Finally, there is toluene (C_7H_8), which is an aromatic hydrocarbon.

The entrapped fluids are partly hosted in two petrographically distinct single-phase non-aqueous fluid inclusion types, classified as type-I and type-II (Fig. 4.7). That these containing volatile species (CH_4, N_2, H_2S) are homogenously distributed in the inclusions is reflected visually in two-dimensional composition maps for single inclusions obtained by Raman spectroscopy (Fig. 4.12). Type-II fluid inclusions are early

secondary (ES) in origin and formed as grain boundaries sealed up after most of the host quartz had already grown (Fig. 4.7). Type-I fluid inclusions are considered late secondary (LS) because they crosscut these healed grain boundaries that host type-II fluids (Fig. 4.7).

Type-I inclusions homogenize to a liquid phase between -89.5˚C (Q1) and -88.8˚C (Q3) and have an average variation of 0.6°C within a FIA (Table 8; Fig. 4.8). This means there is a range in CH_4:N_2 ratios or variable P from assemblage to assemblage. Fluid inclusion assemblage IV was considered an outlier because of its anomalously low T_h values, ranging from -112.0 to -111.0°C (Table 8; Fig. 4.8), which could indicate high concentrations of N_2. Laser Raman measurements of type-I inclusions (Fig. 4.9) confirm this variability in volatile composition, with CH_4:N_2 ratios ranging from 7.1 (Q1) to 10.6 (Q3), with an average of 8.8. Specifically, CH_4 concentrations range from 87.1 (Q1) to 90.7 (Q3) mol% and N_2 concentrations range from 8.6 (Q1) to 12.2 (Q3) mol% (Table 9), and their averages are 88.6 and 10.8 mol%, respectively. The variability of CH_4 and N_2 within the same FIA is 3 mol%, with a standard deviation of 1 mol%. The volatile composition of type-I fluids is relatively enriched in CH_4 when compared to type-II fluids and other lode gold deposits, such as eclogite, granulites, and slates (Fig. 4.11). Type-I fluids are also relatively enriched in H_2S when compared to eclogites, granulites, high-grade greenschist to low-grade amphibolite rocks, and slates. Type-I fluids are relatively depleted in N_2 when compared to type-II fluids, slates, and some eclogites but are more consistent with the eclogite-hosted quartz fluid inclusions studied by Andersen et al. (1989) in the Western Gneiss Region of the Norwegian Caledonides.

Type-II inclusions (Fig. 4.7) homogenize mainly to a liquid phase (but sometimes to vapor or show super critical behavior) between -25.6°C (Q1) and -19.1°C (Q3) (Table 8; Fig. 4.8), thus consistent with a range in CO_2:CH_4 ratios or variable P from assemblage to assemblage. Laser Raman measurements of the volatile contents confirm this variability in type-II inclusions (Fig. 4.9), with variable CO_2:CH_4 ratios ranging from 1.8 (Q1) to 2.9 (Q3) and an average of 2.4 (Table 9). The range in molar concentration of CO_2, from 30 to 61 mol%, is also noted to be significantly higher than the average X_{CO2} for sub-amphibolite facies Archean lode-gold deposits, which generally fall between 5 to 25 mol%) (Mikucki and Ridley, 1993). The volatile composition of type-II fluids is relatively enriched in CO_2 when compared to type-I fluids and other lode gold deposits, such as slates and some high-grade greenschist to low-grade amphibolite rocks (Fig. 4.11). Type-II fluids are also relatively enriched in H_2S when compared to eclogites, granulites, high-grade greenschist to low-grade amphibolite rocks, and slates. Furthermore, type-II inclusions are relatively enriched in CH_4 when compared to eclogites, granulites, and slates. However, type-II fluids are relatively depleted in N_2 when compared to slates, and some eclogites.

Although there is variability in T_h between FIAs for both type-I and type-II inclusions, the T_h for inclusions belonging to the same FIA show low variability and in some cases inclusions in the same FIA having identical T_h values (Table 8). Homogenization temperatures belonging to the same FIA vary, on average, by 0.6 ˚C for type-I and 0.8 ˚C for type-II. However, additional measurements should be done on type-II FIAs because FIA 11 is suspected of post-entrapment leakage and/or stretching, and FIA 12 only has 1 inclusion measurement. This leaves only FIA 13 as a reliable source

for inclusion measurements for average T_h variance. Moreover, a deeper investigation into type-II microthermometric characteristics could provide information regarding the dominant mode of homogenization.

Crowell (unpublished) recorded Raman spectra of aqueous inclusions (Fig. 4.10) which show enrichment in CH_4. Interestingly, some inclusions contain H_2 – a species that is not present in type-I and type-II inclusions and which is interesting because H_2 is rarely found in fluid inclusions (Peretti et al., 1992). The reasons why H_2 is not reported relates to several features: i) fluid inclusions cool after being trapped and the system C-O-H-(N-S) is re-equilibrated, hence very low concentrations of H_2 result – so low that H_2 becomes undetectable by micro-Raman analysis; ii) high redox states of the initial geothermal fluids prevent stabilization of H_2; and iii) H_2 is prone to diffusion and would not remain as a volatile species in the inclusions. The presence of H_2 suggests that the aqueous inclusions could have been formed under strong reducing conditions.

Isochores for type-I and type–III (Crowell, unpublished) inclusions were generated from their respective measured homogenization temperatures and calculated densities, and presented in Fig. 5.1. The method of intersecting isochores shows that type-I inclusions were entrapped within a P-T window of 320 to 490˚C and 1.2 to 2.2kbar. The miscibility field ranges from 420-490˚C and 1.5-2.2kbar. The immiscibility field, representing the range of conditions of entrapment of the type I-III inclusions, and conditions at which gold precipitation occurred by several suspected mechanisms, ranges from 320-420˚C and 1.2-2kbar. The immiscibility/miscibility field constrained by the method of intersecting isochores represents the P-T conditions for two intermingling fluids (i.e., type-I and type-III) that were entrapped in the late stage "ladder" crack-

seal/ribbon-textured quartz veins (Fig. 4.3). Based on petrographic observations, this study has determined a process of fluid mixing rather than decompression of a single-phase fluid (Fig. 4.7). If all of the entrapped fluid inclusions originated from an immiscible process, it would be argued that a single-phase fluid evolved prior to vein formation and was decompressed because of the transition from regional D2 compression to D_{NE-NW} shearing during emplacement of batholiths (King et al., 1988, 1992; Relf, 1989; Geusebroek and Duke, 2005; van Breemen et al., 1992). However, petrographic observations show isolated domains of type-I and type-III fluids, and only locally do FIAs contain both fluids (i.e., coeval entrapment of a heterogeneous fluid mixture) (Fig. 4.7). Judging by this textural association of fluid inclusions, it is more reasonable to assume that type-I and type-III fluids developed independently, were sourced separately and subsequently interacted or mixed in the structures that now host the mineralized quartz veins. The fluids were entrapped as heterogeneous fluid inclusions when subjected to conditions associated with the immiscible field (i.e., 320 to 420˚C and 1.2 to 2 kbar) (Fig. 5.1).

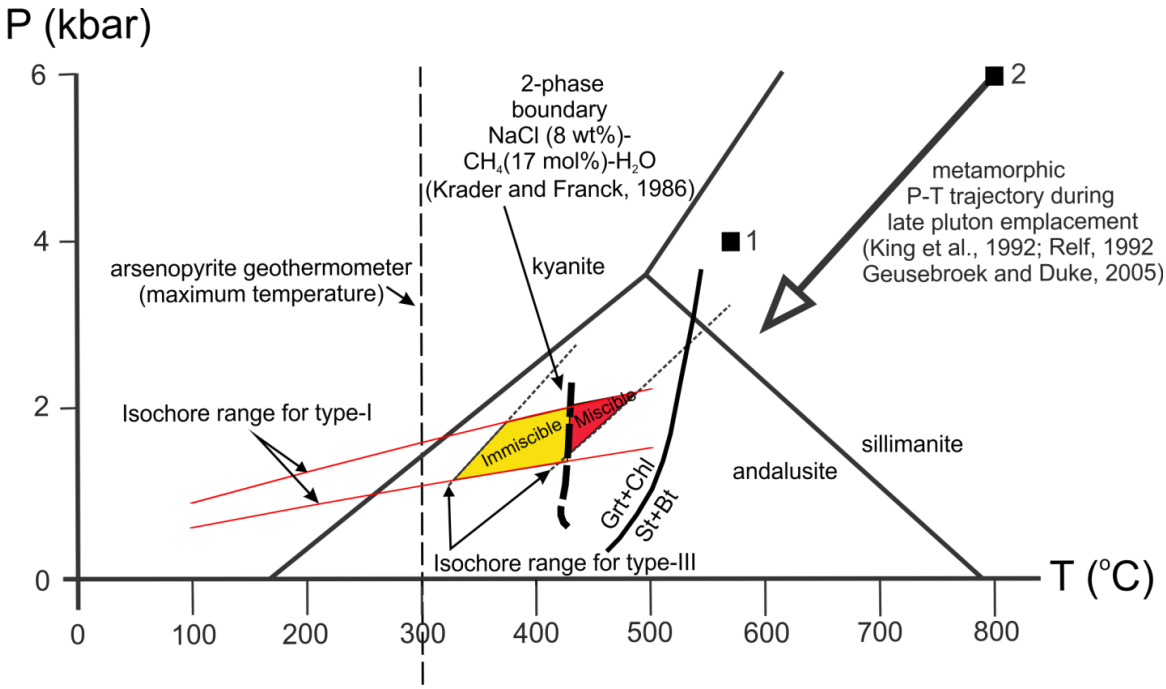

Figure 5.1: The inferred P-T window for quartz-vein hosted type-I and type-III fluid inclusion in samples from the Lupin gold deposit using the method of intersecting isochores and the constraints determined from this study. Also included are relevant immiscibility conditions and the peak metamorphic conditions associated with the D2-D_{NE-NW} transition. A P-T boundary determined by Krader and Franck (1986) for the NaCl-H_2O-CH_4 system is drawn to separate the single-phase field (miscible) from the two-phase field (immiscible). The miscible field ranges from 420 - 490˚C and 1.5 – 2.2 kbar whereas the immiscible field ranges from 320 - 420˚C and 1.2 – 2kbar. Gold deposition in quartz veins occurred in the "immiscible" range. The arsenopyrite geothermometer is based on SEM-EDS, which represents the temperature of final equilibration associated with the crystallization of arsenopyrite from loellingite (Fig. 4.15). Peak metamorphic conditions determined by various researchers are displayed.
[1]Ford and Duke (1993) used a grt-bt geothermometer on the stable prograde metamorphic assemblage of enveloping metapelites (quartz + grunerite + hornblende + pyrrhotite ± garnet ± graphite ± ilmenite) and found peak metamorphic conditions of 570˚C and 4 kbar.
[2]King et al. (1992) and Relf (1992) postulated that mineral assemblages (i.e., biotite + muscovite + quartz + plagioclase + Fe oxides ± sillimanite ± cordierite ± garnet ± staurolite ± tourmaline) and geothermobarometry pointed to peak metamorphic conditions of 800˚C and 6 kbar.

5.1.3 – Arsenopyrite – complexity in composition

The incorporation of major and trace elements into arsenopyrite is achieved by precipitation, co-precipitation, chemical or physical absorption and redox reactions at the grain surface (Dellwig et al., 2002 and Berner et al., 2013). The concentrations of major and trace elements incorporated into arsenopyrite grains adjacent to late quartz veins were investigated using LA-ICP-MS elemental mapping. Select maps and time series are presented in Section 4.6. The selection of the essential elemental maps shown was carried out through careful analysis of each major and trace element and their relationship to Au.

The logarithmic scale map for Au of grain LUP7 (small) shows that nanoparticles of Au in the matrix of the arsenopyrite grain and electrum increased as the arsenopyrite grain grew (Fig. 4.18). This increase in Au-nanoparticles and electrum is associated with a late Sb-Mo dissolution replacement event. That is to say, the low Sb-Mo part of the crystal contains more Au, which suggests that Au precipitation is associated with a decrease in Sb and Mo.

The elemental S map of LUP7 (small) (Appendix B, Fig. I) shows a pervasive distribution of S throughout the grain, which means loellingite is not present or loellingite inclusions are below the spatial resolution of the laser beam, which is roughly 20 μm. The absence of large loellingite inclusions suggests that loellingite is not an important determinant in controlling gold distribution.

Graphical correlations of all quantified ablation spots obtained through the mapping of arsenopyrite grains show no elemental association with Au. Tellurium in LUP7 (big) is the most glaring example of a non-correlative relationship of an arsenopyrite trace element and Au content (Fig. 4.16). An additional example of this lack

of correlation is for Au and As, which show no apparent relationship (Fig. 4.17). This lack of relationship noted suggests that when arsenopyrite formed from loellingite by sulfurization, as discussed above, there was no change in Au concentration, rather the Au is simply redistributed from lattice-dissolved to matrix micro-inclusions. This non-correlative relationship between As and Au is common in sediment-hosted, Lupin-like, stratiform deposits (Table 1).

The lack of correlation between Au and other trace elements is interesting because the LA-ICP-MS elemental distribution maps clearly indicate that certain trace elements show preferential distribution in zones relating to different growth stages of the arsenopyrite grains (Appendix B). In other words, these trace element distributions imply a series of events during crystal growth, yet Au concentrations do not prefer any distinct event.

The assemblage arsenopyrite-pyrrhotite-(pyrite) allows for an estimation of the minimum temperature of crystallization and S_2 fugacity associated with vein formation (Kretschmar and Scott, 1976) (Fig. 4.15). The minimum temperature of final equilibration associated with the crystallization of arsenopyrite from loellingite is <300˚C. This reaction requires either a significant decrease in temperature or an increase in S_2 fugacity [see reaction (1) in Section 4.6], or both. This temperature of final equilibration is significantly lower than those identified for mineral assemblages of the Contwoyto Lake area containing loellingite, indicating that there needs to be a significant drop in temperature in order for arsenopyrite to fully replace loellingite (Kretschmar, 1973; & Bostock, 1968).

5.1.4 – Implications for gold deposition and exploration

Gold remobilization is late with respect to arsenopyrite formation and quartz veins (Fig. 4.6). Bullis et al. (1994) describes arsenopyrite as being formed in the alteration halo of the quartz veins. The X-ray elemental distribution maps in Fig. 4.6 show that Au was deposited even later than the alteration event because it is infilling fractures in arsenopyrite grains. In addition to Au infilling fractures in the rock that is adjacent to the quartz veins, it also infills fractures in the quartz veins themselves, which might indicate multiple generations of remobilization. This late Au depositional event in the quartz veins is associated with secondary fluid inclusions along grain boundaries (type-II) and fractures healed but cutting grain boundaries (type-I).

The conditions of entrapment for the fluid inclusions associated with secondary gold enrichment are well below peak P-T metamorphic conditions and even cooler than the minimum temperature associated with the latest stages of pluton emplacement (Fig. 5.1). Ford and Duke (1993) used a garnet-biotite geothermometer on the stable prograde metamorphic assemblage of enveloping metapelites (quartz + grunerite + hornblende + pyrrhotite ± garnet ± graphite ± ilmenite) and found peak metamorphic conditions of 570˚C and 4 kbar. King et al. (1992) and Relf (1992) postulated that mineral assemblages of biotite + muscovite + quartz + plagioclase + Fe-oxides ± sillimanite ± cordierite ± garnet ± staurolite ± tourmaline and geothermobarometry pointed to peak metamorphic conditions of 800˚C and 6 kbar. SEM-BSE images of minerals in a quartz vein selvage show chlorite within matrix sulfides and chloritized hornblende which indicates that early prograde metamorphism was followed by retrograde metamorphism (Fig. 4.5). The conditions of entrapment are in accord with the precipitation of gold in vein selvages with

the assemblage chlorite + garnet and fall into the andalusite field. This is consistent with past research that has found andalusite occurring as 2-mm to 3-cm xenoblasts in mica-dominant rocks in the metasedimentary pile that bounds the main Lupin iron formation unit (Geusebroek & Duke, 2004). If gold precipitation occurred as a result of immiscibility, it occurred in the low P-T range already noted for the fluid entrapment conditions.

The immiscibility field for a fluid of NaCl (8 wt.%)-CH_4(17 mol%)-H_2O composition encompasses much greater P-T range than a fluid of NaCl (9 wt%)-CO_2(17 mol%)-H_2O composition, thus implying that gold precipitation from the CH_4-rich fluid could happen at greater depths than the CO_2-rich fluids (Fig. 1.1, Fig. 5.1). Considering a stable metamorphic geothermal gradient which is used for orogenic gold systems, precipitation could have occurred at temperatures of ~100°C greater than for CO_2-rich fluids, which is proportional to roughly 3-5km in depth. If this scenario is right, then it may explain the lack of gold enrichment associated with quartz veining in the shallower parts of the deposit because immiscible fluids that entered structures from depth had already precipitated gold.

Fluid inclusion studies have shown that gold ore fluids normally contain a mix of CO_2/CH_4-rich and H_2O-rich phases, and an integral part of gold deposition is the process of phase separation (Naden, & Shepherd, 1989). It is possible that gold-bearing bi-hydrosulfide complexes ($Au(HS)_2^-$) were neutralized, cooled, and diluted around 320 to 420˚C and 1.2 to 2kbar (i.e., immiscibility field) when the type-I and type-III fluids mixed. This reaction would have forced the gold to drop out of the bi-hydrosulfide-bearing fluid and for H_2S to be partitioned into the vapor phase. It is unlikely that the

type-II fluid influenced gold deposition because of its observed high concentration of N_2 (Table 9). If the type-II fluid mixed and reacted with the type-III fluid, there would be residual N_2 in the vapor bubbles of the two-phase inclusions found in mixed FIAs. However, these vapor bubbles do not contain N_2 (Fig. 4.10). In addition, significantly more CO_2 is soluble under these low P-T conditions, so the extent of the reaction needed to initiate immiscibility is much greater. Thus, fluid immiscibility and the precipitation of gold are favored by the production of CH_4 as the dominant volatile species upon reaction with graphite (assuming reducing conditions where the ambient f_{O2} is low):

$C + 2H_2O \leftrightarrow CH_4 + 2[O]$, where O represents oxygen bound in carbon dioxide and/or carbonate (3)

Additionally, the lowering of f_{O2} would produce H_2S and CH_4 vapor, as well as the precipitation of gold because it forces reaction (3) to the right. Hydrogen sulfide and CH_4 are found in the type-I inclusions, so this is a possibility for gold precipitation.

Figure 4.6 shows that magnetite + pyrrhotite + gold coexist in a veinlet that crosscuts an arsenopyrite grain. For this assemblage to result, Gibert et al. (2013) explained that pH has to increase so that magnetite can be stable in the presence of pyrrhotite. In response to the increase in pH, the amount of sulfur and gold in solution would decrease and reaction (4) would make an equilibrium shift to the left. In addition, the assemblage magnetite + pyrrhotite + gold could have formed due to a change in the oxidation state. The system would need to have an overall fO_2 that is quite high, and near

the border of the magnetite-hematite stability fields because this is where small variations in fO_2 can strongly influence the gold concentration in solution.

$$Au + H_2O + HS^- + H_2S = Au(HS)_2^- + H_2O \quad (4)$$

Mixed FIAs have non-aqueous type-I and aqueous type-III fluid inclusions (Fig. 4.7). Type-III contains sulfate which could have formed if a CH_4- and H_2S-rich fluid interacted with a highly oxidized aqueous fluid. The H_2S and HS^- species would be destroyed and reaction (4) would re-equilibrate to the left, causing gold to drop out. If the CH_4 fluid initially contained the gold-bearing di-bisulfide complexes, it would have to interact with a more neutral (i.e., non-acidic) or oxidizing aqueous fluid. It is also possible that this could cause Au to partition into the CH_4 fluid the gold-bearing complexes originated in the aqueous fluid instead.

5.2 – Conclusion

Sulfides have a $\delta^{34}S_{VCDT}$ range of +1.8 to +3.4 ‰, which is in the magmatic range and is typical for pyrite ± arsenopyrite ± pyrrhotite assemblages in upper-greenschist/lower-amphibolite gold settings. However, sulfur could have been sourced from metavolcanic rocks during metamorphic fluid production and is, therefore, not necessarily sourced directly from a magma. Furthermore, it is hard to distinguish between S isotopes from sediments and those from magmas because most of the depositional history of BIF and associated rocks at Lupin (i.e., 3006 to 2661 Ma) happened prior to fractionation due to seawater sulfate reduction (i.e., 2700 Ma). Vein quartz fluid inclusions have a $\delta^{15}N_{AIR}$ value of +7.4‰, which is in the range of N_2 sourced from

micas in metasediments and biotite schists (+4.9 to +19.7 ‰), as well as N_2 derived from organic matter in oceanic sediments (0 to +10‰). Therefore, N_2 could have originated in micas and/or organics in BIF and/or metasedimentary rocks in the Contwoyto Lake area. Vein quartz fluid inclusions have a $\delta^{13}C_{VPDB}$ range of -29.9 to -22 ‰, which is in the thermogenic/biogenic range. However, this range is also in a F-T-t reaction field (i.e., abiogenic origin) as indicated by a $\delta^{13}C$ vs. δD diagram. Therefore, more analysis (e.g., compound specific carbon isotope analysis, deuterium isotope analysis) needs to be done to distinguish between a biogenic vs. abiogenic origin for carbon.

Bulk compositional analysis of the entrapped fluids demonstrated the diversity of hydrocarbon species, with CH_4 being the primary constituent. The entrapped fluids are partly hosted in two petrographically distinct single-phase non-aqueous fluid inclusion types, classified as type-I (CH_4-N_2-H_2S) and type-II (CO_2-CH_4-N_2-H_2S). Type-II fluid inclusions (T_h range = -25.6°C to -19.1°C) are early secondary in origin and formed as grain boundaries sealed up after most of the host quartz had already grown. Type-I fluid inclusions (T_h range = -89.5˚C to -88.8˚C), which can be grouped in the same trail as aqueous type-III inclusions (H_2O-CH_4), are considered late secondary because they crosscut the healed grain boundaries that host type-II fluids. Type-I and type-II inclusions have variable CH_4:N_2 (7.1 to 10.6) and CO_2:CH_4 (1.8 to 2.9) ratios, respectively, which can explain the variance seen in homogenization temperatures. Both types-I and -II inclusions are relatively enriched in H_2S when compared to inclusions found in eclogites, granulites, and high-grade greenschist to low-grade amphibolite rocks. The fact that H_2S is so abundant in type-I inclusions indicates that as the system reached its range of immiscibility (320 to 420˚C and 1.2 to 2 kbar) and type-I and –III fluids mixed, there was

a phase separation where gold-bearing bi-hydrosulfide complexes were neutralized, cooled and diluted, gold dropped out and H_2S was partitioned into the vapor phase.

Laser ablation analysis of arsenopyrite grains indicate a lack of correlation of gold with other trace elements but X-ray elemental intensity maps of a late pyrrhotite-electrum vein crosscutting an arsenopyrite grain show textural evidence of the history of gold precipitation. The crosscutting texture indicates that gold remobilization is late with respect to arsenopyrite formation and quartz veins, which are associated with the arsenopyrite alteration haloes. In addition, the assemblage arsenopyrite-pyrrhotite-(pyrite) allowed for a calculation of the temperature of final equilibration of arsenopyrite (<= 300˚C) through SEM-EDS analysis of arsenic in arsenopyrite.

Comparing the position of mapped metamorphic assemblages, volatile-fertile protoliths, and structures to the volatile and host-rock chemistry of quartz vein selvages in the gold orebody could prove to be a reliable means to delineate zones of secondary gold deposition. This paper provides further characterization of the vein quartz fluid inclusions and their vein selvages through laser Raman microscopy, fluid inclusion bulk analysis, fluid inclusion petrography, microthermometry, LA-ICP-MS, and C-N-S isotope systematics. Its findings provide a guide for source rock determination, possible processes for Au remobilization, and subsequent delineation of secondary Au deposition.

References

Adomako-Ansah, K., Mizuta, T., Hammond, N. Q., Ishiyama, D., Ogata, T., & Chiba, H. (2012). Gold Mineralization in Banded Iron Formation in the Amalia Greenstone Belt, South Africa: A Mineralogical and Sulfur Isotope Study. *Resource Geology, 63*(2), p. 119-140.

Andersen, T., Austrheim, H., & Burke, E. A. (1990). Fluid inclusions in granulites and eclogites from the Bergen Arcs, Caledonides of W. Norway. *Mineralogical Magazine, 54*, 145-158.

Andersen, T., Burke, E. A., & Austrheim, H. (1989). Nitrogen-bearing, aqueous fluid inclusions in some eclogites from the Western Gneiss Region of the Norwegian Caledonides. *Contributions to Mineralogy and Petrology, 103*, 153-165.

Andrawes, F., & Gibson, E. K. (1979). Release and analysis of gases from geological samples. *American Mineralogist, v. 64*, p. 453-463.

Andrawes, F., Holzer, G., Roedder, E., Gibson, E. K., & Oro, J. (1984). Gas chromatographic analysis of volatiles in fluid and gas inclusions. *Journal of Chromatography A, v. 302*, p. 181-193.

Baker, D. E., & Seccombe, P. K. (2004). Physical conditions of gold deposition at the McPhees deposit, Pilbara Craton, Western Australia: fluid inclusion and stable isotope constraints. *The Canadian Mineralogist, 42*, 1405-1424.

Bakker, R. J. (1999). Adaptation of the Bowers and Helgeson (1983) equation of state to the H2O–CO2–CH4–N2–NaCl system. *Chemical Geology, 154*(1-4), 225–236.

Bakker, R. J. (2003). *Chemical Geology, 194*, 3-23.

Beaumont, V., & Robert, F. (1999). Nitrogen isotope ratios of kerogens in Precambrian cherts: a record of the evolution of atmosphere chemistry? *Precambrian Research, 96*(1-2), p. 63-82.

Beeskow, B., Rankin, A. H., Murphy, P. J., & Treloar, P. J. (2005). Mixed CH4-CO2 fluid inclusions in quartz from the South Wales Coalfield as suitable natural calibration standards for microthermometry and Raman spectroscopy. *Chemical Geology, 223*, pp. 3-15.

Beeskow, B., Treloar, P. J., Rankin, A. H., Vennemann, T. W., & Spangenberg, J. (2006). A reassessment of models for hydrocarbon generation in the Khibiny nepheline syenite complex, Kola Peninsula, Russia. In: Potter, J., Salvi, S., & Longstaffe, F.

J. (2013). Abiogenic hydrocarbon isotopic signatures in granitic rocks: Identifying pathways of formation. Lithos(182-183), p. 114-124.

Bekker, A., Barley, M. E., Fiorentini, M. L., Rouxel, O. J., Rumble, D., & Beresford, S. W. (2009). Atmospheric sulfur in Archean komatiite-hosted nickel deposits. *Science, 326*, p. 1086-1089.

Berner, Z. A., Puchelt, H., Noltner, T., & Kramer, U. T. (2013). Pyrite geochemistry in the Toarcian Posidonia Shale of south-west Germany: Evidence for contrasting trace-element patterns of diagenetic and syngenetic pyrites. In: Gregory, D. D., et al. (2015). The chemical conditions of the late Archean Hamersley basin inferred from whole rock and pyrite geochemistry with Δ33S and δ34S isotope analyses. Geochimica et Cosmochimica Acta, 149, p. 223-250.

Beukes, N. J. (1973). Precambrian iron-formation of Southern Africa. In: Khalil, K. I., et al. (2015). Late Neoproterozoic banded iron formation (BIF) in the central Eastern Desert of Egypt: Mineralogical and geochemical implications for the origin of the Gebel El Hadid iron ore deposit. Ore Geology Reviews, In Press.

Bierlein, F. P., & Crowe, D. E. (2000). Phanerozoic orogenic lode gold deposits. In S. G. Hagemann, & P. E. Brown, *Reviews in Economic Geology* (pp. 103-137). Littleton, CO: Society of Economic Geologists.

Bodnar, R. J., & Vityk, M. O. (1994). Interpretation of microthermometric data for H2O-NaCl fluid inclusions. In B. De Vivo, & M. L. Frezzotti, *Fluid inclusions in minerals, methods and applications* (pp. 117-130). Blacksburg, VA: Virginia Tech.

Bostock, H. S. (1968). Gold - arsenopyrite - loellingite - pyrrhotite deposits in amphibolite, Itchen Lake - Contwoyto Lake area, District of MacKenzie. *Geological Survey of Canada Paper, 68-1B*, 72-76.

Bottrell, S. H., Carr, L. P., & Dubessy, J. (1988). A nitrogen-rich metamorphic fluid and coexisting minerals in slates from North Wales. *Mineralogical Magazine, 52*, 451-457.

Bowers, T. S., & Helgeson, H. C. (1983). Calculation of the thermodynamic and geochemical consequences of nonideal mixing in the system H2O–CO2–NaCl on phase relations in geological systems: equation of state for H2O–CO2–NaCl fluids at high pressures and temperatures. *Geochim. Cosmochim. Acta, 47*, 1247–1275.

Bowins, R. J., & Crocket, J. H. (1994). Sulfur and carbon isotopes in Archean banded iron formations: Implications for sulfur sources. *Chemical Geology, 111*(1-4), p. 307-323.

Boyd, S. R., & Philippot, P. (1998). Precambrian ammonium biogeochemistry: a study of the Moine metasediments, Scotland. *Chemical Geology, 144*, 257–268.

Bühn, B., Santos, R. V., Dardenne, M. A., & de Oliveira, C. G. (2012). Mass-dependent and mass-independent sulfur isotope fractionation (δ34S and δ33S) from Brazilian Archean and Proterozoic sulfide deposits by laser ablation multi-collector ICP-MS. *Chemical Geology, 312-313*, p. 163-176.

Bullis, H., Hureau, R. A., & Penner, B. D. (1994). Distribution of Gold and Sulfides at Lupin, Northwest Territories. *Bulletin of the Society of Economic Geologists, Economic Geology, v. 89*, p. 1217-1227.

Burke, E. A. (2001). Raman microspectrometry of fluid inclusions. *Lithos, 55*(1-4), pp. 139–158.

Charlou, J. L., Donval, J. P., Fouquet, Y., Jean-Baptiste, P., & Holm, N. (2002). Geochemistry of high H2 and CH4 vent fluids issuing from ultramafic rocks at the Rainbow hydrothermal field (36 14′N, MAR). In: Potter, J., Salvi, S., & Longstaffe, F. J. (2013). Abiogenic hydrocarbon isotopic signatures in granitic rocks: Identifying pathways of formation. Lithos(182-183), p. 114-124.

Chryssoulis, S., & Agha, U. (1996). Determination of "invisible" gold carrier minerals in selected ore zones of the Lupin mine, N.W.T. *Technical Report, Process Mineralogy, Surface Science Western, 20*.

CNW Group Ltd. (2014, Sept. 10). *Mandalay Resources Completes Acquisition of Elgin Mining.* Retrieved January 29, 2015, from CNW Group: A PR Newswire Company: http://cnw.ca/yqViN

Crowell, S. (Unpublished). Directed study: Microthermometry of Lupin quartz vein liquid-rich fluid inclusions. Saint Mary's University.

Dee, S. J., & Roberts, S. (1993). Late kinematic gold mineralization and the role of anomalous nitrogen; an example from the La Codosera area, SW Spain. *Mineralogical Magazine, 57*, 437-450.

Dellwig, O., Böttcher, M. E., Lipinski, M., & Brumsack, H. J. (2002). Trace metals in Holocene coastal peats and their relation to pyrite formation (NW Germany). In: Gregory, D. D., et al. (2015). The chemical conditions of the late Archean

Hamersley basin inferred from whole rock and pyrite geochemistry with Δ33S and δ34S isotope analyses. Geochimica et Cosmochimica Acta, 149, p. 223-250.

Driesner, T. (2007). The System H2O-NaCl. II. Correlation Formulae for Phase Relations in Temperature-Pressure-Composition Space from 0 to 1000°C, 0 to 5000 bar, and 0 to 1 XNaCl. *Geochimica et Cosmochimica Acta, 71*, 4880-4901.

Driesner, T., & Heinrich, C. A. (2007). The System H2O-NaCl. I. Correlations for molar volume, enthalpy, and isobaric heat capacity from 0 to 1000 degrees C, 1 to 5000 bar, and 0 to 1 XNaCl. *Geochimica et Cosmochimica Acta, 71*(20), 4902-4919.

Duan, Z., Moller, N., & Weare, J. H. (2003). Equations of state for the NaCl-H20-CH4 system and the NaCl-H2O-CO2-CH4 system: phase equilibria and volumetric properties above 573 K. *Geochimicaet et Cosmochimica Acta, 67*, 671-680.

Dubessy, J., Poty, B., & Ramboz, C. (1989). Advances in C-O-H-N-S fluid geochemistry based on micro-Raman spectrometric analysis of fluid inclusions. *European Journal of Mineralogy, 1*(4), pp. 517 - 534.

Eldridge, C. S., Compston, W., Williams, I. S., Harris, J. W., Bristow, J. W., & Kinny, P. D. (1995). Applications of the SHRIMP I ion microprobe to the understanding of processes and timing of diamond formation. *Economic Geology, 90*, p. 271-280.

Elvevold, S., & Andersen, T. (1993). Fluid evolution during metamorphism at increasing pressure: carbonic- and nitrogen-bearing fluid inclusions in granulites from Oksfjord, north Norwegian Caledonides. *Contrib. Mineral. and Petrol., 114*, 236-246.

Ford, R. C., & Duke, N. A. (1993). Concentration of gold during retrograde metamorphism of Archean banded iron formations, Slave Province, Canada. *Canadian Journal of Earth Sciences, 30*(8), p. 1566-1581.

Geusebroek, P., & Duke, N. A. (2004). An update on the geology of the Lupin gold mine, Nunavut, Canada. *Exploration and Mining Geology, v. 13*(n. 1-4), p. 1-13.

Goldfarb, R. J., Baker, T., Dubé, B., Groves, D. I., Hart, C. J., & Gosselin, P. (2005). Distibution, character, and genesis of gold deposits in metamorphic terranes. *Economic Geology, 100th Anniversary Volume*, 407-450.

Goldfarb, R. J., Groves, D. I., & Gardoll, S. (2001). Orogenic gold and geologic time: a global synthesis. *Ore Geology Reviews*, pp. 1-75.

Graser, G., Potter, J., Köhler, J., & Markl, G. (2008). Isotope, major, minor and trace element geochemistry of late-magmatic fluids in the peralkaline Ilímaussaq intrusion, South Greenland. In: Potter, J., Salvi, S., & Longstaffe, F. J. (2013).

Abiogenic hydrocarbon isotopic signatures in granitic rocks: Identifying pathways of formation. Lithos(182-183), p. 114-124.

Gregory, D. D., Large, R. R., Halpin, J. A., Steadman, J. A., Hickman, A. H., Ireland, T. R., et al. (2015). The chemical conditions of the late Archean Hamersley basin inferred from whole rock and pyrite geochemistry with Δ33S and δ34S isotope analyses. *Geochimica et Cosmochimica Acta, 149*, p. 223-250.

Groves, D. I., Goldfarb, R. J., Gebre-Mariam, M., Hagemann, S. G., & Robert, F. (1998). Orogenic gold deposits: A proposed classification in the context of their crustal distribution and relationship to other gold deposit types. *Ore Geology Reviews, 13*, 7-27.

Guilhaumou, N., Santos, M., Touray, J. C., Beny, C., & Dardenne, M. (1990). Multiphase methane-rich fluid inclusions in gold-bearing quartz as illustrated at Pontal (Goias, Brazil). *Mineralogical Magazine*, *54*, 257-266.

Guillong, M., Meier, D. L., Allan, M. M., Heinrich, C. A., & Yardley, B. W. (2008). SILLS: A MATLAB-based program for the reduction of laser ablation ICP-MS data of homogeneous materials and inclusions. *Mineralogical Association of Canada Short Course, 40*, (pp. 328-333).

Gwinnett, G. (2015, Jan. 19). *Mandalay Resources Strikes Deal to Sell Lupin Gold Mine.* Retrieved Jan. 29, 2015, from Proactive Investors: USA & Canada: http://www.proactiveinvestors.com/companies/news/59344/mandalay-resources-strikes-deal-to-sell-lupin-gold-mine--59344.html

Hayashi, K. I., & Ohmoto, H. (1991). Solubility of gold in NaCl- and H2S-bearing aqueous solution at 259-350˚C. *Geochim. Cosmochim. Acta, 55*, 2111-2126.

Heinrich, C. A., Driesner, T., Stefansson, A., & Seward, T. M. (2004). Magmatic vapor contraction and the transport of gold from the porphyry environment to epithermal ore deposits. *Geology, 32*, 761-764.

Henderson, J., & Easton, R. M. (1977). Archean supracrustal basement-rock relationships in the Keskarrah Bay map-area, Slave structural province, District of MacKenzie. *Canada Geological Survey Paper, v. 77-1A*, p. 217-221.

Huston, D. L., & Logan, G. A. (2004). Barite, BIFs and bugs: evidence for the evolution of the Earth's early hydrosphere. *Earth Planet Science Letters*, *220*, p. 41-55.

Jamieson, J. W., Wing, B. A., Hannington, M. D., & Farquhar, J. (2006). Evaluating isotopic equilibrium among sulfide mineral pairs in Archean ore deposits; case

study from the Kidd Creek VMS deposit, Ontario, Canada. *Economic Geology and the Bulletin of the Society of Economic Geologists., 101,* p. 1055-1061.

Kakegawa, T., & Nanri, H. (2006). Sulfur and carbon isotope analyses of 2.7 Ga stromatolites, cherts and sandstones in the Jeerinah Formation, Western Australia. *Precambrian Research, 148*(1-2), p. 115-124.

Kakegawa, T., & Ohmoto, H. (1999). Sulfur isotope evidence for the origin of 3.4 to 3.1 Ga pyrite at the Princeton gold mine, Barberton Greenstone Belt, South Africa. *Precambrian Research, 96*, p. 209-224.

Kaplan, I. R. (1983). Stable isotopes of sulfur, nitrogen and deuterium in Recent marine environments. *Stable Isotopes in Sedimentary Geology* (pp. 2-1-2-108). Columbia: SEMP.

Kerr, M., Hanley, J., Morrison, G., Everest, J., & Bray, C. (2015). Preliminary evaluation of trace hydrocarbon speciation and abundance as an exploration tool for footwall-style sulfide ores associated with the Sudbury Igneous Complex, Ontario, Canada. *Economic Geology*, p. 531-556.

Kerrich, R., & King, R. (1993). Hydrothermal zircon and baddeleyite in Val-d'Or Archean mesothermal gold deposits: characteristics, compositions, and fluid-inclusion properties, with implications for timing of primary gold mineralization. *Canadian Journal of Earth Science, 30,* p. 2334-2351.

Kerswill, J. A. (1986). Gold deposits hosted by iron formation in the Contwoyto Lake area, NWT. *Poster volume, Gold'86: An international symposium on the geology of gold deposits.* (pp. 82-85). A.M. Chater (ed.).

Kerswill, J. A. (1992). *Geological Survey of Canada, Open File 2484: Gold metallogeny of the Contwoyto Lake, Russell Lake and Courageous Lake areas, Slave Province, NWT.* Government of Northwest Territories.

Kerswill, J. A. (1993). Models for iron formation-hosted gold deposits. *Mineral deposits modelling, proceedings volume for the IUGS/UNESCO deposit modelling program (DMP) conference at eighth IAGOD symposium.* Ottawa: Geological Association of Canada, special volume, open file 2659.

Kerswill, J. A. (1996). Iron-formation hosted stratabound gold. In O. R. Eckstrand, W. D. Sinclair, & R. I. Thorpe, *Geology of Canadian Mineral Deposit Types* (pp. 367-382).

Khalil, K. I., El-Shazly, A. E., & Lehmann, B. (2015). Late Neoproterozoic banded iron formation (BIF) in the central Eastern Desert of Egypt: Mineralogical and

geochemical implications for the origin of the Gebel El Hadid iron ore deposit. *Ore Geology Reviews*, In Press.

King, J. E., Davis, W. J., & Relf, C. (1992). Late Archean tectono-magmatic evolution of the central Slave Province, Northwest Territories. *Canadian Journal of Earth Science, 29*, 2156-2170.

King, J. E., Davis, W. J., Relf, C., & Avery, R. W. (1988). Deformation and plutonism in the western Contwoyto Lake map area, central Slave Province, District of Mackenzie, N.W.T. *Current Research, Part C, Geological Survey of Canada, Paper 88-1C*, 161-176.

King, J. E., Davis, W. J., Relf, C., & Van Nostrand, T. (1990). Geology of the Contwoyto - Nose Lakes map area, central Slave Province, District of MacKenzie, N.W.T. *Geological Survey of Canada, Paper 90-1C*, p. 177-187.

Klein, C., & Beukes, N. J. (1993). Proterozoic iron-formations. In K. C. Condie, *Development in Precambrian Geology: Proterozoic crustal, evolution 10* (pp. p. 383-418).

Kretschmar, U. (1973). *Phase relations involving arsenopyrite in the system Fe-As-S and their application. Ph.D. thesis.* Toronto, ON: University of Toronto.

Kretschmar, U., & Scott, S. D. (1976). Phase relations involving arsenopyrite in the system Fe-As-S and their application. *Can. Mineral., 14*, 364-386.

Lhotka, P. G., & Nesbitt, B. E. (1989). Geology of unmineralized and gold-bearing iron formation, Contwoyto Lake Point Lake region, Northwest Territories, Canada. *Canadian Journal of Earth Sciences (Revue canadienne des sciences de la Terre), 26*(1), p.46-64.

Marin-Carbonne, J., Rollion-Bard, C., Bekker, A., Rouxel, O., Agangi, A., Cavalazzi, B., et al. (2014). Coupled Fe and S isotope variations in pyrite nodules from Archean shale. *Earth and Planetary Science Letters., 392*, p. 67-79.

Marty, B., & Dauphas, N. (2002). The nitrogen record of crust-mantle interaction and mantle convection from Archean to Present. *Earth and Planetary Science Letters, 206*, p. 397-410.

Marty, B., & Zimmermann, L. (1999). Volatiles (He, C, N, Ar) in mid-ocean ridge basalts: assesment of shallow-level fractionation and characterization of source composition. *Geochimica et Cosmochimica Acta, 63*(21), p. 3619-3633.

McCuaig, T. C., Kerrich, R., Groves, D. I., & Archer, N. (1993). The nature and dimensions of regional and local gold-related hydrothermal alteration in tholeiitic

metabasalts in the Norseman goldfields: The missing link in a crustal continuum of gold deposits? *Miner. Deposita, 28*, 420–435.

Mernagh, T. P., & Bastrakov, E. N. (2013). An evaluation of hydrogen sulfide in anorogenic gold fluids and the uncertainties associated with vapor-rich inclusions. *Geofluids, 13*, 494-505.

Mernagh, T. P., & Witt, W. K. (1994). Early, methane-rich fluids and their role in Archaean gold mineralisation at the Sand King and Missouri deposits, Eastern Goldfields Province, Western Australia. *Journal of Australian Geology & Geophysics, 15*(3), 297-312.

Mikucki, E. J., & Ridley, J. R. (1993). The hydrothermal fluid of Archa an lode-gold deposits at different metamorphic grades: compositional constraints from ore and wallrock alteration assemblages. *Mineralium Deposita, 28*, 469-481.

Mining and exploration in Nunavut what is actually going on up there?(MINING IN CANADA'S TERRITORIES). (Nov, 2012). *Engineering & Mining Journal, 213*(11), p. 93-98.

Mortensen, J. K., Relf, C., Davis, W. J., & King, J. E. (1992). *U-Pb zircon ages from the Shallow Bay volcaniclastic belt, Contwoyto Lake area, Northwest Territories: age constraints for Lupin-type iron-formation.* Radiogenic Age and Isotopic Studies: Report 5, Geological Survey of Canada, Paper 91-2.

Naden, J., & Shepherd, T. J. (1989). Role of methane and carbon dioxide in gold deposition. *Nature, 342*, 793-795.

Palenik, C. S., Utsunomiya, S., Reich, M., Kesler, S. E., Wang, L., & Ewing, R. C. (2004). "Invisible" gold revealed: Direct imaging of gold nanoparticles in a Carlin-type deposit. *American Mineralogist, 89*(10), 1359-1366.

Papineau, D., Mojzsis, S. J., Karhu, J. A., & Marty, B. (2005). Nitrogen isotopic composition of ammoniated phyllosilicates: case studies from Precambrian metamorphosed sedimentary rocks. *Chemical Geology, 216*(1-2), p. 37-58.

Peretti, A., Dubessy, J., Mullis, J., Frost, B. R., & Trommsdorff, V. (1992). Highly reducing conditions during Alpine metamorphism of the Malenco peridotite (Sondrio, northern Italy) indicated by mineral paragenesis and H 2 in fluid inclusions. *Contributions to Mineralogy and Petrology, 112*, 329-340.

Pokrovski, G. S., Borisova, A. Y., & Harrichoury, J. C. (2008a). The effect of sulfur on vapor-liquid fractionation of metals in hydrothermal systems. *Earth and Planetary Science Letters, 266*, 345-362.

Potter, J., & Longstaffe, F. J. (2007). A gas-chromatograph, continuous flow-isotope ratio mass-spectrometer method for δ13C and δD measurement of complex fluid inclusion volatiles: examples from the Khibina alkaline igneous complex, northwest Russia and the south Wales coalfields. *Chemical Geology, 244,* p. 186-201.

Potter, J., Salvi, S., & Longstaffe, F. J. (2013). Abiogenic hydrocarbon isotopic signatures in granitic rocks: Identifying pathways of formation. *Lithos*(182-183), p. 114-124.

Proskurowski, G., Lilley, M. D., Seewald, J. S., Früh-Green, G. L., Olson, E. J., Lupton, J. E., et al. (2008). Abiogenic hydrocarbon production at Lost City hydrothermal field. In: Potter, J., Salvi, S., & Longstaffe, F. J. (2013). Abiogenic hydrocarbon isotopic signatures in granitic rocks: Identifying pathways of formation. Lithos(182-183), p. 114-124.

Relf, C. (1989). Archean deformation of the Contwoyto Formation metasediments, western Contwoyto Lake area, Northwest Territories. *Geological Survey of Canada, Paper 89-1C,* p. 95-105.

Relf, C. (1990). Archean deformation and metamorphism of metasedimentary rocks in the Contwoyto-Nose Lakes area, central Slave Province, N.W.T. *Geological Survey of Canada, Paper 90-1C,* p.97-106.

Schmidt, C., & Bodnar, R. J. (2000). Synthetic fluid inclusions: XVI. PVTX properties in the system H2O-NaCl-CO2 at elevated temperatures, pressures, and salinities. *Geochimica et Cosmochimica Acta, 64*(22), 3853–3869.

Seward, T. M. (1973). Thio complexes of gold and the transport of gold in hydrothermal ore solutions. *Geochimica et Cosmochimica Acta., 37*(3), 379-399.

Sharp, Z. D., Essene, E. J., & Kelly, W. C. (1985). A re-examination of the arsenopyrite geothermometer: pressure considerations and applications to natural assemblages. *Journal of the Mineralogical Association of Canada, 23,* 517-534.

Shen, Y., Buick, R., & Canfield, D. E. (2001). Isotopic evidence for microbial sulphate reduction in the early Archaean era. *Nature, 410,* 77-81.

Shenberger, D. M., & Barnes, H. L. (1989). Solubility of gold in aqueous sulfide solutions from 100 to 350˚C. *Geochim. Cosmochim. Acta, 53,* 269-278.

Sherwood-Lollar, B., Lacrampe-Coloumbe, G., Slater, G. F., Ward, J., Moser, D. P., Gihring, T. M., et al. (2006). Unravelling abiogenic and biogenic sources of methane in the Earth's deep subsurface. In: Potter, J., Salvi, S., & Longstaffe, F. J.

(2013). Abiogenic hydrocarbon isotopic signatures in granitic rocks: Identifying pathways of formation. Lithos(182-183), p. 114-124.

Sherwood-Lollar, B., Westgate, T. D., Ward, J. A., Slater, G. F., & Lacrampe-Couloume, G. (2002). Abiogenic formation of alkanes in the earth's crust as a minor source for global hydrocarbon reservoirs. In: Potter, J., Salvi, S., & Longstaffe, F. J. (2013). Abiogenic hydrocarbon isotopic signatures in granitic rocks: Identifying pathways of formation. Lithos(182-183), p. 114-124.

Skoog, D. A., Holler, F. J., & Crouch, S. R. (2007). *Principles of Instrumental Analysis Sixth Edition.* Belmont, CA, USA: Thomson Brooks/Cole.

Smith, D. S. (1996). Hydrothermal alteration at the Mineral Hill Mine, Jardine, Montana: A lower amphibolite facies archean lode gold deposit of probable synmetamorphic origin. *Economic Geology, 91*, p. 723-750.

Tarikh, S. (2015, May 6). *The Northern Miner*. Retrieved December 14, 2015, from The Northern Miner Web site: http://www.northernminer.com/news/wpc-aims-to-bring-lupin-back-online/1003589547/

Thode, H. G., Monster, J., & Dunford, H. B. (1961). Sulfur isotope geochemistry. *Geochim Cosmochim Acta, 25*, p. 159-174.

Thomazo, C., Ader, M., Farquhar, J., & Philippot, P. (2009). Methanotrophs regulated atmospheric sulfur isotope anomalies during the Mesoarchean (Tumbiana Formation, Western Australia). *Earth and Planetary Science Letters., 279*(1-2), p. 65-75.

van Breemen, O., Davis, W. J., & King, J. E. (1992). Temporal distribution of granitoid plutonic rocks in the Archean Slave Province, northwest Canadian Shield. *Canadian Journal of Earth Sciences, 29*(10), 2186-2199.

van Zuilen, M. A., Mathew, K., Wopenka, B., Lepland, A., Marti, K., & Arrhenius, G. (2005). Nitrogen and argon isotopic signatures in graphite from the 3.8-Ga-old Isua Supracrustal Belt, Southern West Greenland. *Geochimica et Cosmochimica Acta, 69*(5), p. 1241–1252.

Voytov, G. I. (1992). Chemical and carbon-isotopic fluctuations in free gases (gas jets) in the Khibiny. In: Potter, J., Salvi, S., & Longstaffe, F. J. (2013). Abiogenic hydrocarbon isotopic signatures in granitic rocks: Identifying pathways of formation. Lithos(182-183), p. 114-124.

Wacey, D., Noffke, N., Cliff, J., Barley, M. E., & Farquhar, J. (2015). Micro-scale quadruple sulfur isotope analysis of pyrite from the ~3480 Ma Dresser

Formation: New insights into sulfur cycling on the early Earth. *Precambrian Research*, *258*, p. 24-35.

Whelan, J. A., & Craig, H. (1983). Methane, Hydrogen and Helium in Hydrothermal Fluids of 21°N on the East Pacific Rise. In: Potter, J., Salvi, S., & Longstaffe, F. J. (2013). Abiogenic hydrocarbon isotopic signatures in granitic rocks: Identifying pathways of formation. Lithos(182-183), p. 114-124.

Wopenka, B., & Pasteris, J. D. (1986). Limitations to quantitative analysis of fluid inclusions in geological samples by laser Raman microprobe spectroscopy. *Applied Spectroscopy, 24*(2), pp. 144–151.

Wopenka, B., & Pasteris, J. D. (1987). Raman intensities and detection limits of geochemically relevant gas mixtures for a laser Raman microprobe. *Analytical Chemistry*, *59*(17), pp.2165-2170.

Appendix A

LA-ICP-MS operating conditions for arsenopyrite mapping

LA-ICP-MS Operating Conditions for LUP7 – Small Map, LUP7 – Big Map, and SIBX

LA	
Model	Resonetics RESOlution M-50
Wavelength	193 nm
Pulse duration (FWHM)	20 ns
Repetition rate	6 Hz (LUP7 - Small); 6 Hz (LUP7 - Big); 7 Hz (SIBX)
Spot diameter	48 um (LUP7 - Small); 90 um (LUP7 - Big); 90 um (SIBX)
Scan Speed	24 um/s (LUP7 - Small); 45 um/s (LUP7 - Big); 45 um/s (SIBX)
Energy density	7 J/cm2
Primary (calibration) standards	NIST 610 (synthetic doped glass)
ICP-MS	
Model	Thermo X-Series II
Forward power	1480 W
Shield torch	Used
Gas flows (He carrier mixed downstream from cell with Ar make up):	
Carrier (He)	0.65 L/min
Make up (Ar)	0.85 L/min
Additional	6 ml/min N2 for enhanced sensitivity
ThO^+/Th^+	<0.5%
U^+/Th^+ (NIST 612)	ca. 0.9
Data acquisition parameters	
Data acquisition protocol	Time Resolved Analysis
Scanning mode	Peak hopping
Dwell time per isotope	10 ms
Detector mode	Pulse counting and/or analogue
Isotopes determined	24Mg, 27Al, 29Si, 34S, 44Ca, 56Fe, 59Co, 60Ni, 65Cu, 66Zn, 82Se, 95Mo, 105Pd, 106Pd, 107Ag, 108Pd, 111Cd, 118Sn, 121Sb, 125Te, 195Pt, 197Au, 208Pb, 209Bi
Quadrupole settling time	Dynamic
Analysis time	60 s: ~ 30 s gas blank, 30 s ablation

Notes: NIST 610, BHVO2 and MASS were all analyzed, but NIST was the one used to calibrate the maps. There was one minute of washout between lines. ^{34}S was only analyzed for LUP7 – Small Map.

Appendix B

Quantified LA-ICP-MS Maps

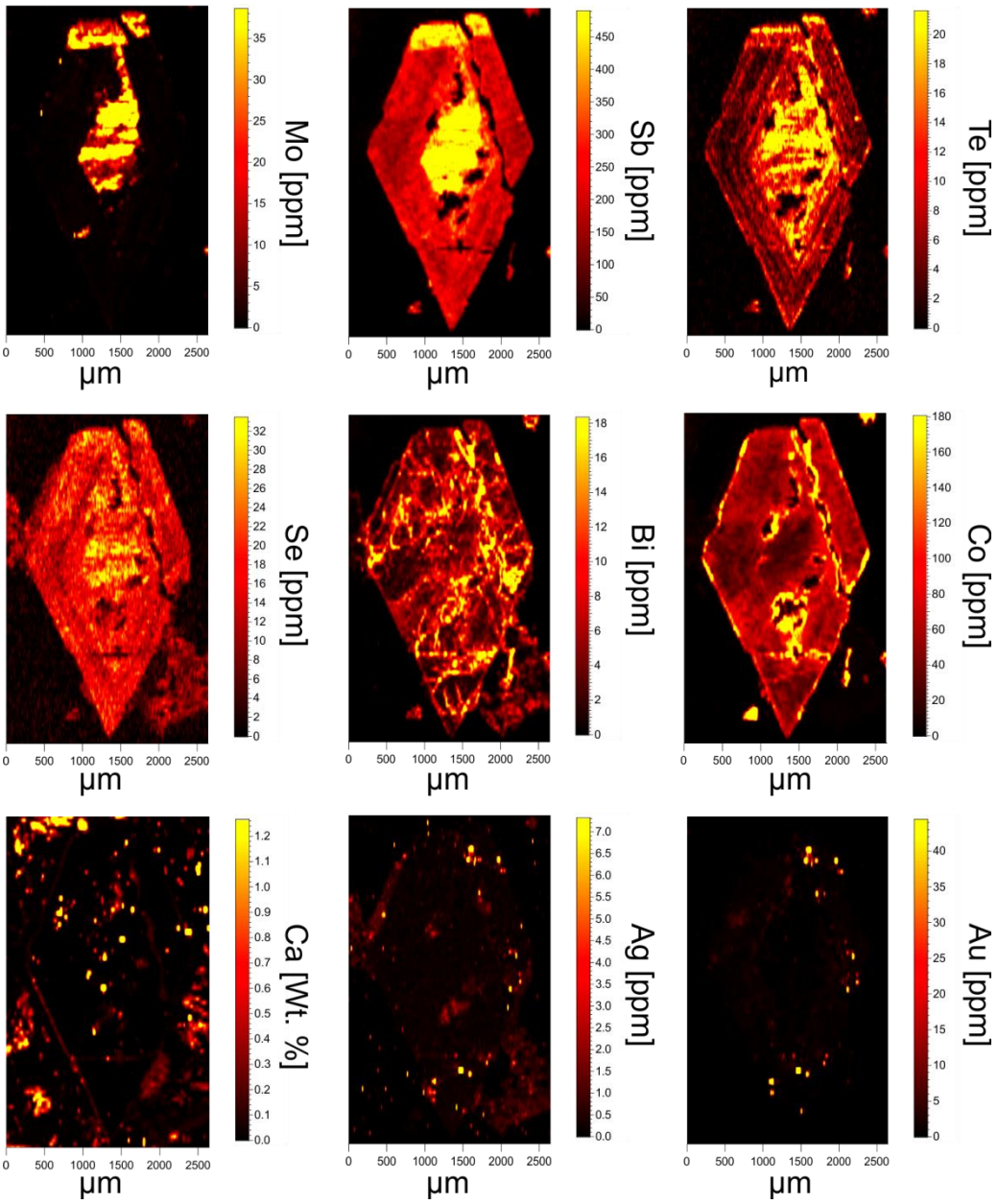

Figure I: LA-ICP-MS maps of LUP7 (small) arsenopyrite grain with linear scales. Maps include elemental Mo, Sb, Te, Se, Bi, Co, Ca, Ag, and Au.

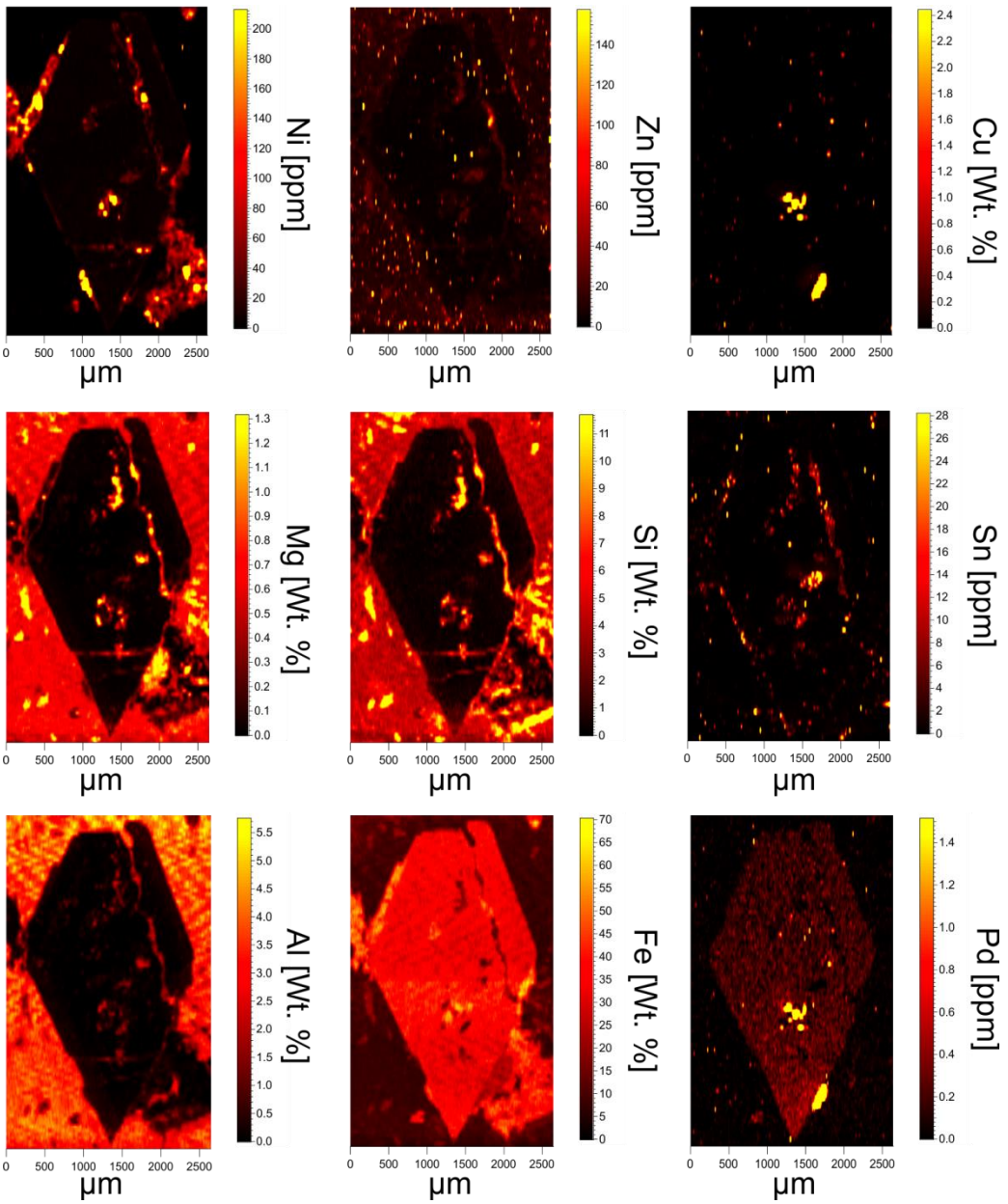

Figure II: LA-ICP-MS maps of LUP7 (small) arsenopyrite grain with linear scales. Maps include elemental Ni, Zn, Cu, Mg, Si, Sn, Al, Fe, and Pd.

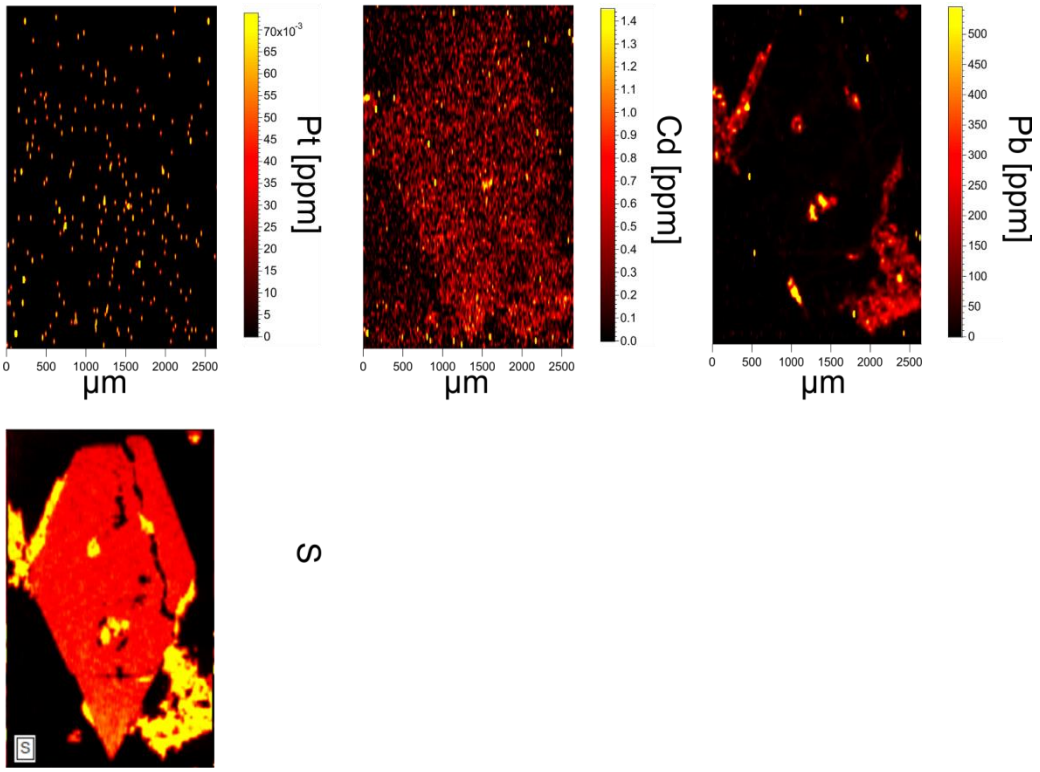

Figure III: LA-ICP-MS maps of LUP7 (small) arsenopyrite grain with linear scales. Maps include elemental Pt, Cd, Pb, and S. Sulfur does not have a scale; however, it is displayed to demonstrate its ubiquity, so a scale is unnecessary.

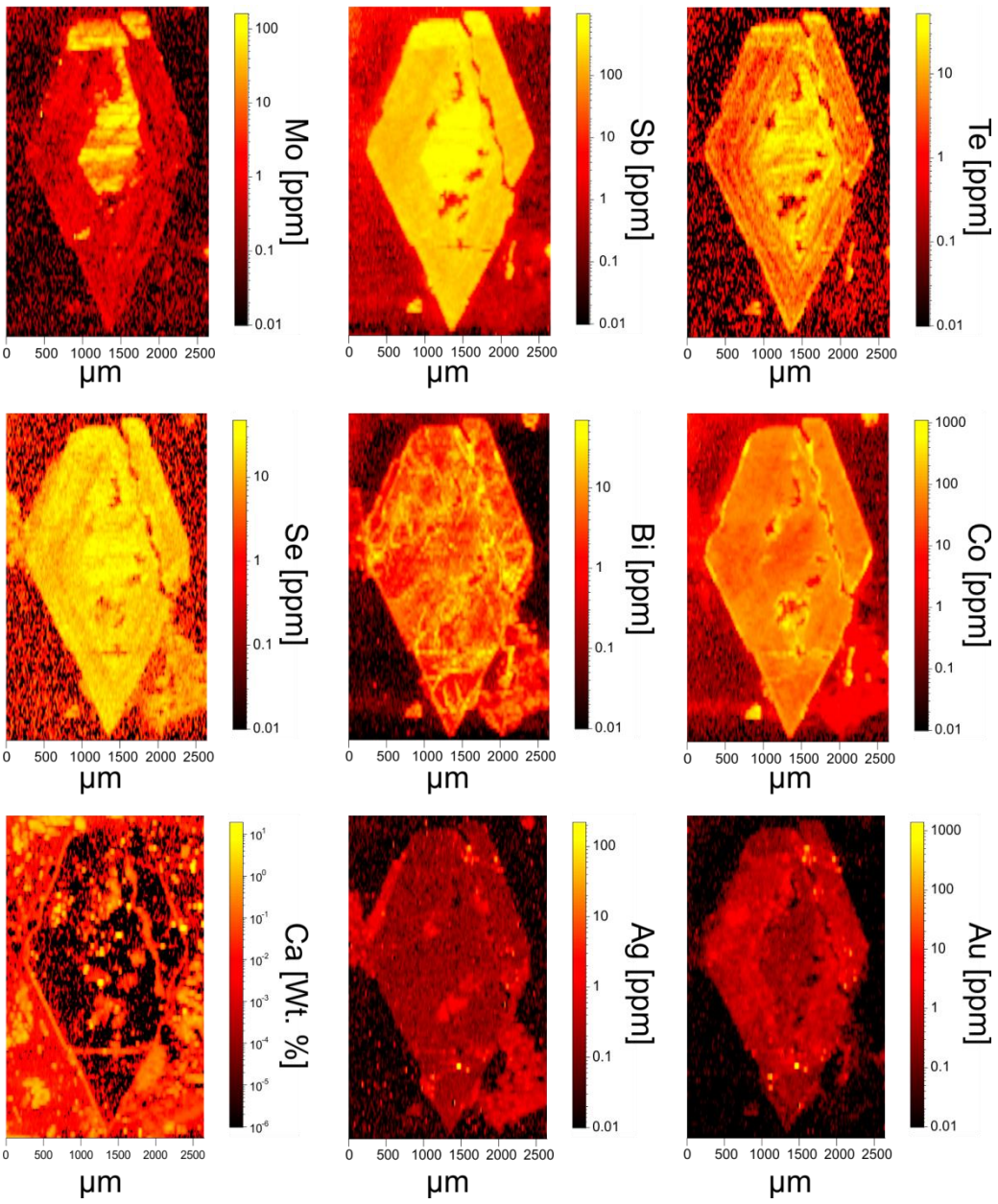

Figure IV: LA-ICP-MS maps of LUP7 (small) arsenopyrite grain with logarithmic scales. Maps include elemental Mo, Sb, Te, Se, Bi, Co, Ca, Ag, and Au.

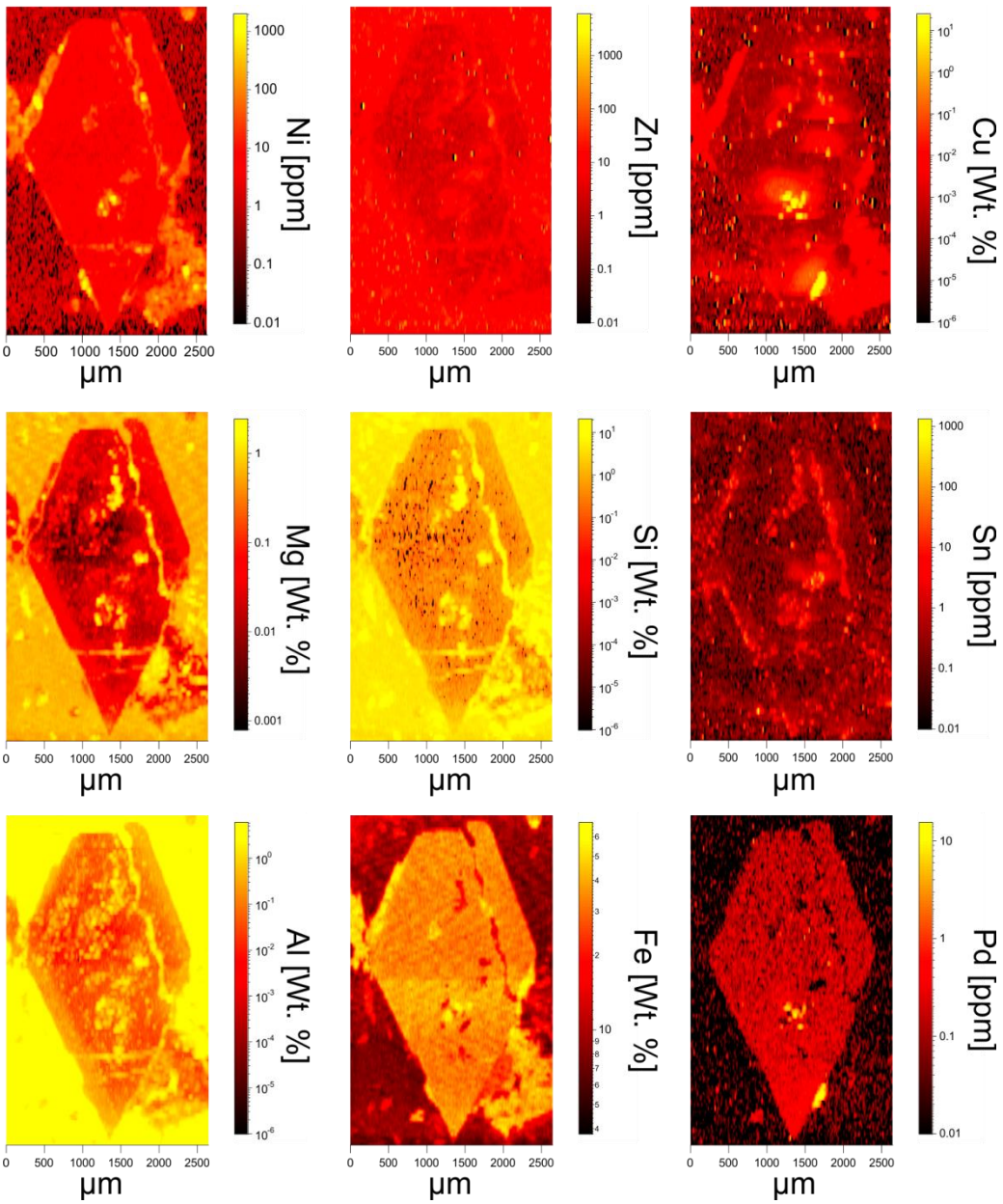

Figure V: LA-ICP-MS maps of LUP7 (small) arsenopyrite grain with logarithmic scales. Maps include elemental Ni, Zn, Cu, Mg, Si, Sn, Al, Fe, and Pd.

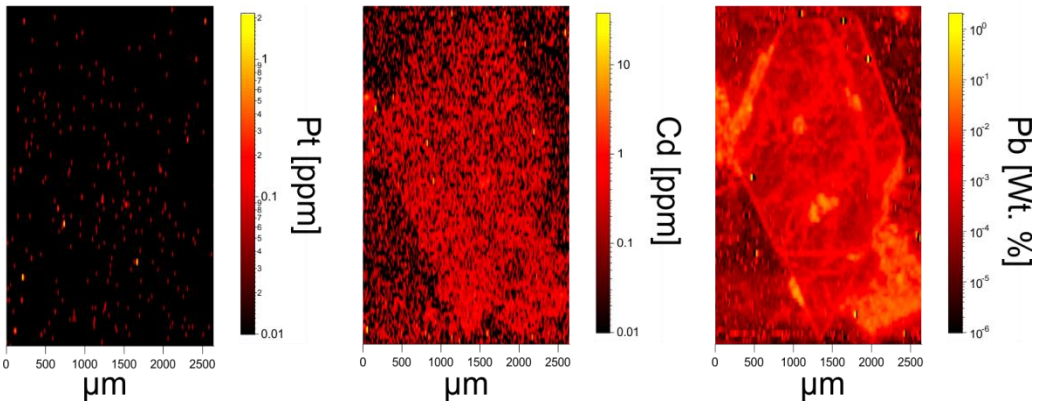

Figure VI: LA-ICP-MS maps of LUP7 (small) arsenopyrite grain with logarithmic scales. Maps include elemental Pt, Cd, and Pb.

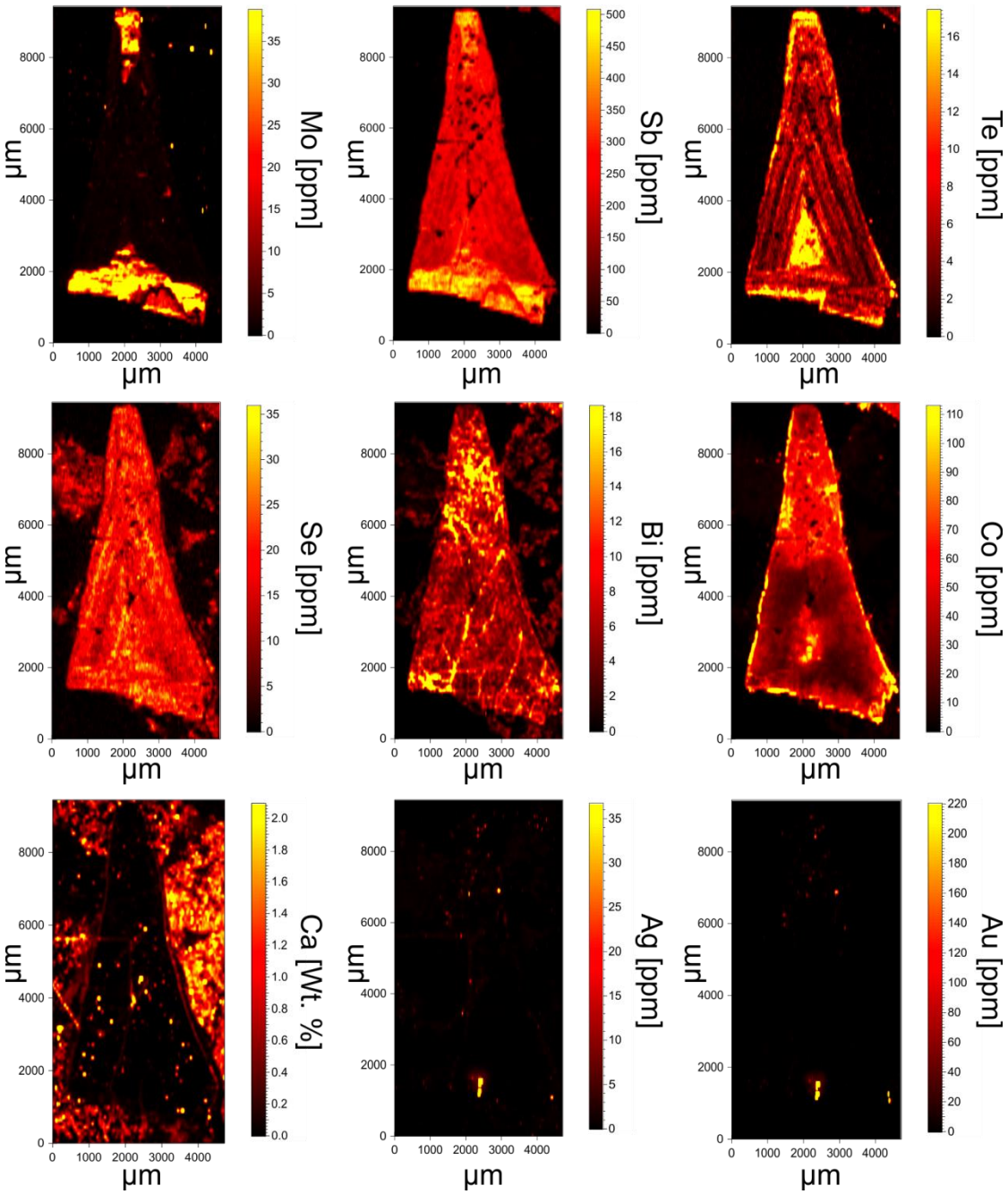

Figure VII: LA-ICP-MS maps of LUP7 (big) arsenopyrite grain with linear scales. Maps include elemental Mo, Sb, Te, Se, Bi, Co, Ca, Ag, and Au.

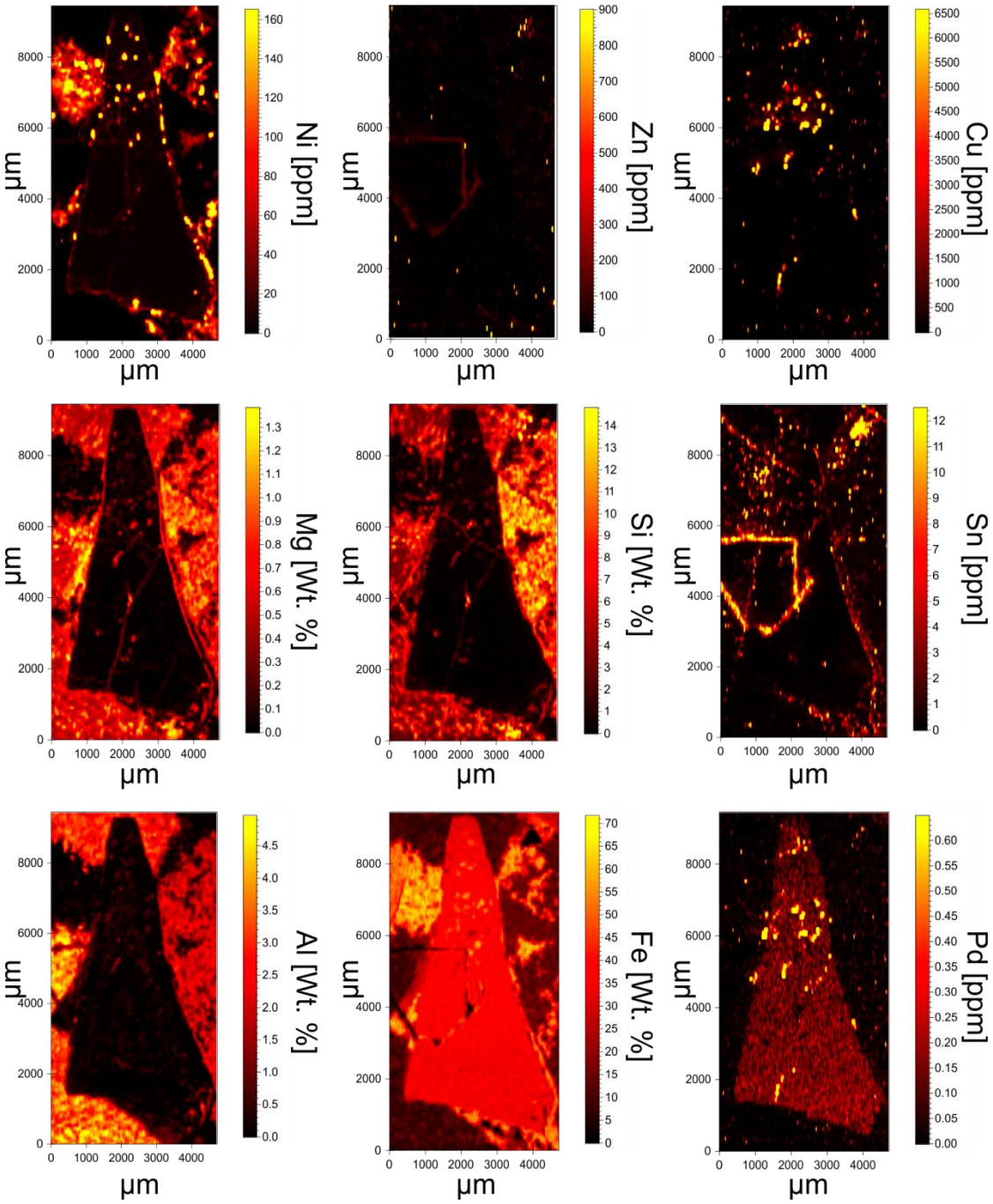

Figure VIII: LA-ICP-MS maps of LUP7 (big) arsenopyrite grain with linear scales. Maps include elemental Ni, Zn, Cu, Mg, Si, Sn, Al, Fe, and Pd.

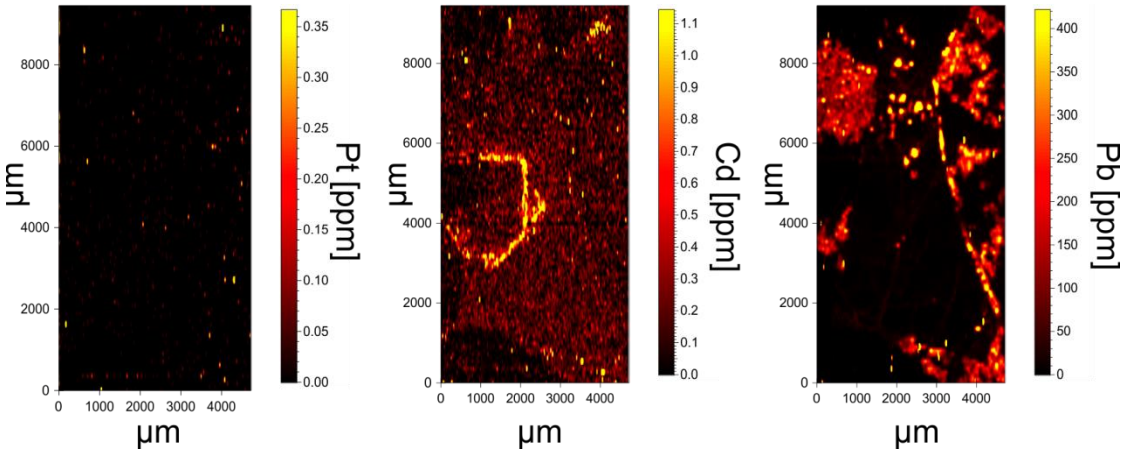

Figure IX: LA-ICP-MS maps of LUP7 (big) arsenopyrite grain with linear scales. Maps include elemental Pt, Cd, and Pb.

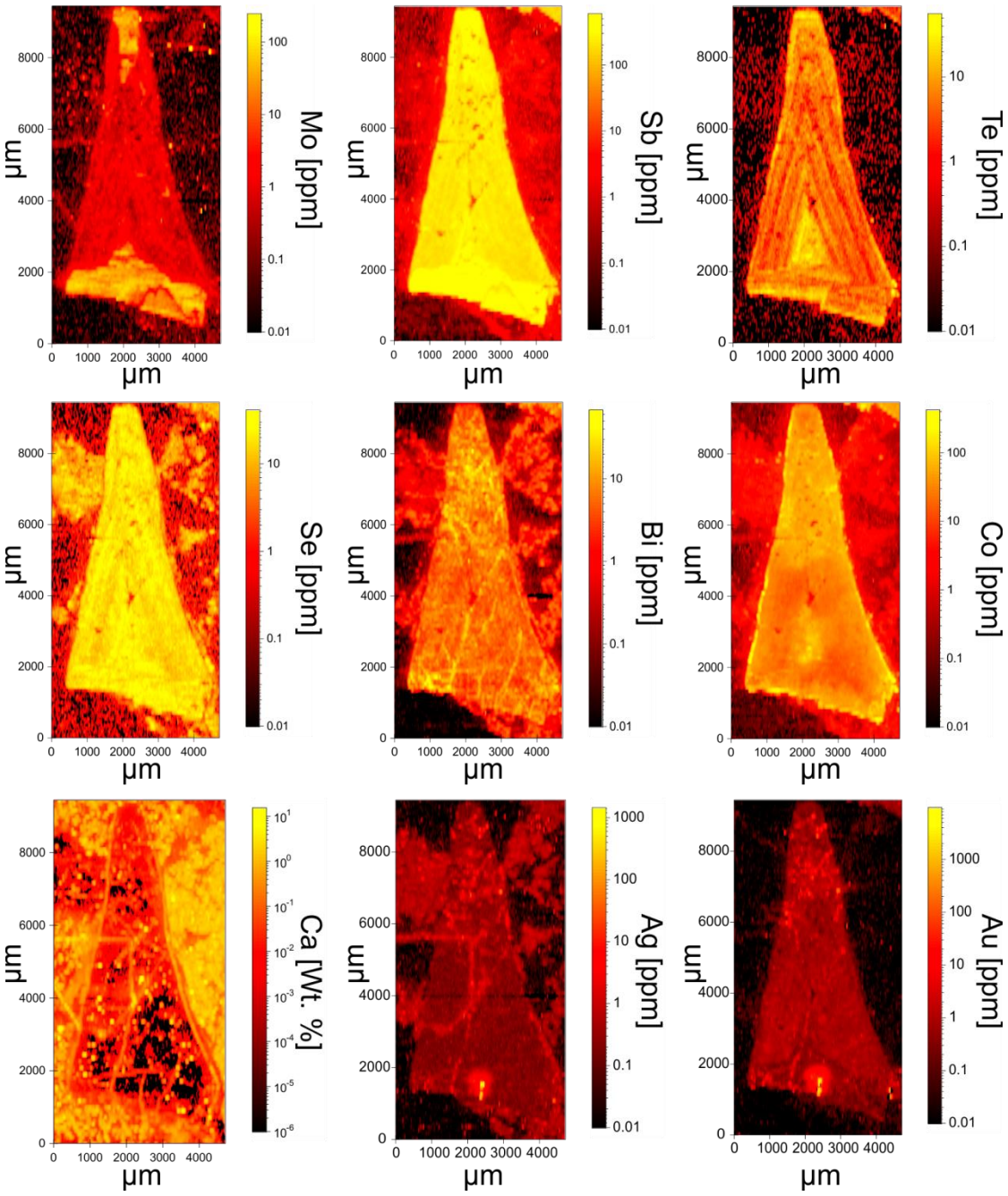

Figure X: LA-ICP-MS maps of LUP7 (big) arsenopyrite grain with logarithmic scales. Maps include elemental Mo, Sb, Te, Se, Bi, Co, Ca, Ag, and Au.

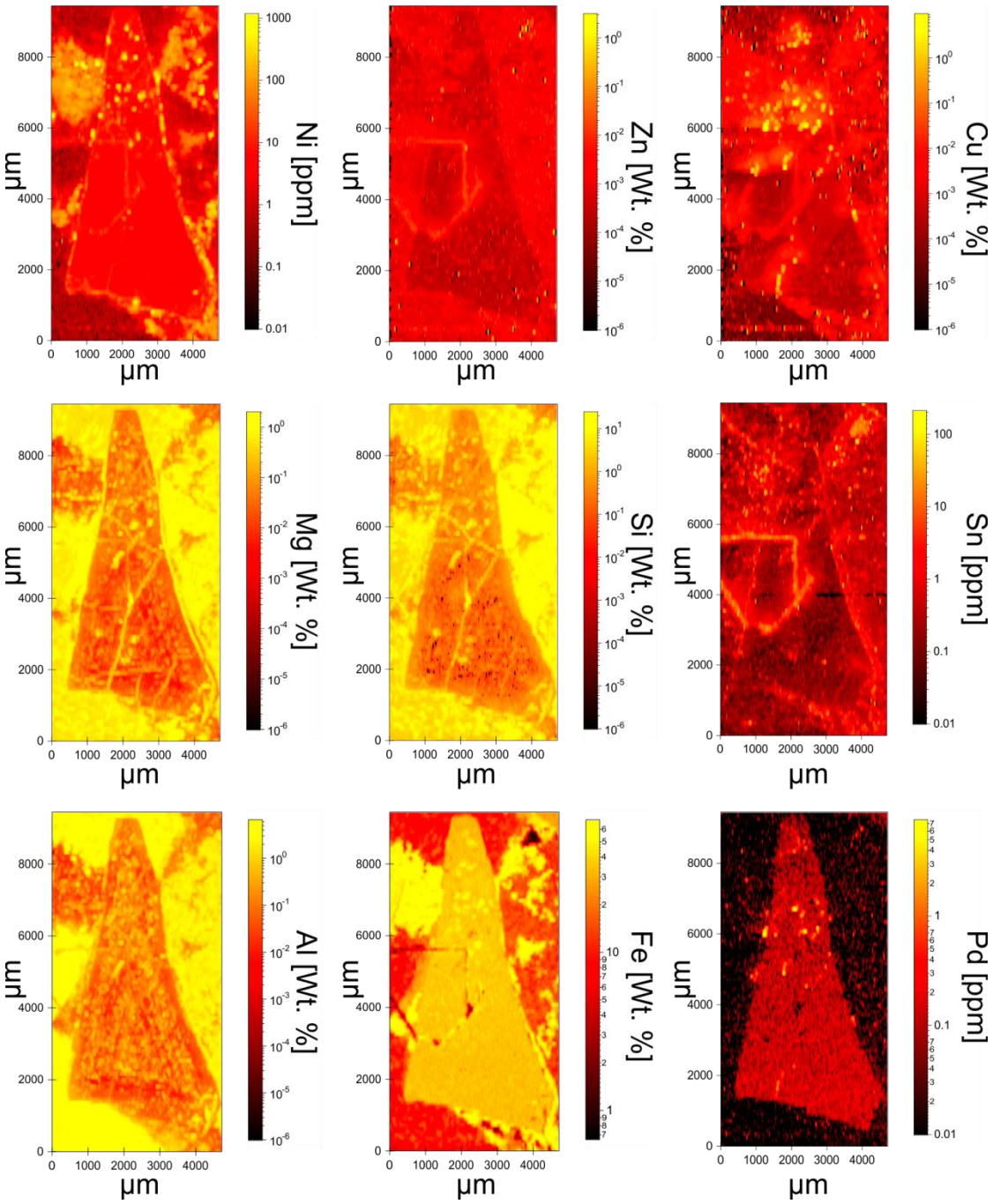

Figure XI: LA-ICP-MS maps of LUP7 (big) arsenopyrite grain with logarithmic scales. Maps include elemental Ni, Zn, Cu, Mg, Si, Sn, Al, Fe, and Pd.

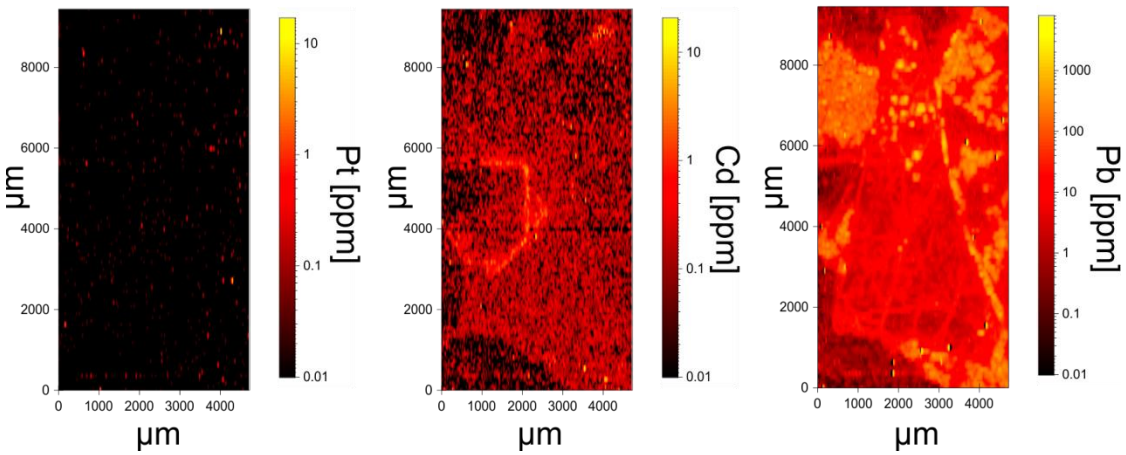

Figure XII: LA-ICP-MS maps of LUP7 (big) arsenopyrite grain with logarithmic scales. Maps include elemental Pt, Cd, and Pb.

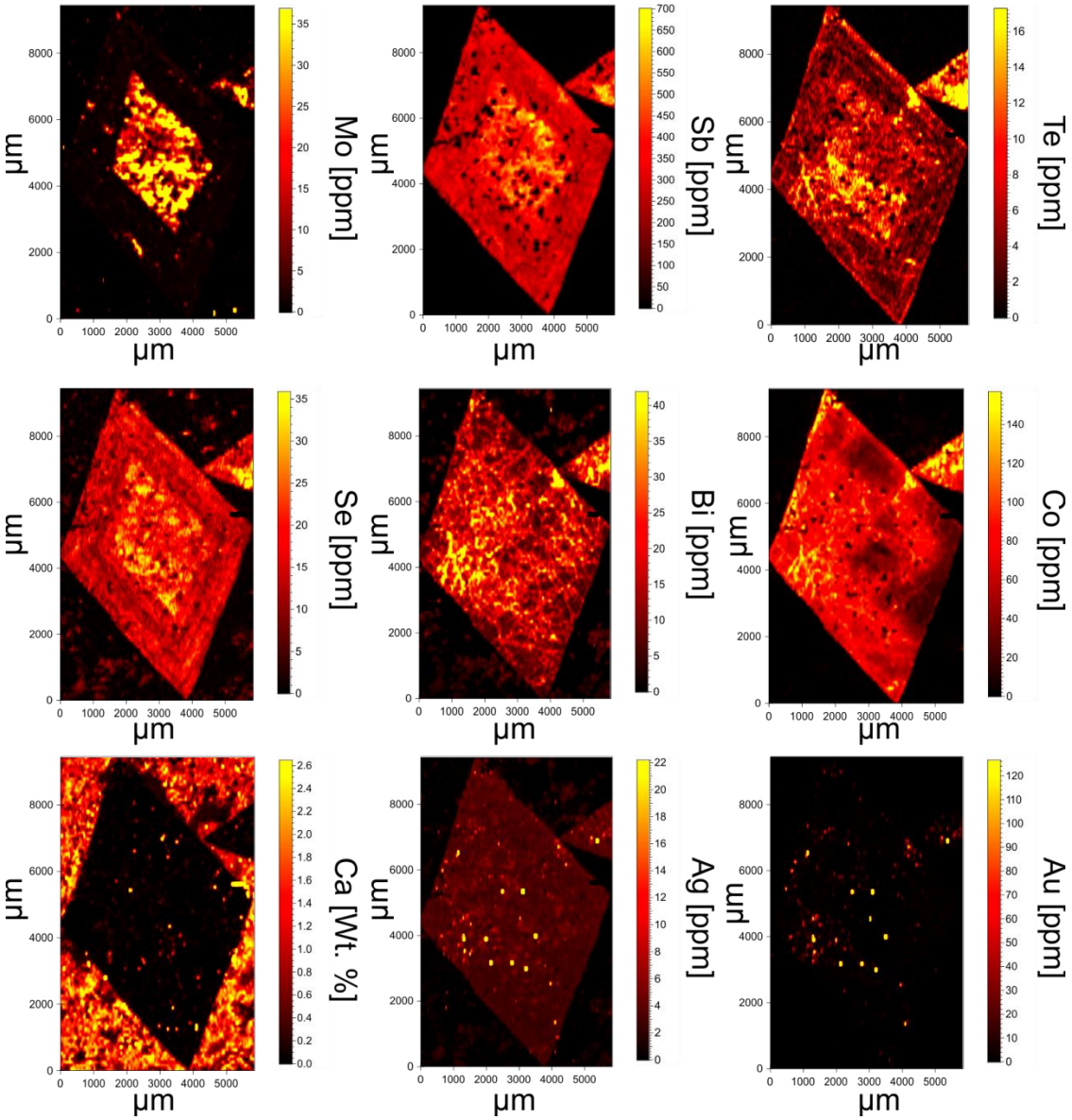

Figure XIII: LA-ICP-MS maps of SIBX arsenopyrite grain with linear scales. Maps include elemental Mo, Sb, Te, Se, Bi, Co, Ca, Ag, and Au.

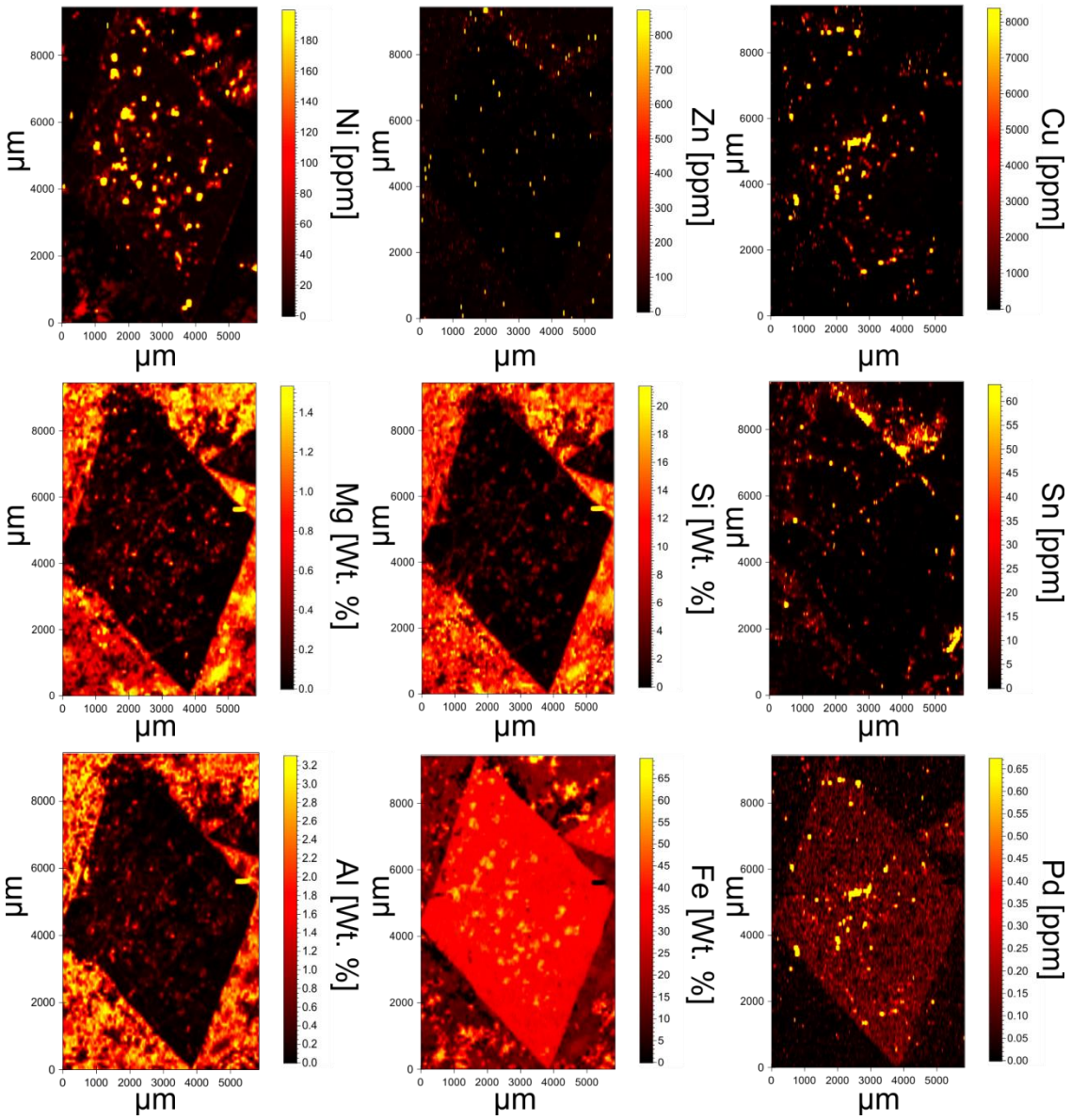

Figure XIV: LA-ICP-MS maps of SIBX arsenopyrite grain with linear scales. Maps include elemental Ni, Zn, Cu, Mg, Si, Sn, Al, Fe, and Pd.

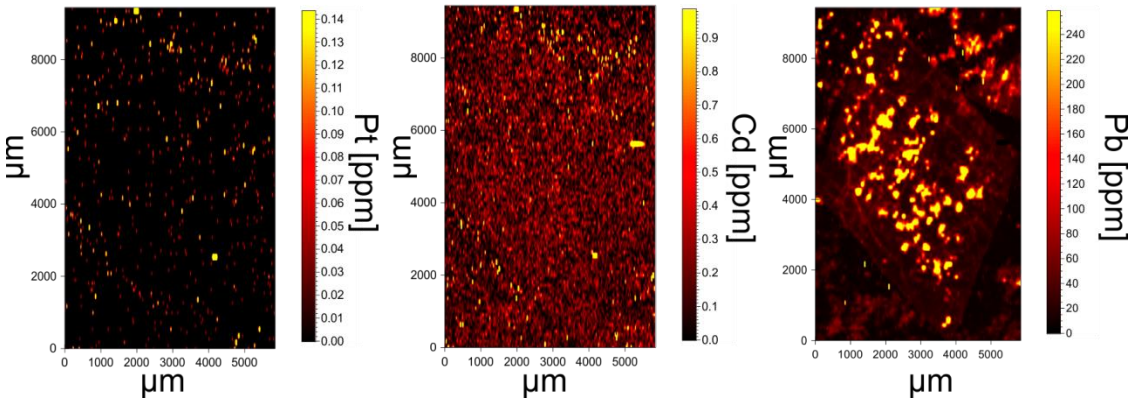

Figure XV: LA-ICP-MS maps of SIBX arsenopyrite grain with linear scales. Maps include elemental Pt, Cd, and Pb.

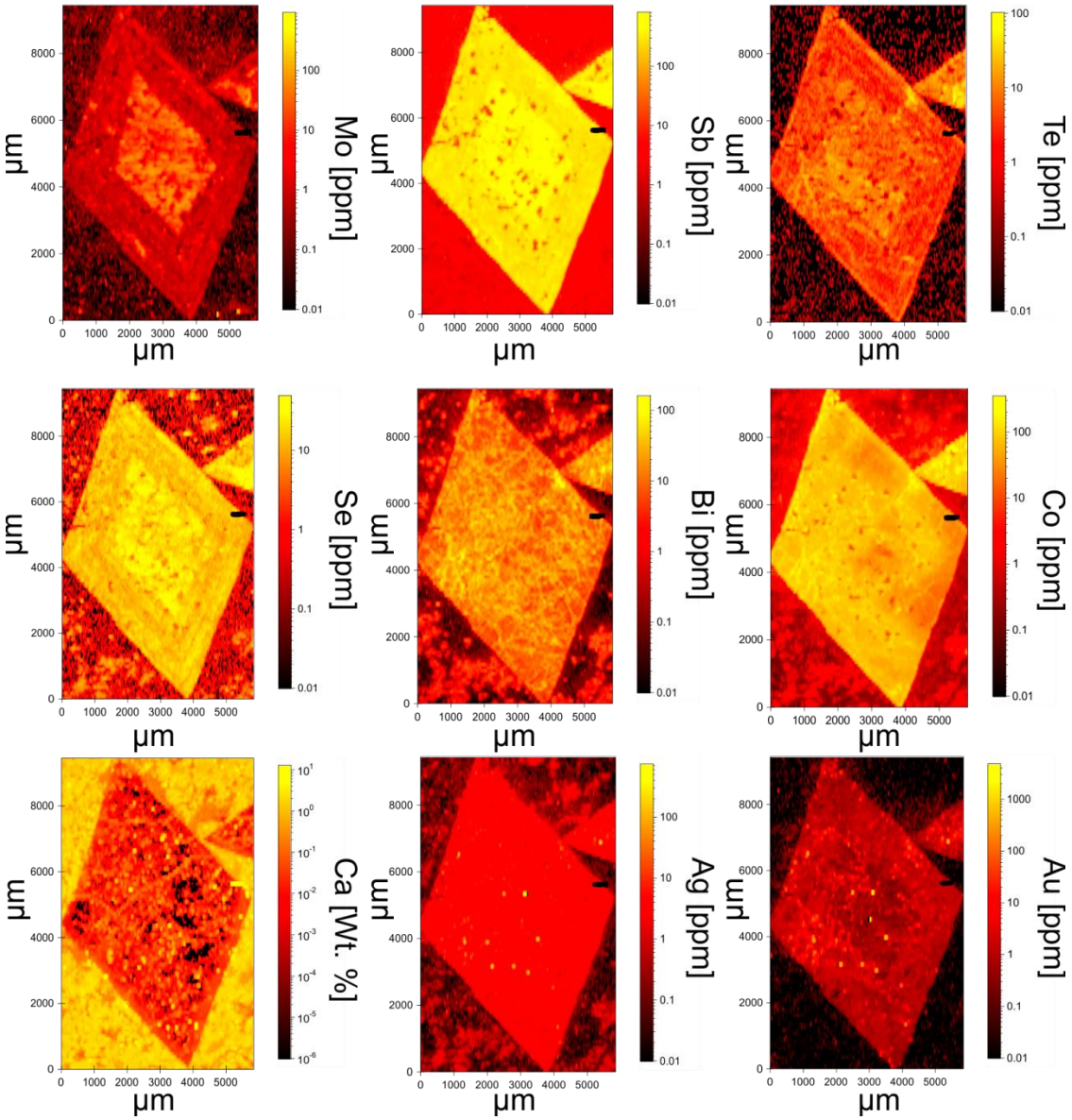

Figure XVI: LA-ICP-MS maps of SIBX arsenopyrite grain with logarithmic scales. Maps include elemental Mo, Sb, Te, Se, Bi, Co, Ca, Ag, and Au.

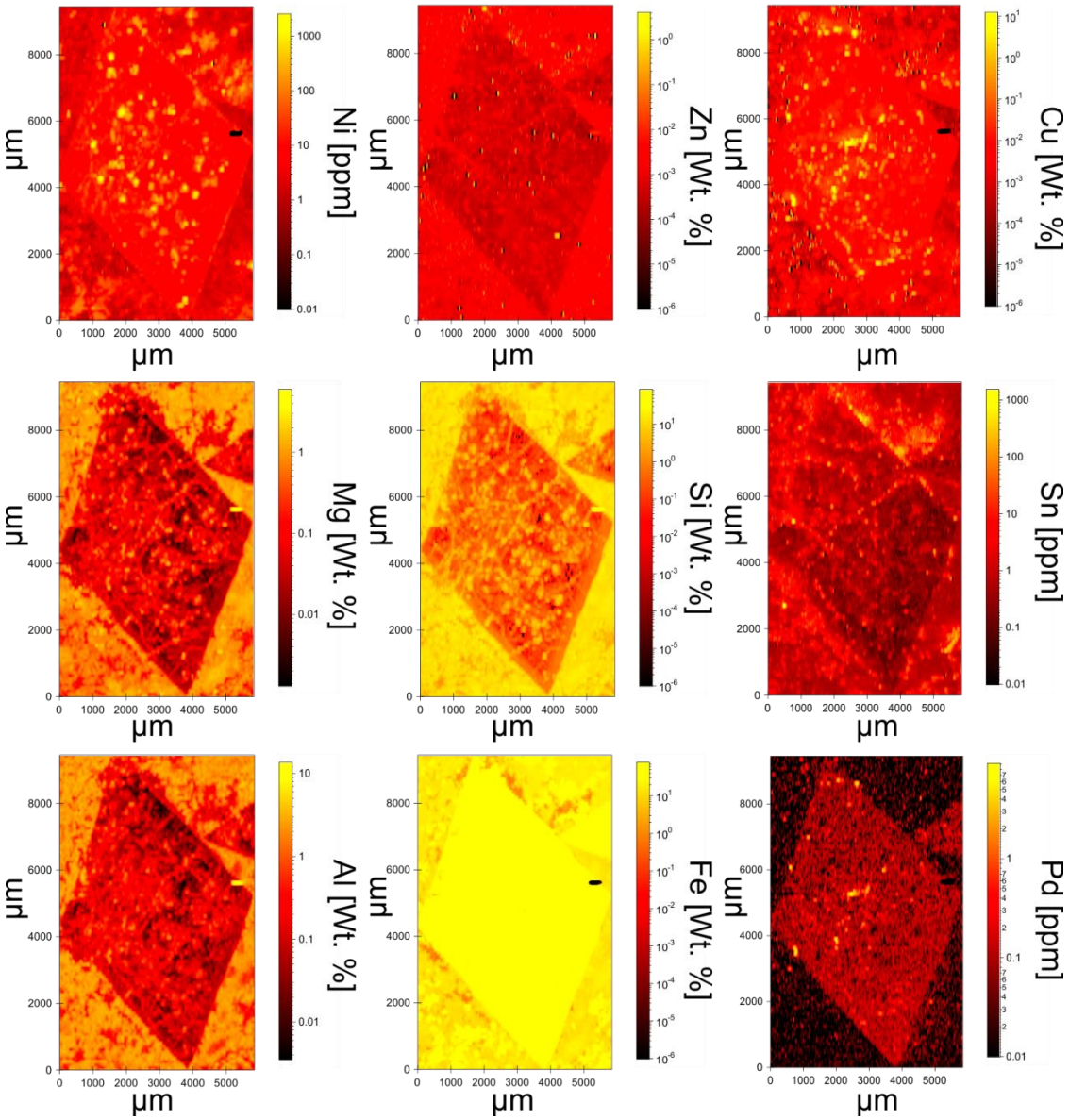

Figure XVII: LA-ICP-MS maps of SIBX arsenopyrite grain with logarithmic scales. Maps include elemental Ni, Zn, Cu, Mg, Si, Sn, Al, Fe, and Pd.

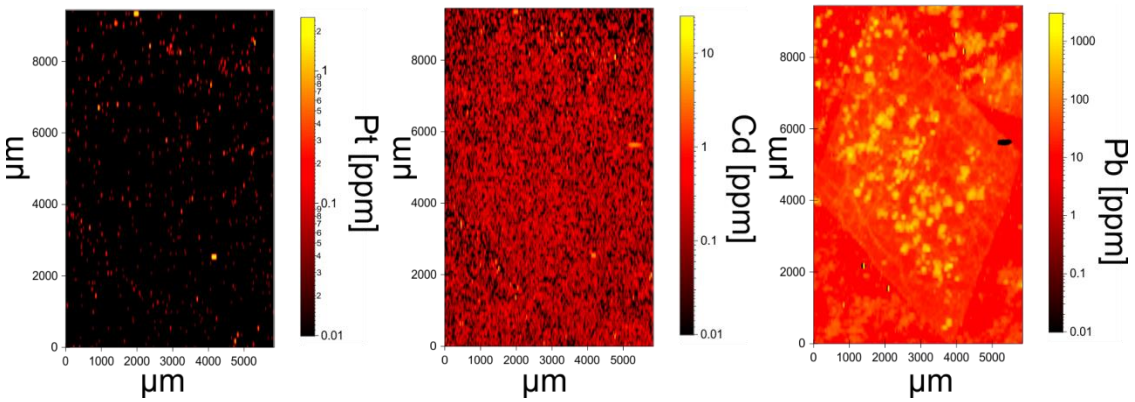

Figure XVIII: LA-ICP-MS maps of SIBX arsenopyrite grain with logarithmic scales. Maps include elemental Pt, Cd, and Pb.